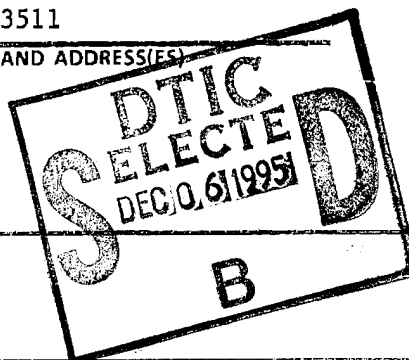


# REPORT DOCUMENTATION PAGE

Form Approved  
OMB No. 0704-0188

Public reporting burden for this collection of information is estimated to average 1 hour per response, including the time for reviewing instructions, searching existing data sources, gathering and maintaining the data needed, and completing and reviewing the collection of information. Send comments regarding this burden estimate or any other aspect of this collection of information, including suggestions for reducing this burden, to Washington Headquarters Services, Directorate for Information Operations and Reports, 1215 Jefferson Davis Highway, Suite 1204, Arlington, VA 22202-4302, and to the Office of Management and Budget, Paperwork Reduction Project (0704-0188), Washington, DC 20503.

1. AGENCY USE ONLY (Leave blank)		2. REPORT DATE		3. REPORT TYPE AND DATES COVERED FINAL REPORT 30 Sep 94 - 29 Sep 95	
4. TITLE AND SUBTITLE  Experimental and Theoretical Research on Advanced Vacuum Electronic Microwave Devices				5. FUNDING NUMBERS  6223N 0001/73	
6. AUTHOR(S)  Professor Destler					
7. PERFORMING ORGANIZATION NAME(S) AND ADDRESS(ES) University of Maryland Institute for Plasma Research Energy Research Building #223 Paint Branch Drive College Park, Maryland 20742-3511				8. PERFORMING ORGANIZATION REPORT NUMBER  AFOSR-TR-95 0771	
9. SPONSORING/MONITORING AGENCY NAME(S) AND ADDRESS(ES) AFOSR/NE 110 Duncan Avenue Suite B115 Bolling AFB DC 20332-0001				F49620-94-1-0432	
11. SUPPLEMENTARY NOTES					
12a. DISTRIBUTION/AVAILABILITY STATEMENT  APPROVED FOR PUBLIC RELEASE: DISTRIBUTION UNLIMITED				12b. DISTRIBUTION CODE	
13. ABSTRACT (Maximum 200 words)  This report summarizes the work done on the task titled "Harmonic Gyrotron Oscillators and Amplifiers", covering the period from September 30, 1994 to September 29, 1995. During the past year we have completed the test experiment of phase locking a 35 GHz second harmonic gyrotron oscillator using a quasi-optical circulator to separate injection and output signals. The experiment well demonstrated the capabilities of the hot test equipment in the harmonic gyrotron laboratory at UMCP and provided a good basis for understanding the importance of mode selective design and the phase-stable operating parameters of more advanced harmonic gyrotrons.					
14. SUBJECT TERMS				15. NUMBER OF PAGES	
				16. PRICE CODE	
17. SECURITY CLASSIFICATION OF REPORT UNCLASSIFIED		18. SECURITY CLASSIFICATION OF THIS PAGE UNCLASSIFIED		19. SECURITY CLASSIFICATION OF ABSTRACT UNCLASSIFIED	
20. LIMITATION OF ABSTRACT					



19951205 049

Final Report

**Experimental and Theoretical Research in Advanced Vacuum  
Electronic Microwave Devices**

Submitted to  
Air Force Office of Scientific Research

Submitted by  
Institute for Plasma Research and Electrical Engineering Department  
University of Maryland, College Park, MD 20742

October 1995

# Contents

<b>TASK A: Harmonic Gyrotron Oscillators and Amplifiers</b>	<b>1</b>
1 Summary	1
2 Accomplishments to Date	1
3 Recent Papers and Presentations Related to this Task	2
4 Efficiency Enhancement of Gyrotrons by Using Depressed Collectors	8
 <b>TASK B: Prebunched Gyrotron Studies</b>	 <b>13</b>
1 Overview	13
2 Theoretical Effort	14
2.1 Code development . . . . .	14
2.2 Small-orbit design . . . . .	15
2.3 Large-Orbit Design . . . . .	17
2.4 Broadband bunching investigation . . . . .	17
2.5 Electron gun design . . . . .	18
3 Experimental Effort	18
4 Proposed Work for the Next Year	19
 <b>TASK C: Studies of Cyclotron Maser Amplifiers with Trochoidal Electron Beams (Trochotrons)</b>	 <b>22</b>
 <b>Appendix: Papers Pertaining to this Project</b>	 <b>23</b>

<b>Accession For</b>	
NTIS GRA&I	<input checked="checked" type="checkbox"/>
DTIC TAB	<input type="checkbox"/>
Unannounced	<input type="checkbox"/>
Justification	
By	
Distribution/	
Availability Codes	
Disc	Avail and/or Special
A-1	

# TASK A: Harmonic Gyrotron Oscillators and Amplifiers

## 1 Summary

This report summarizes the work done on the task titled "Harmonic Gyrotron Oscillators and Amplifiers", covering the period from September 30, 1994 to September 29, 1995. During the past year we have completed the test experiment of phase locking a 35 GHz second harmonic gyrotron oscillator using a quasi-optical circulator to separate injection and output signals. The experiment well demonstrated the capabilities of the hot test equipment in the harmonic gyrotron laboratory at UMCP and provided a good basis for understanding the importance of mode selective design and the phase-stable operating parameters of more advanced harmonic gyrotrons.

We have also developed a special approach to realize a compact high performance MMW source. This special approach includes two aspects. First, we employ a new gyrotron operation regime in which multi-stage interaction is used with resonant cyclotron harmonic multiplication in each succeeding stage to provide sufficient prebunching of the MIG produced electron beam at lower harmonics, this will provide an efficient excitation of the EM field in the final stage of the device at a higher harmonic of the electron cyclotron frequency. Secondly we employ an experimentally demonstrated  $TE_{0n}$  mode selective circuit for input coupler and for each interaction stage in order to suppress unwanted competing modes which are inevitable in any harmonic gyro-device. For the purpose of demonstration of this approach, two proof-of-principle devices have been designed and contracted for fabrication. These devices are the two-stage harmonic multiplying gyro-TWT and the two-stage phase-controlled harmonic multiplying inverted gyrotwystron (phigtron). Both of them are with Ku-band, fundamental, gyro-TWT prebunching and Ka-band second harmonic output. In addition, we have also made good progress in preparing a Ka-band tunable magnetron source that might be used for driving a gyro-TWT with fourth harmonic W-band output and second harmonic Ka-band prebunching. The prebunched beam might also be used to optimize the efficiency of a fourth harmonic oscillator. This study on harmonic gyrotron amplifiers and oscillators has also been supported by MURI program since May 1, 1995. As a result, the research works are being able to continued.

## 2 Accomplishments to Date

During this reporting period and the few months preceding it, significant progress was made both in the experimental and theoretical aspects of the program. Accomplishments to date include the following:

1. Completion of the test experiment of phase locking a 35 GHz second harmonic gyrotron oscillator using a quasi-optical circulator to separate injection and output signals. Details of the test and analysis of the experimental results are presented in the appendix of this report.

DTIC QUALITY INSPECTED 2

2. Development of a new gyrotron concept, "harmonic multiplying gyrotron amplifiers and oscillators", with the potential for weakly relativistic small orbit gyro-devices to efficiently operate at fourth harmonic (Figures 1 and 2).
3. Completion of the engineering design of the 35 GHz, second harmonic gyro-TWT amplifier and the inverted gyrotwyston oscillator (phigtron) both implemented with complex mode selective circuitry and Ku band fundamental prebunching (Figures 3 and 4 and Table 1).
4. Contracting for fabrication of the above 35 GHz proof-of-principle harmonic multiplying gyrotrons.
5. Procurement of a surplus radar pulsar, 16 kV/16 A, with reconditioning and some modification as the high voltage modulator for a Ka-band tunable magnetron which has been borrowed from Prof. K.R. Chu (National Tsing Hua University, Taiwan, R.O.C.) and is planned for driving our fourth harmonic gyrotrons. This modulator has been installed, adjusted and made to work adequately in the magnetron performance test experiment.

### 3 Recent Papers and Presentations Related to this Task

1. H. Guo, V.L. Granatstein, B. Levush, T.M. Antonsen, Jr., J.P. Tate, J. Rodgers, and W.W. Destler, "Experimental Study of Phase-Controlled Harmonic Gyrotron Oscillators and Amplifiers," 1994 Microwave Power Tube Conference, Monterey, CA, May 10-12, 1994, abstracts in conference record, presentation 2B.7.
2. J.P. Tate, H. Guo, M. Naiman, L. Chen and V.L. Granatstein, "Experimental Proof-of-Principle Results on a Mode-Selective Input Coupler for Gyrotron Applications," IEEE Trans. MTT **42**, 1910 (1994).
3. H. Guo, V.L. Granatstein, T.M. Antonsen, Jr., B. Levush, J.P. Tate, and S.H. Chen, "Compact, Harmonic Multiplying Gyrotron Amplifiers," 1995 IEEE Int. Conf. on Plasma Science, June 5-8, 1995; abstract in Conference Record 95-CH35796, p. 211.
4. H. Guo, D.J. Hoppe, J. Rodgers, R.M. Perez, J.P. Tate, B.L. Conroy, V.L. Granatstein, A. Bhanji, P.E. Latham, G.S. Nusinovich, M. Naiman, and S.H. Chen, "Phase-Locking of a Second Harmonic Gyrotron Oscillator Using a Quasi-Optical Circulator to Separate Injection and Output Signals," IEEE Trans. Plasma Sci., Oct. 1995, to be published.

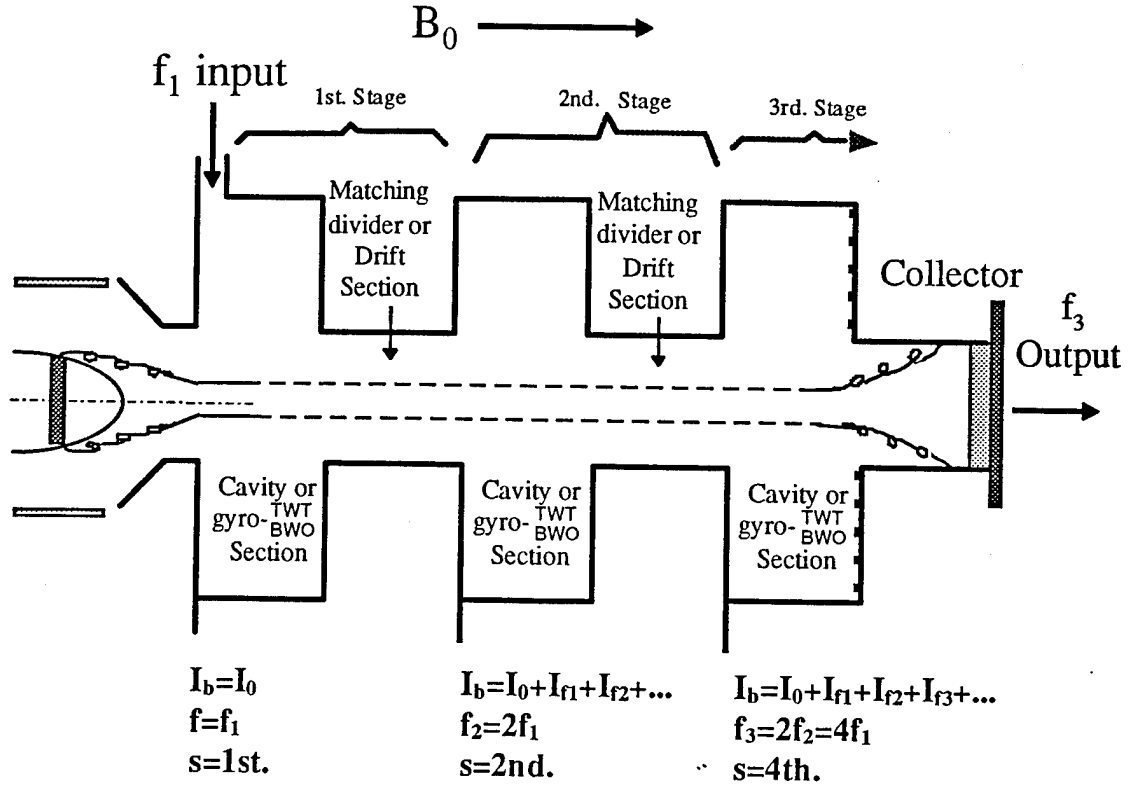


Figure 1 Physical Mechanism and Configuration of the Harmonic Multiplying Gyrotron

- 1st. stage:
- i) beam modulation by  $V_{f1} \approx \int E_1^{\text{effect}} d(r_e \theta)$
  - ii) fundamental ECRM interaction
  - iii)  $I_b = I_0 \rightarrow$  at the entrance
- 2nd. stage:
- i)  $I_b = I_0 + I_{f1} + I_{f2} \dots$  at the entrance and  $f_2 = 2 f_1$
  - ii)  $V_{f2} \approx \int E_2^{\text{effect}} d(r_e \theta)$  initiated by  $I_{f2}$
  - iii) second harmonic ECRM interaction
  - iv) beam further modulated by  $V_{f2}$
- 3rd. stage:
- i)  $I_b = I_0 + I_{f1} + I_{f2} + I_{f4} \dots$  at the entrance and  $f_4 = 2 f_2 = 4 f_1$
  - ii)  $V_{f4} \approx \int E_4^{\text{effect}} d(r_e \theta)$  initiated by  $I_{f4}$
  - iii) fourth harmonic ECRM interaction
  - iv)  $V_{f4}$ ;  $I_{f4} \Rightarrow$  output power

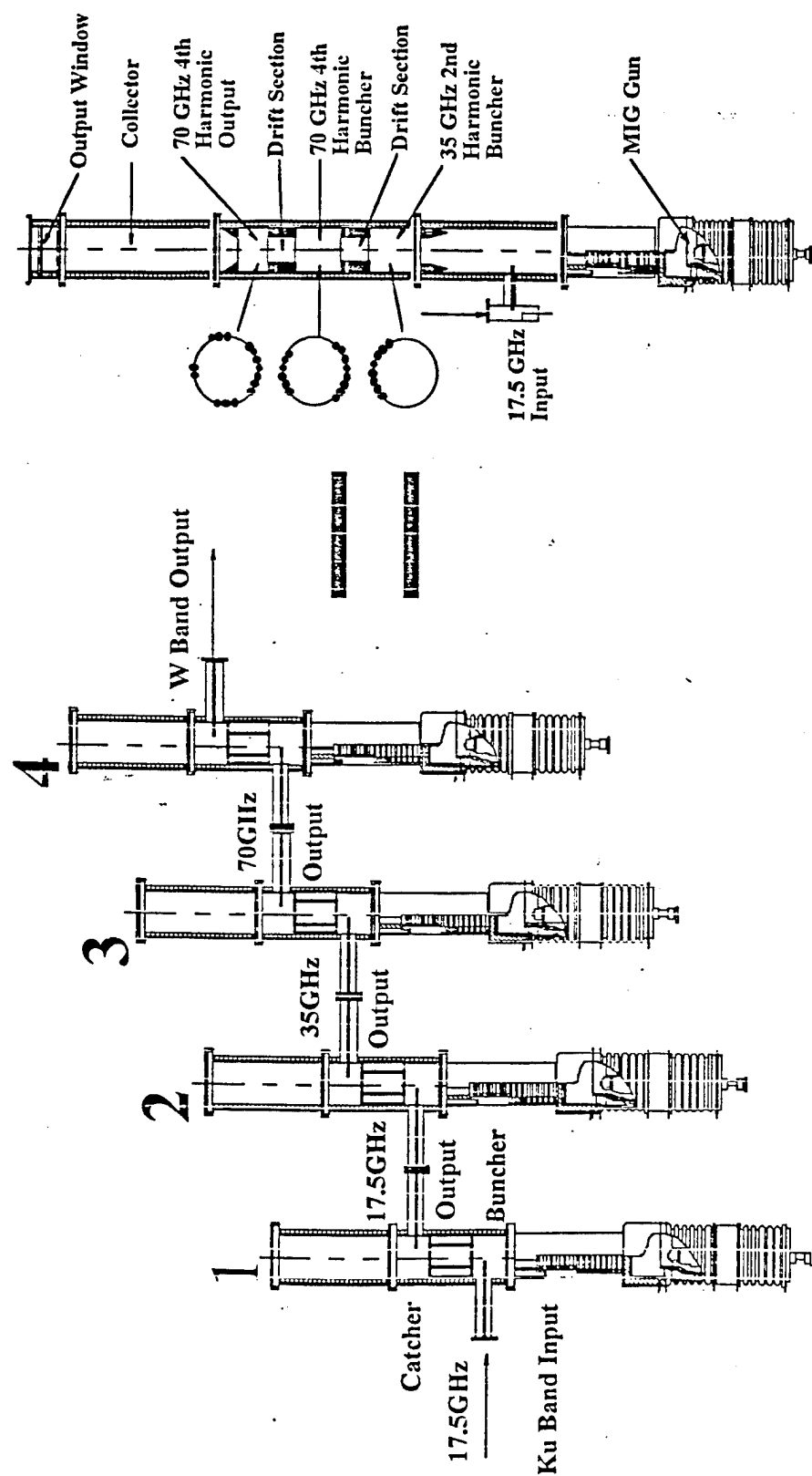


Figure 2 Cascade Gyrokystron Amplifiers With Frequency And Harmonic

Multiplying  $\approx$  A Phigtron Amplifier

1. Ku band fundamental gyrokystron
2. Gyrokystron with fundamental prebunch and second harmonic output
3. Gyrokystron with second harmonic prebunch and fourth harmonic output
4. fourth harmonic W band gyrokystron amplifier
5. Phase-controlled harmonic-multiplying inverted gyrotwycron ( Phigtron ).

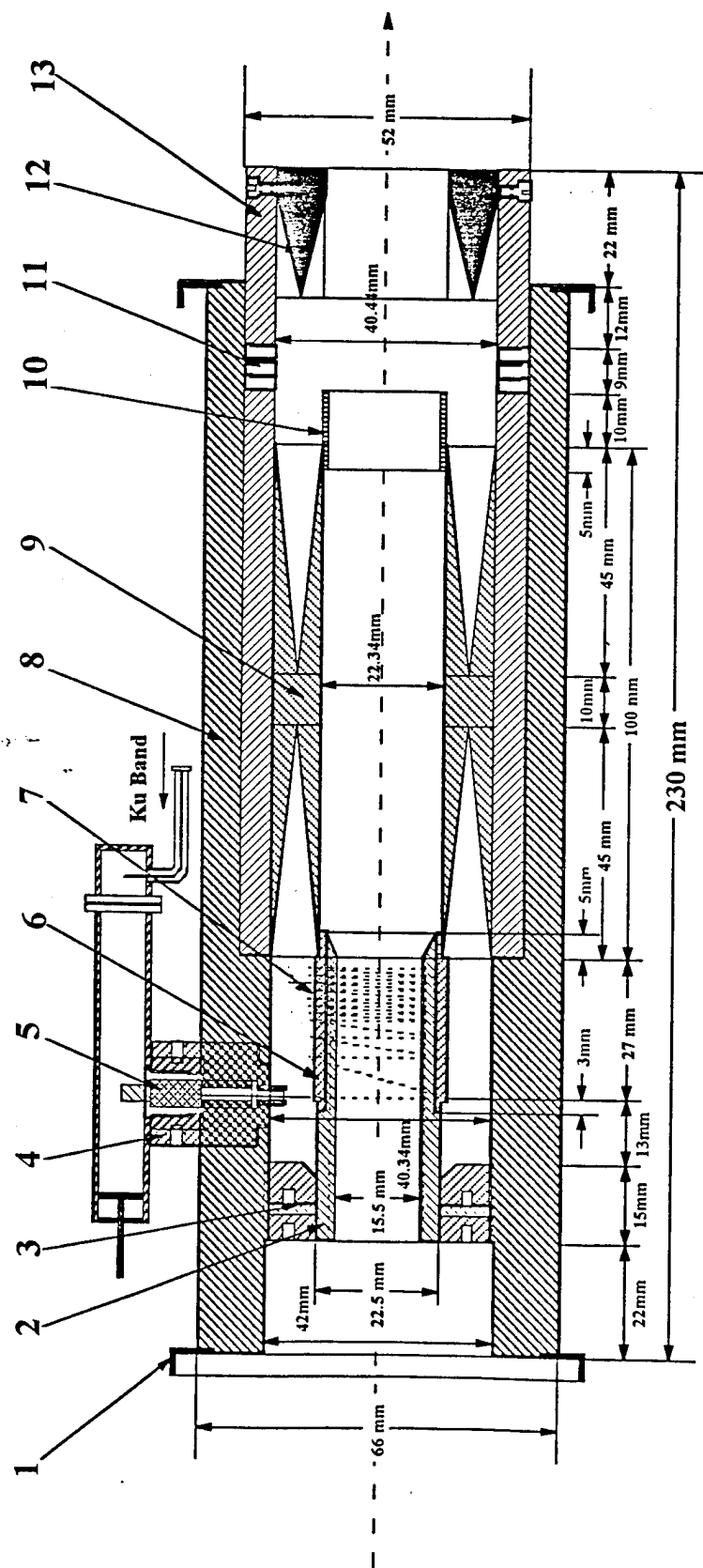


Figure 3 Assembly Configuration of the Mode Selective Circuit with an Input Coupler/TE<sub>02</sub> Mode Launcher for Gyro-TWT Interaction

1. Argon welding edge
2. Cut-off waveguide
3. Tuning plug assembly
4. Input window support
5. Input window assembly
6. Ceramic tube
7. Antenna coil
8. Body sleeve
9.  $TE_{02} \leftrightarrow TE_{01} \leftrightarrow TE_{02}$  Mode converter
10. Non- $TE_{02}$  mode suppressor
11. Mode filter
12. Attenuator
13. Transition waveguide



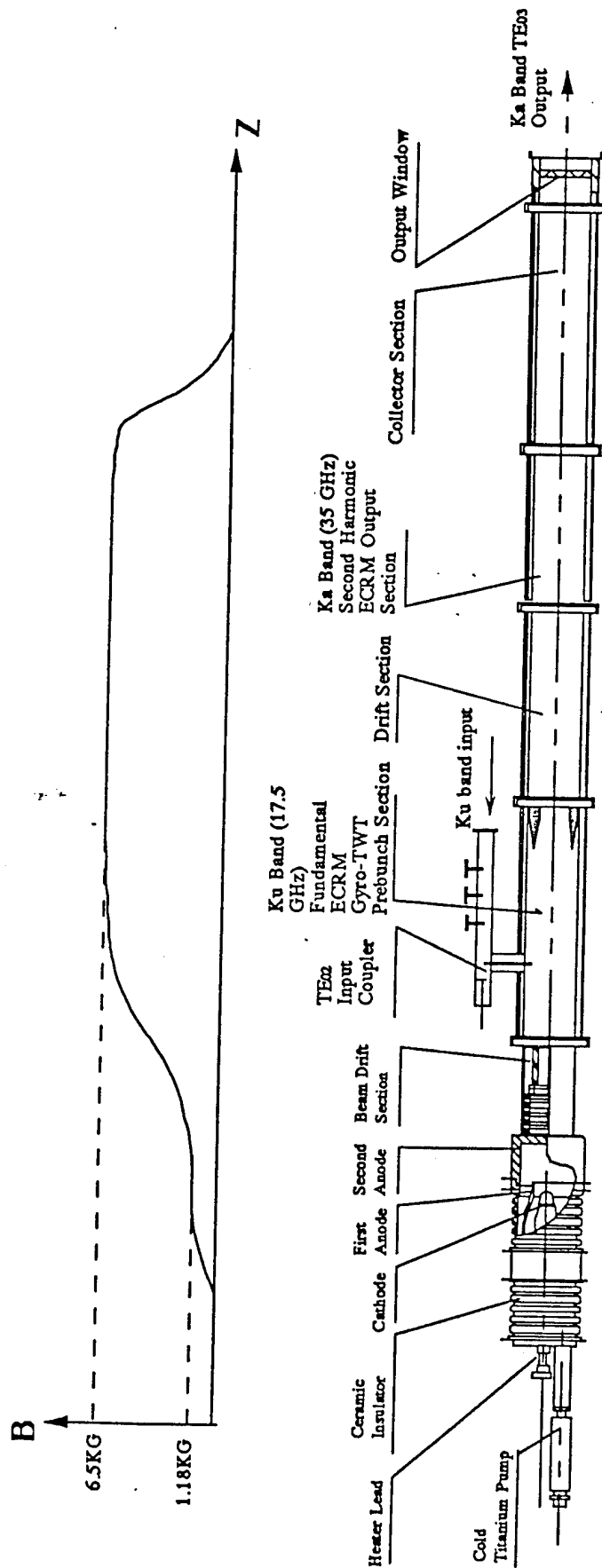


Figure 4 Proof-of-Principle Tube of the Harmonic Multiplying Gyrotron  
( In Configuration of Gyro-TWT and Phigtron )

**Table 1\* Design Parameters of the Proof-of-Principle Experiment**

	<b>Phigtron</b>	<b>Gyro-TWT</b>
<b>Output center frequency</b>	35 GHz	35 GHz
<b>Input center frequency</b>	17.5 GHz	17.5 GHz
<b>Bandwidth</b>	>50 MHz	>5%
	(phase-locking)	(instantaneous)
<b>Output power</b>	> 200KW(peak)	> 100 KW (peak)
<b>Efficiency</b>	>30%	>15 %
<b>Gain</b>	40 dB	30 dB(linear)
	(phase-locking)	25 dB(saturated)
<b>Harmonic number s</b>	2	2
<b>Length of interaction region</b>	40 cm	50 cm
<b>Output mode</b>	TE <sub>03</sub>	TE <sub>03</sub>
<b>Magnetic field</b>	6.5 kG(max.) <sup>1</sup>	6.5 kG(max.) <sup>1</sup>
<b>Gun type</b>	MIG <sup>2</sup>	MIG <sup>2</sup>
<b>Gun voltage</b>	60 kV	60 kV
<b>Gun current</b>	12 A	12 A

<sup>1</sup> Compatible with modern permanent magnets ( Nd/Fe/B).

<sup>2</sup> Magnetron Injection Gun.

\* Based on the cold-test and calculation results (K.R.Chu etal. to be published) we have designed a two-stage phigtron oscillator and a two-stage gyro-TWT amplifier for proof-of-principle demonstration. These devices will soon be in hot-test experiment.

## 4 Efficiency Enhancement of Gyrotrons by Using Depressed Collectors

High power millimeter waves sources, such as Gyrotrons and Free Electron Lasers do not presently have the efficiency of conventional tubes operating at longer wave lengths. Overall efficiency is an important consideration in various applications such as plasma heating, materials processing, etc. The Institute of Plasma Research has been actively engaged in studies on enhancement of overall efficiency by using depressed collectors.

Techniques have been developed for tailoring the electric and magnetic field configurations in the collector region, such that electrons in the spent beam would be sorted according to energy and would not turn back before getting collected. These techniques have been applied to the cases of large and small orbit gyrotrons. Designs were developed for tubes with axially and radially extracted beams, and for cavity type as well as quasi-optical type resonators for rf interaction.

A library of computer codes has been developed to assist in various stages of depressed collector design. A flowchart is given in Annexure A and a description of the codes is given in Annexure B. They help to define the regions of accessibility for electrons, and provide pre and post processors for the code which simulates electron trajectories. They help to reduce the design time and evaluate new designs in terms of collector efficiency and heat dissipation density profile. Among other things they provide insights into the behavior of the electron trajectories through three dimensional representation of an effective potential (Figure 1). Animated contours can be generated to get an overview of the effect of variations due to different parameters. A summary of the work was presented at the International Conference on Infra Red and Millimeter Waves in Sendai, Japan, in December 1994.<sup>1</sup>

A feasibility study was done for a single stage depressed collector for a gyrotron for the International Thermonuclear Experimental Reactor (ITER). Currently a design is being developed for a two stage depressed collector for it and for a 110 GHz gyrotron, in close collaboration with industry. The library of codes has been provided to Calabazas Creek Research in the form of diskettes and user manuals for the software. Consultancy is being provided to them for the design of two depressed collectors for a millimeter wave gyrotron with power output of 1 Megawatt. There is also close collaboration with the tube division of Communications and Power, Inc. (Ex Varians), for this project.

---

<sup>1</sup>Amarjit Singh, Daniel S. Weile and Victor L. Granatstein. "Simulation and Comparison of Depressed Collector Configurations for a Gyrotron". 1994 Conference Record IR & MM Waves, pp 73-74, Sendai, Japan.

**3-D Plot of Effective Potential for  
Two Depressed Collectors**

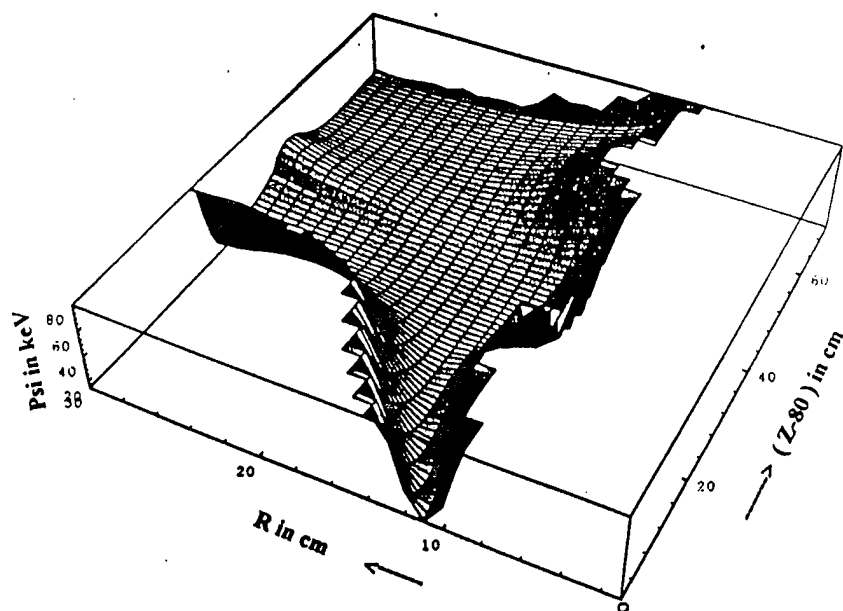
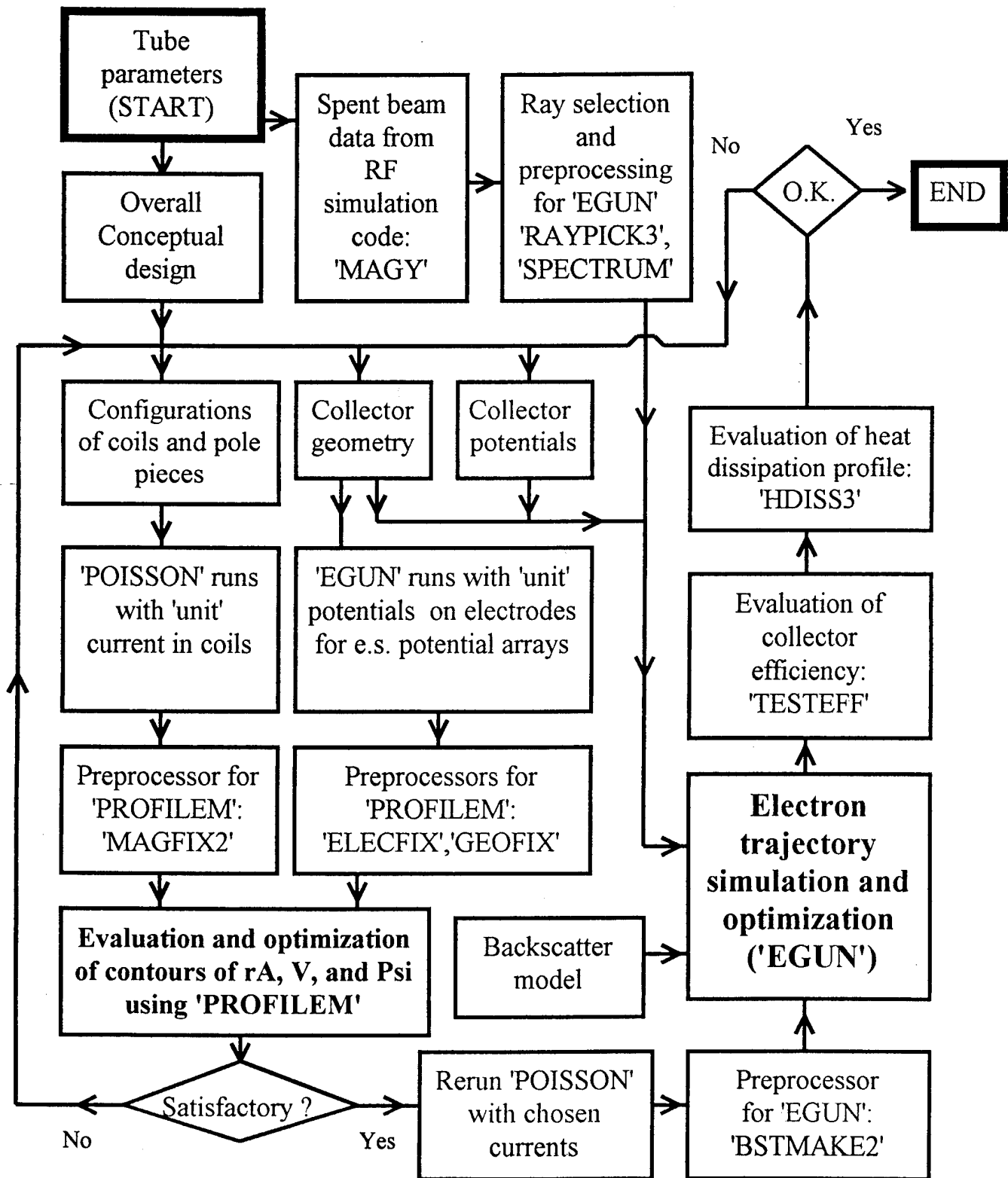


Figure 1

# Flow Diagram for Design of Depressed Collectors



## Computer Codes for Design of Depressed Collectors

At the Institute for Plasma Research, University of Maryland, we have developed a library of computer codes as aids to design of depressed collectors, especially for gyrotrons. The tasks for which we have codes now are:

- \* 'Raypick3' for preparation of data arrays regarding the spent beam for input to the code for trajectory tracing. The basic data are derived from the simulation of rf interaction. Criteria can be inserted for sampling and randomization, and calculations made for the parameters needed by the trajectory code, 'Egun'.

- \* 'Spectrum' for evaluation of the current and power spectra as a function of energy for a) the spent beam as characterised by rf simulation, and b) the representative set of rays as given by 'Raypick'.

- \* 'ProfileM' for: a) precise control of magnetic flux lines in depressed collector region, b) evaluation of contours of effective potential in the collector region, and making 2-D and 3-D plots of the same, so as to ensure collection of all rays and to give energy sorting and c) pre-processors for linking this code to the output/input of the codes, 'Poisson', and 'Egun'

- \* 'Testeff' for calculation of collector efficiency from an output file in 'Egun'.

- \* 'Hdiss3' for evaluation of the profile of heat dissipation density on the surface of the collectors. The strip width for which the density is calculated can be varied. The heat dissipation density profiles are of particular interest for elimination of potentially harmful hot spots.

## Features of ProfileM

ProfileM was programmed with a visual interface in Windows™. You enter data and make choices with user friendly devices such as dialog boxes, option buttons and action buttons. Specifically, ProfileM can:

- interactively adjust contour lines and magnetic field profiles by allowing you to change currents, potentials and canonical angular momentum and show the results of your changes in a few seconds,
- display contours and profiles against the backdrop of the device geometry so that the configuration of the fields vis-a-viz the geometry may be optimized,
- zoom into a narrower viewing area to emphasize a certain region of interest,
- create hard copies of designs with data on the electrode potentials, coil currents, and canonical angular momenta incorporated in the design so that you can keep a record of the design as it evolves,
- create text files which contain arrays that can be imported by other programs (such as Mathematica™) to draw three dimensional plots of the potential surface,
- make script files so that universal problem parameters only need to be defined by the user once and subsequently can be loaded from disk,
- make and show film loops that show how contours and profiles evolve with changing currents, potentials or the canonical angular momentum.

# TASK B: Prebunched Gyrotron Studies

## 1 Overview

In recent years, numerous theoretical and experimental investigations of gyrotrons operating near the fundamental cyclotron frequency have proven them to be reliable, efficient, high power sources of microwave and millimeter wave radiation [1, 2]. Unfortunately, a serious drawback of the classic gyrotron configuration at high frequencies is the high magnetic field level required for first harmonic operation and the associated power consumption. Thus, they are not viable candidates for some high frequency applications that require compact and lightweight tubes. One way to decrease the requisite magnetic field is to operate at an harmonic of the cyclotron frequency. Unfortunately, the efficiencies of second harmonic devices usually lag behind their first harmonic counterparts by several percent and efficiencies tend to decrease fairly rapidly with increasing harmonic number after that point.

We have recently proposed a method of pre-bunching an electron beam to enhance the efficiency in high harmonic, large-orbit devices which is based on the cusp-injection scheme [3, 4]. This device (shown in Fig. 1), which we call the axially-modulated, cusp-injected, large-orbit gyrotron, uses the axial bunching mechanism of the klystron amplifier on an annular, linearly-streaming beam to generate the pre-bunched beam [5]. The axial bunches are created ballistically after the beam passes through an input cavity which is driven with a  $TM_{mn0}$  circularly-polarized mode. The axial bunches are converted into azimuthal bunches when the beam encounters a non-adiabatic magnetic transition (cusp). If the drive frequency is at the  $m$ th harmonic of the cyclotron frequency, the net effect is that the beam will form  $m$  spokes that will rotate at the cyclotron frequency. If an output cavity that operates in a  $TE_{m11}$  mode is placed immediately after the cusp, efficient energy extraction can occur. For example, an earlier design study [5] demonstrated that an efficiency of 40% was achievable in X-Band at the fourth harmonic via an interaction between a 100 kV, 25 A electron beam and a simple  $TE_{411}$  cavity.

While this initial result is quite promising, there are some practical limits to the applicable range of parameters for this device. For example, the beam radius of the large-orbit configuration is equal to the Larmor radius, which is proportional to the perpendicular velocity for a given cyclotron frequency. Thus, the beam radius in low voltage systems decreases fairly substantially with decreasing beam energy. However, the relative radius of the maximum electric field in a cavity increases with increasing harmonic number. In fact, the electric field at radii much less than the maximum field radius varies by a factor that is proportional to the power of the harmonic number. In such systems, the achievement of the necessary field strength for efficient interaction often leads to unrealistic requirements on output cavity quality factors.

There are at least two possible ways to overcome these difficulties and design efficient, low voltage, harmonic devices. One way is to use a vane-resonator to couple various azimuthal modes together. The resultant cavity modes can support the necessary azimuthal field variation with a much lower cutoff frequency. Thus, the wall radius can be reduced considerably as compared to the smooth wall case and the interaction impedance can be significantly increased. The second approach is to pre-bunch a small-orbit beam. Axial modulation is



still a viable concept because a small orbit beam can be generated by a non-adiabatic magnetic transition that does not reverse the direction of the field. The guiding center radius can be adjusted to place the beam at a location where the electric field is relatively strong. This non-zero guiding center radius expands the number of potential modes that the beam can interact with. While this may enable us to select a desirable output mode, it also can potentially lead to additional mode competition problems. A properly pre-bunched beam, however, should help to reduce mode competition by preferentially selecting the desired operating mode. Efficiencies for both types of devices can significantly exceed those of non-prebunched beams. Yet, many of the stability problems usually associated with gyrotron amplifiers are not an issue with this novel approach.

The goal of this program is to design, build, and test a proof-of-principle experiment based on this prebunched gyrotron concept. To be of interest to applications that require compact devices, we limit our designs to voltages below 50 kV. To demonstrate moderate power levels, we have focused on designs that produce peak powers on the order of 100 kW. We have kept our design frequencies in the 5-10 GHz range in order to perform a cost effective experiment. The designs are fairly conservative and can no doubt be pushed to higher frequencies with a power that scales better than the normal expectation.

The first year's effort has been spent predominantly working on three areas. The first effort was to develop the necessary modeling tools to analyze the microwave circuits which can efficiently interact with low-voltage rotating beams in a variety of configurations. The five main codes developed or modified for this effort are described in the following section. The second task, which represented the bulk of the work, was to use these new codes along with some existing codes to design a proof-of-principle experiment that can be carried out in our laboratory. Included in the appendix are copies of two papers [6, 7] that have been submitted to journals and which describe the results of our microwave circuit designs. These papers are very briefly summarized in the next section, along with descriptions of the design work not included in the journal articles. The final task was to begin the construction of the experiment. The initial phase involved bringing additional personnel onto the project (engineers, students, etc.), identifying existing hardware that was available and compatible with the designs, and procuring additional hardware. These efforts are described in the third section.

In the final section we describe our proposed effort for the second year.

## 2 Theoretical Effort

### 2.1 Code development

Five main codes were written or enhanced in the past year to assist in the design of low voltage, prebunched gyrotrons systems. Two "driver" codes focused on the microwave input system. The first computes the field profiles, quality factors, and required drive power for  $TM_{mnp}$  dielectric-loaded, right-circular cavities. Up to three ideal dielectric regions can be introduced between arbitrary radial locations. The second code computes the field profiles for a sheath-helix structure. The input system, which will be used in the design of a broadband version of this device, can have a conducting wall inside or outside the helix (or both).

The “buncher” code uses the output from the “driver” codes to simulate the velocity modulation and ballistic bunching of the beam. It can also be used without the driver codes if the input system is a simple right-circular (unloaded) cavity. Initial uniform particle distributions in time, azimuthal angle, and axial location can be specified. Finite beam thicknesses are modeled with three layers of electrons. A predictor-corrector scheme is used to numerically integrate the particles through an acceleration region, the input cavity, the drift region, and the nonadiabatic magnetic transition. The transition uses a piecewise-linear model and unbalanced transitions can be specified. Different integration step sizes are possible in the cavity, drift, and transition regions. A Runge-Kutta algorithm is used to start the integration whenever necessary. The code outputs the phase space distribution of the particles and various statistics. In addition to calculating the average guiding center position, average velocity ratio, and the perpendicular and parallel velocity spreads, the code also computes the RMS spread in beam energy and a measure of the bunching effectiveness. This measure first computes the RMS spread in angular location, but then normalizes it so that a completely unbunched beam would yield a value of 100%. We normally report 100% minus this value, so that an unbunched beam has a bunching effectiveness of 0% and a fully bunched beam has an effectiveness of 100%. Because particles can be launched at various times, the angular location is given relative to the phase of an EM wave at the frequency of the buncher cavity.

The “VR cavity” code computes the resonant frequency, quality factor, and field profiles of a closed cavity with vane resonators. The number of terms kept in the infinite series can be specified. The usual approximation of a constant field in the slot is used to find the dispersion relation. An arbitrary phase shift between vanes can be introduced provided that it is consistent with the boundary conditions. The quality factor is computed by assuming a good copper cavity and numerically integrating the surface currents on all walls.

The “efficiency” code uses the phase-space results from the buncher code to compute the net interaction in the output cavity. There are now three ways to specify an EM field configuration. Simple right-circular field profiles can be generated internally and the fields of a VR structure can be read in from the output of the previously described code. Finally, we have modified the code to accept input from a scattering matrix code [8]. In this way, we can examine the effects of non-sinusoidal field profiles and post-cavity beam-microwave interactions on tube performance. The efficiency code uses the same numerical methods as the buncher code. A linearly-tapered magnetic field can be introduced into the region. Efficiency is computed as a function of the EM wave’s amplitude and phase. These two quantities can be swept automatically to aid in the search for optimal efficiency. The code calculates the output cavity quality factor required to achieve the specified fields.

## 2.2 Small-orbit design

The results of our small-orbit design are discussed in great detail in the first paper contained in the Appendix. In this section we highlight only the key points of the design.

The parameters of the second harmonic, small-orbit design are given in center column of Table 1. A picture of the system with a typical beam profile is given in Fig. 2. The smooth-walled output cavity has a main section length of 10 cm and a coupling lip with a radius of 1.7 cm. Simulations are carried out with the codes described in the previous

Table 1: Amplifier system parameters.

Beam Parameters	Small-orbit	Large orbit
Voltage (kV)	35	45
Current (A)	4	4
Average radius (cm)	1.18	1.13
Beam thickness (mm)	7.33	0.8
Velocity ratio ( $v_{\perp}/v_z$ )	2.28	2.20
Input Cavity		
Drive frequency (GHz)	9.9	5.5
Operating mode	TM <sub>020</sub>	TM <sub>310</sub>
Resistive Quality factor (Q)	2800	2170
Radius (cm)	2.66	1.701
Length (cm)	0.20	0.23
Magnetic Field Parameters		
Buncher guide field (kG)	0.985	-0.57
Output magnetic field (kG)	1.83	0.61
Cyclotron frequency (GHz)	4.794	1.577
Cusp width (cm)	0.50	0.38
Cavity - cusp spacing (cm)	13	30
Output field taper	-3%	13%
Output cavity		
Output frequency (GHz)	9.9	5.5
Operating mode	TE <sub>011</sub>	$\pi$ -mode
Diffraction Q	1825	1240
Resistive Q	28,580	13,430
Radius (cm)	1.864	1.763
Length (cm)	11.09	15.00
Harmonic number	2	3

section and are checked with a modified gyrokystron code [9]. With a beam thickness of 6.7% (prior to the magnetic transition), the net axial velocity spread at the output cavity entrance is 12% and the net energy spread is 3.2%. A slight decrease in the magnetic field strength throughout the output region is required to maximize efficiency. The required drive power is 840 W and an output power of over 74 kW is achieved with an efficiency of 53%. Hence, the large-signal gain is approximately 19.5 dB. The system drive curve is shown in Fig. 3. Powers as high as 78 kW can be achieved with drive powers of about 1.2 kW. The zero-drive efficiency is less than 2%. An examination of the start-oscillation currents for all the potential spurious modes indicates that only the desired operating mode is unstable at the nominal operating point. The only other mode to have a start current below 10 A is the TE<sub>111</sub> mode, but this is zero-drive stable for all magnetic fields above 1.79 kG. Simulations indicate that efficiency is fairly insensitive to beam thickness. They also predict efficiency enhancement of a few percent for larger average velocity ratios (up to  $\alpha = 3$ ).

## 2.3 Large-Orbit Design

Again, the results of our large-orbit design are discussed in considerable detail in the second paper supplied in the Appendix. In this section we summarize the design parameters at the nominal operating point and discuss operation at other harmonics.

The design parameters of the third harmonic, large-orbit design are given in the final column of Table 1. The output cavity is of the vane-resonator type and has six slots, each with a depth of 0.75 cm and a relative opening of 50%. The cavity cross-section is plotted in Fig. 4 along with beam distributions at the entrance (Fig. 4a) and exit (Fig. 4b) of the output cavity. The input cavity is assumed to contain lossless dielectric material to enhance the axial electric field at the beam. With a beam thickness of 6.7%, the net axial velocity spread at the output cavity entrance is 9.0% and the net energy spread is 3.8%. A fairly substantial increase in the magnetic field strength throughout the output region is required to maximize efficiency. The required drive power is 1.1 kW and an output power of nearly 100 kW is achieved with an efficiency of 55% (and a resultant large-signal gain of nearly 19.6 dB). Simulations indicate that this device is considerably more sensitive to beam thickness than the small-orbit device. On the other hand, the post-cusp velocity spread induced by the buncher cavity is considerably less for the large-orbit beam than for the previous system.

We have also taken a preliminary look at efficiency enhancement in higher harmonic systems with comparable beam voltages. In Fig. 5a, we plot the simulated efficiency of a large-orbit device as a function of harmonic number. The point on the dashed line at the third harmonic corresponds to the system described in the previous section. For the other harmonic results, the magnetic field and beam parameters are fixed at the values given in Table 1. However, the cavity-cusp spacing, and the cavities' harmonic number, radial dimensions, and number of (output) vanes are adjusted to the appropriate values. Furthermore, the output cavity quality factor is adjusted to optimize efficiency (Fig. 5b). The figure also indicates the simulated efficiency achievable for a zero thickness beam. With the exception of the second harmonic result, the finite beam thickness results in an efficiency decrease of about 10 - 12%.

Figure 5 clearly demonstrates the rapid decline in tube efficiency with harmonic number which is inherent in these systems. This problem is exacerbated by the dramatic rise in the required quality factor. For example, the sixth harmonic design presented here requires a quality factor over three times the resistive  $Q$  of a copper cavity. While a full optimization of system design at each harmonic (e.g. adjustment of the output cavity length, magnetic field tapering, etc.) would undoubtedly improve the indicated performance somewhat, the fourth harmonic is probably the highest viable harmonic number for the 45 kV beam considered here.

## 2.4 Broadband bunching investigation

An extension of this device that we have just started to examine is designed to produce similar efficiency enhancement in a broadband configuration. The basic idea is to replace the input cavity with a slow wave structure and the output cavity with a gyrotwistron-like output waveguide [10]. Initial results with the beam parameters of the small-orbit configuration indicate that bunching over a wide range of frequencies is possible with only a slight

Table 2: The electron gun parameters.

Parameter	Value
Average cathode radius (cm)	3.0
Cathode thickness (mm)	2.0
Cathode loading (A/cm <sup>2</sup> )	1.0
Cathode magnetic field (G)	260
Magnetic compression	4.0
Peak electric field (kV/cm)	24

increase in the resultant velocity spread as compared to the input cavity approach. Sheath helices can also be used in principle to excite the fields required for the large-orbit configuration. We are now in the process of modifying our codes to model the traveling-wave output structure.

## 2.5 Electron gun design

We have been considering three slightly different electron gun configurations in the course of this investigation. EGUN [11] was used for all simulations. The first, pictured in Fig. 6, is a gun designed to produced 2 A at 35 kV. The second configuration is similar in shape but has a decreased anode-cathode gap and is designed to operate at 4 A and 45 kV. The space-charge limiting current is simulated to be 6 A. A summary of the gun design values for the first configuration is given in Table 2. The peak electric field on the cathode is 24 kV/cm.

We are currently working on a higher compression design that can be used to power the third harmonic large-orbit design. It is believed that the same cathode can be used for both experiments.

## 3 Experimental Effort

With the completion of the two design studies presented in the previous section, we have just recently turned our attention to the proof-of-principle experiment. Our initial effort to assemble a test bed has included work on a modulator, the magnetic field system, the vacuum system, microwave components, and test equipment. Progress in each of these areas is described in the following paragraphs.

We have obtained a PFN-type modulator that has a maximum peak power of about 950 kW and a pulse duration of either 0.5  $\mu$ s or 5  $\mu$ s. We will use the modulator in the long pulse-length mode. We have repaired some minor problems and characterized the modulator performance as a function of load impedance. Optimal performance is achieved with a pulse voltage of 49 kV and a current of about 19 A (at 90% of the supply's maximum output). Since the beam current is in the 2-6 A range, a shunt resistor will be used to match the PFN impedance.

We have identified over a half-dozen magnetic field coils that are available to us and that will be easily able to handle the field requirements of the large-orbit design. We are just

starting to evaluate their ability to work at the higher magnetic field required for the small-orbit design. If they prove to be inadequate, we will attempt to procure several water-cooled magnets. We have also identified a few power supplies that can be used to energize some of the coils but have ordered three more supplies. We have obtained an iron plate that, with a few modifications, should prove adequate for the non-adiabatic transitions of both designs.

We have obtained one 60  $\ell$ /s ion pump/controller set and have access to roughing and bake-out pumps in addition to leak-checking hardware. We are in the process of ordering additional vacuum hardware.

We have identified sources that are available to us and cover the range from 8.5–10 GHz. Two of the sources are pulsed magnetrons with considerably more power than required but pulse lengths of only about 2  $\mu$ s. Another source (near 9.9 GHz) produces a few kilowatts and can be run CW. We intend to order a 5.4 – 5.8 GHz magnetron that can be integrated into an existing power supply and used for the large-orbit design. We are also in the process of ordering a selection of microwave components that will be required to perform the proof-of-principle experiment.

Finally, we have begun to accumulate the necessary test equipment that will be required to successfully complete this study (e.g. a computer, interface hardware, oscilloscopes, etc.)

## 4 Proposed Work for the Next Year

We have developed an ambitious schedule for next year which should allow us to begin microwave amplifier experiments by the beginning of the third year. We intend to first try to build and test the second harmonic small-orbit design, primarily because more of the hardware for this design is already on hand in our Institute. With the exception of the required circuit magnetic field, the small-orbit components are somewhat easier to construct than the corresponding large-orbit components. We will continue to improve our modeling capabilities and explore other pre-bunched gyrotron designs. We have briefly summarized the major tasks proposed for next year below.

1. Modify the “efficiency” code to automatically search for the maximum efficiency as a function of field amplitude and phase.
2. Modify the “buncher” code to accept input from the scattering matrix code to allow coaxial input cavities and to investigate the effects of fringing fields.
3. Modify the “output” code to model traveling wave interactions.
4. Modify the “helix” and “buncher” codes for non-symmetric modes.
5. Modify the “buncher” code to accept input from EGUN simulations.
6. Use HFSS to model the input cavities.
7. Design and evaluate broadband amplifier configurations.
8. Re-evaluate previous designs with the improved codes.

9. Finalize electron gun design, order emitter strip, and construct remaining components.
10. Complete procurement of experimental hardware.
11. Construct and cold-test input and output cavities for small-orbit design.
12. Design and construct vacuum jacket. Utilize a gate-valve if at all possible to keep gun under vacuum during tube rebuilds.
13. Construct complete magnetic field system and characterize field profile in all regions, particularly near the iron plate.
14. Construct the vacuum-compatible microwave circuit.
15. Construct beam diagnostics.
16. Characterize beam performance.
17. Construct microwave diagnostics.
18. Initiate microwave amplifier experiment (most likely not to begin until the third year).

## References

1. R. S. Symons and H. R. Jory, *Advances in Electronics and Electron Physics*, C. Marton, ed. (New York: Academic Press, 1981), vol. 55, Ch. 1, p. 1.
2. V. L. Granatstein, M. E. Read, and L. R. Barnett, *Infrared and Millimeter Waves*, K. Button, ed. (New York: Academic Press, 1981), vol. 5, Ch. 5, p. 267.
3. M. J. Rhee and W. W. Destler, "Relativistic electron dynamics in a cusped magnetic field," *Phys. Fluids*, vol. 17, p. 1574, 1974.
4. W. W. Destler, E. Chojnacki, R. F. Hoeberling, W. Lawson, A. Singh, and C. D. Striffler, "High-power microwave generation from large-orbit devices," *IEEE Trans. Plasma Sci.*, vol. 16, pp. 71-89, 1988.
5. W. Lawson and W. W. Destler, "The axially modulated, cusp-injected, large-orbit gyrotron amplifier," *IEEE Trans. Plasma Sci.*, vol. 22, pp. 895-901, 1994.
6. W. Lawson, A. Grigoropolous, A. Liu, G.P. Saraph, J. Rodgers, and W. W. Destler, "Design of a high efficiency, low voltage, axially modulated, cusp-injected, second harmonic, X-band gyrotron amplifier," submitted to *IEEE Trans. Plasma Sci.*, July 1995.
7. W. Lawson, W. W. Destler, A. Fernandez, A. Liu, J. Rodgers, and J. Weinstein, "Design of an efficient, low voltage, third harmonic, large-orbit gyrotron amplifier with a vane resonator for output cavity," submitted to *IEEE Trans. Electron Devices*, October 1995.
8. W. Lawson and P. E. Latham, "The scattering matrix formulation for overmoded coaxial cavities," *IEEE Trans. Microwave Theory & Tech.*, vol. 40, pp. 1973-1977, 1992.
9. P. E. Latham, W. Lawson, and V. Irwin, "The design of a 100 MW, Ku-band second harmonic gyrokystron experiment," *IEEE Trans. Plasma Sci.*, vol. 22, pp. 804-817, 1994.
10. W. Lawson, P. E. Latham, J. P. Calame, J. Cheng, B. Hogan, G. S. Nusinovich, V. L. Granatstein, and M. Reiser, "High power operation of fundamental-mode and second harmonic gyrotwistrons," *J. Appl. Phys.*, vol. 78, pp. 550-559, 1995.
11. W. B. Herrmannsfeldt, "Electron Trajectory Program," SLAC Report 226, November 1979.



## **TASK C:**

### **Studies of Cyclotron Maser Amplifiers with Trochoidal Electron Beams (Trochotrons)**

After developing the linear theory of trochotrons the quality of trochoidal electron beams has been studied. Two concrete designs of electron guns have been analyzed intended for operation at 35 GHz in second harmonic trochotrons. It was shown that trochoidal electron beams can be formed with large ratios of perpendicular to parallel (drift) velocity and very small spread in drift velocities. This makes such beams suitable for utilization in trochotron-traveling-wave amplifiers.

A paper submitted for publication in the 6th Special Issue of the IEEE Transactions on Plasma Science on High-Power Microwaves is included as an Appendix.

## APPENDIX

### Papers Pertaining to this Research

- TASK A: "Phase-locking of a second-harmonic gyrotron oscillator using a quasi-optical circulator to separate injection and output signals"
- TASK B: "Design of a high efficiency, low voltage, axially modulated, cusp-injected, second harmonic, X-band gyrotron amplifier"
- "Design of an efficient, low voltage, third harmonic, large-orbit gyrotron amplifier with a vane-resonator output cavity"
- TASK C: "On the design of electron guns for cyclotron resonance masers utilizing trochoidal electron beams (trochotrons)"

# Phase-Locking of a Second-Harmonic Gyrotron Oscillator Using a Quasi-Optical Circulator to Separate Injection and Output Signals\*

H.Z. Guo, D.J. Hoppe, MEMBER, IEEE, J. Rodgers, R.M. Perez, J.P. Tate, MEMBER, IEEE, B.L. Conroy, V.L. Granatstein, FELLOW, IEEE, A. Bhanji, P.E. Latham, MEMBER, IEEE, G.S. Nusinovich, SENIOR MEMBER, IEEE, M. Naiman, and S.H. Chen

**Abstract**—Phase-locking in a 34.5 GHz special complex cavity gyrotron oscillator operating at the second harmonic of the electron cyclotron frequency was studied. Injection of the locking power was made via a quasi-optical circulator connected to the gyrotron output. Locking bandwidth was measured by comparing the phase of the injection signal and output signal using a balanced mixer. Locking was observed with input power level as low as 40 dB below the gyrotron output power. The locking bandwidth is, however, narrower than in gyrotrons operating at the fundamental cyclotron frequency which may be attributed to the longer resonant cavity in the second harmonic gyrotron and the corresponding larger value of external quality factor. The measurements are roughly in agreement with predictions of Adler's phase-locking equation which is given for our system in terms of powers propagating in the output waveguide toward and away from the gyrotron cavity.

## I. INTRODUCTION

Efficient, high power, coherent millimeter wave sources are currently needed for satellite and space communications and for imaging radar to be used in space exploration [1]. A weakly relativistic (electron energy  $< 100$  keV) gyrotron phase-locked oscillator operating at high harmonic of the electron cyclotron frequency (harmonic number  $s \geq 2$ ) has been considered as one of the appropriate source choices for these applications for the following reasons:

- (1) the transverse dimensions of both the electron beam and the circuit can be much larger than in klystrons or slow-wave microwave tubes because of the ability of gyrotrons to operate in fast wave, higher-order, transverse electric modes, resulting in higher average and peak power rating at a given operating frequency;
- (2) the moderate voltage requirement avoids the need for large insulators or electron accelerator sections; and
- (3) the required magnetic field can be reduced by the harmonic factors compared with gyrotrons operating at fundamental cyclotron frequency, potentially making gyro-devices compatible with modern permanent magnet technology up to operating frequencies of approximately ( $s \times 20$ ) GHz.

\*The research described in this paper was carried out in part by the Jet Propulsion Laboratory, California Institute of Technology, under a contract with the National Aeronautics and Space Administration; in addition, this work was supported in part by the DoD Vacuum Electronics Initiative and managed by the Air Force Office of Scientific Research under Grant AFOSR-91-0390.

H.Z. Guo, J. Rodgers, V.L. Granatstein, P.E. Latham, G.S. Nusinovich, M. Naiman and S.H. Chen are with the Institute for Plasma Research, University of Maryland, College Park, MD 20742.

D.J. Hoppe, R.M. Perez, B.L. Conroy, and A. Bhanji are with the Jet Propulsion Laboratory, Pasadena, CA 91109. J.P. Tate was with the University of Maryland and is now with Florida A&M University, Tallahassee, FL 32307.

Recently, major advances have been reported in gyrotrons operating at harmonics of the cyclotron frequency. High efficiency and high power have been achieved in free running second harmonic gyrotron oscillators operating in the millimeter-wave band [2-4]. Furthermore, there have been successful demonstrations [5,6] of phase-locked gyrotrons operating at the fundamental cyclotron frequency. However, no phase-locked harmonic gyrotron operation had been reported prior to the present paper.

In this paper we report the operation and measurement of a high power ( $\sim 100$  kW) second harmonic gyrotron phase-locked by signal injection through the output window using a quasi-optical circulator system [7] to separate the input and output signals. Section II gives a brief description of the second harmonic gyrotron and the arrangement of the phase-locking experiment. Section III discusses the pertinent theory of phase-locking taking into account reflection of the injected signal at the entrance to the gyrotron cavity; requirements on the flatness of the voltage pulse applied to the gyrotron are also discussed. In Section IV the results of the phase-locking experiment are presented and compared with theoretical predictions. Finally, a summary is presented in Section V.

## II. DESCRIPTION OF THE GYROTRON AND THE EXPERIMENTAL ARRANGEMENT

### A. The Second-Harmonic Gyrotron

A second-harmonic gyrotron which features a novel complex cavity as its beam-wave interaction structure [2] was used for the demonstration of phase-locking. The parameters of this gyrotron, GY-32, are shown in Table 1. Figure 1 is a cross-sectioned drawing of the gyrotron tube along with a typical magnetic field profile. The special complex cavity consists of five parts as depicted in Fig. 2. Part 1 and part 2 are uniform circular waveguide sections with their inner radii denoted by  $a$  and  $b$ , respectively. These sections are designed to operate, respectively, in the  $TE_{02}$  and  $TE_{03}$  modes. In order to couple these two modes into one normal mode of a complex cavity the eigenfrequencies of these two partial modes must be the same. This is accomplished by choosing radii  $a$  and  $b$  to satisfy the condition

$$\frac{\mu_{02}}{a} = \frac{\mu_{03}}{b} = k_c, \quad (1)$$

where eigennumbers  $\mu_{02}$  and  $\mu_{03}$  are roots of the equations  $J'(\mu_{02}) = J'(\mu_{03}) = 0$ ,  $J_0$  is the zero order Bessel function and  $k_c$  is the cutoff wavenumber, which is the same

for both modes. Then, if the lengths of both sections are also equal that gives closely matched axial wavenumbers for both modes; thus, one can suppose that in a complex cavity these two partial modes will have closely matched eigenfrequencies.

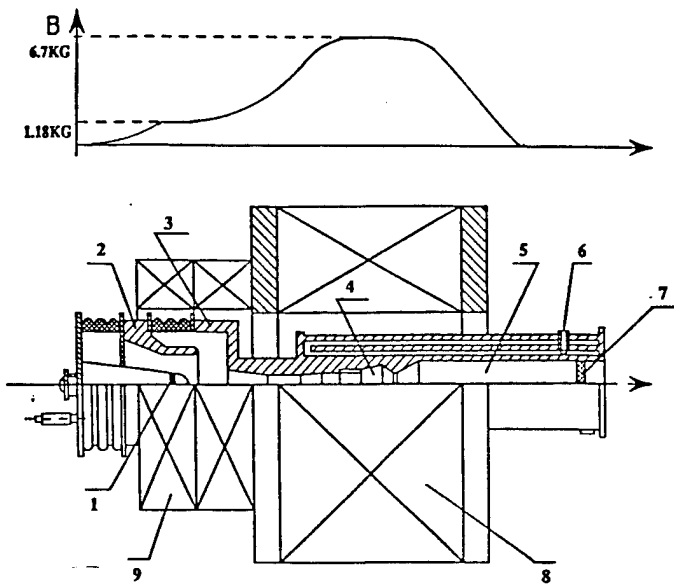


Fig. 1. Cross-sectional drawing of the GY-32 gyrotron tube along with a typical magnetic field profile: 1) cathode, 2) control anode, 3) second anode, 4) complex cavity, 5) beam collector, 6) water cooling jacket, 7) output window, 8) main magnetic field coils, 9) gun coils.

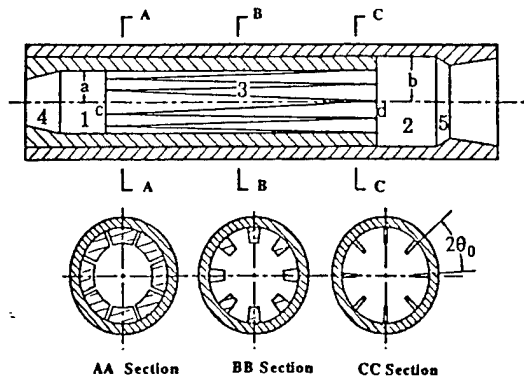


Fig. 2. Special complex cavity with internal mode converter for transforming  $TE_{02}$  to  $TE_{03}$ .

To provide a coupling between these two modes a slotted waveguide with a gradually changing cross section is used (part 3). This part is composed of a main waveguide of radius  $a$  and  $N$  slotted branch waveguides. The angle subtended by each slot,  $2\theta_0$ , varies slowly from 0 to  $2\pi/N$  over the length  $cd$ ; the depth of each branch waveguide is constant and equal to  $(b - a)$ . Thus, the gradually changing slotted waveguide efficiently converts a  $TE_{02}$  mode to

a  $TE_{03}$  mode. The three parts described above together with part 4 (cutoff section) and part 5 (diffraction output section) form a resonator. Good mode selectivity results from this kind of complex cavity for the following reasons:

- (1) The radial metallic fins at one end of the mode converter function as a mode filter. This is because modes which have a radial component of rf electric field may not be excited in the presence of the radial metallic sheets.
- (2) The mode converter functions as mode isolator. With the design criterion applied to this case, only one pair of modes ( $TE_{02}$  and  $TE_{03}$ ) will be coupled and form a normal mode for the whole system.

Table 1. Performance parameters of the GY-32 gyrotron.

Harmonic Number	2
Beam Voltage	40-60 kV
Frequency	34.5 GHz
Beam Current	8-11 A
Peak Output Power	80-230 kW
$\alpha = v_{\perp}/v_{\parallel}$	1.5
Efficiency	~35%
Quality Factor, $Q$	2000
Ohmic Quality Factor, $Q_{ohm}$	10,000
Mode Purity ( $TE_{03}$ mode)	>90%

Due to the superior mode selectivity of the special complex cavity, stable, efficient, harmonic gyrotron operation and high output mode purity result. Both of these are vital for realization of the proposed phase-locking. A calibrated  $TE_{0n}$  water calorimeter placed at the output of the gyrotron verified that greater than 95% (limit of calorimeter accuracy) of the power was in the symmetric TE modes. Spectral analysis of the output power also showed that the  $TE_{03}$  signal was at least 25 dB above any other TE modes resulting in an estimated  $TE_{03}$  purity of greater than 90%. It would have been more difficult to achieve the required stability of operation in a more usual smooth-wall cavity gyrotron operating at a harmonic of the cyclotron frequency because of mode competition problems. Also, the phase-locking arrangement in the present study employed a quasi-optical circulator for separation of injection signal from the gyrotron output signal, and this circulator has critical demands on gyrotron output mode purity for its effective operation.

Evidence for the stability of gyrotron operation is shown in Fig. 3. Figure 3(a) shows a typical modulator voltage and current pulse; 3(b) is a detected sample of the gyrotron rf output; 3(c) is the gyrotron output frequency spectrum; and 3(d) shows the output mode pattern recorded on a liquid crystal display. All of the above traces were taken prior to injecting the phase-locking signal (i.e., the gyrotron was in a free-running condition). Since gyrotron shot-to-shot stability and instantaneous frequency stability were of great importance, gyrotron output power was traded off for increased stability by keeping the beam current and the

beam voltage at the lower end of the values shown in Table 1. Lower current reduces beam space charge thereby increasing the coherence of the electron cyclotron phase bunching. Lowering the voltage had the effect of reducing shot-to-shot pulse height fluctuations in the modulator to approximately one percent. The gyrotron system operating parameters for the phase-locked experiment are shown in Table 2.

Table 2. Operating parameters for the phase-locked gyrotron experiment.

Beam Voltage	42-45 kV
Beam Current	8 Amps
Frequency	34.52 GHz
Output Power	80-100 kW
Gun Field	1.15 kG
Cavity Field	6.5 kG
Repetition Rate	43 Hz
Pulse Width	7 $\mu$ s

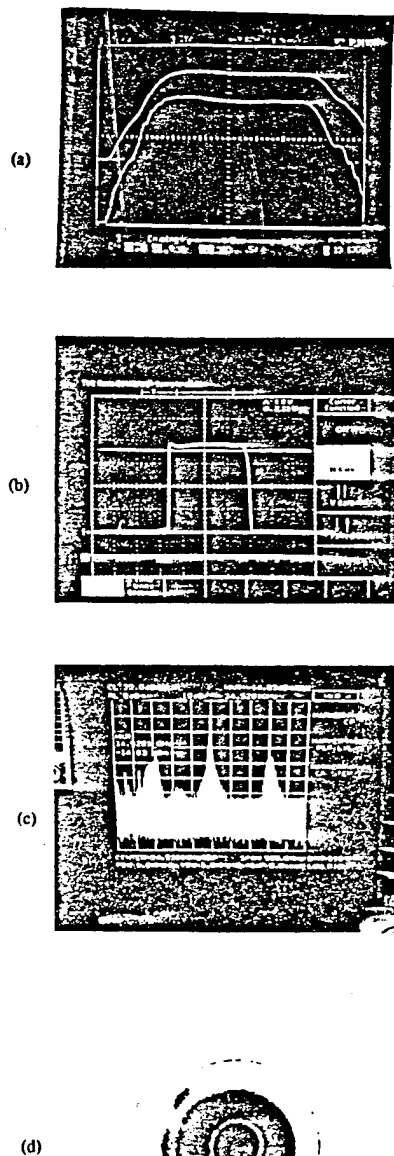


Fig. 3. Stable operation of the GY-32 gyrotron. (a) Top trace is the modulator voltage, 10 kV/div; bottom trace is the beam current, 1 A/div; horizontal time axis, 1  $\mu$ sec/div. (b) Detected gyrotron output pulse. (c) Spectrum analyzer display of gyrotron output from HP11970A waveguide mixer. The sidebands shown are the second axial mode of the complex cavity generated during the rise of the beam pulse. (d) Mode pattern produced by gyrotron output in  $TE_{03}$  mode.

### B. Experimental Arrangement

A block diagram of the phase-locked system is shown in Fig. 4. A synthesized microwave generator amplified by a 100-watt traveling wave tube amplifier (TWTA) provided the injection signal. The signal transmission path included a conventional waveguide isolator providing more than 35 dB of isolation, a directional coupler for sampling the injection signal, and a smooth-wall dual-mode horn providing a gaussian beam for launching into the quasi-optic system.

The quasi-optic circulator is depicted in detail in Fig. 5. The microwave beam was reflected off a flat plate, focused by an ellipsoidal mirror with focal lengths of 24 and 48 inches, and then redirected towards a polarized grid. The grid was fabricated by printing 0.00615 inch copper strips on 0.0123 inch centers on a 0.189 inch thick disk of fused quartz. The beam then passed through the circulator which consists of a 5.75 inch diameter disk of ferrite material, TransTech G-4259, biased with a 1 kG NDFE permanent magnet. The thickness of the disk was chosen to be 0.344 inches, producing a 45 degree Faraday rotation of the microwave beam as it passes through the disk. Fused quartz matching layers of thickness 0.0425 inches were employed on each side of the ferrite disk in order to match to free space. The beam was then injected into the high power overmoded waveguide system via an identical ellipsoid and system of flat mirrors.

The high power overmoded waveguide system consists of a series of circular waveguide mode converters which changed the injected beam from the  $HE_{11}$  gaussian mode to the  $TE_{03}$  gyrotron operating mode. Due to geometrical/mechanical considerations a mode converter system similar to that considered by Doane [8] was employed. The 1.970 inch diameter output waveguide of the gyrotron was nonlinearly tapered to 1.400 inches, where a four-ripple  $TE_{03}$ - $TE_{02}$  mode converter was inserted. A further taper to a 1.00 inch diameter was included and followed by a four-ripple  $TE_{02}$ - $TE_{01}$  mode converter. The conversion efficiency of these devices each exceeded 96%. The guide was then bent through an angle of  $54.5^\circ$  over an arc length of 20.0 inches converting the  $TE_{01}$  mode to the  $TM_{11}$  mode. Since the bend used a sinusoidal curvature distribution rather than a constant radius of curvature, an efficiency of 99.9% was achieved. Finally, a corrugated  $TM_{11}$ - $HE_{11}$  mode converter and horn assembly was used to generate a gaussian beam with the correct waist size to couple into the quasi-optical system [9]. All of the mode

conversion efficiencies were computed and verified qualitatively by far field pattern measurements. An overmoded directional coupler was also included in the waveguide system, providing test signals for a crystal detector and spectrum analyzer.

The gyrotron output followed the reverse path back to the Faraday rotator where it underwent another 45 degree rotation. Since it was then cross-polarized to the grid, the high power beam was transmitted through the grid and was absorbed by a free-space load. The quasi-optic circulator system including the mode converters was measured to have an insertion loss of 1 dB and an isolation of greater than 25 dB. The isolation was measured by injecting signals into the injection signal horn and into the TE<sub>01</sub>-TM<sub>11</sub> mode converter using a mode launcher and measuring the transmission coefficient in both directions using an HP8510 ANA. All cross-polarization effects introduced by the mirrors, horns, and waveguide system are therefore included in the measurement. Waveguide losses reduced the injection signal an additional 1 dB.

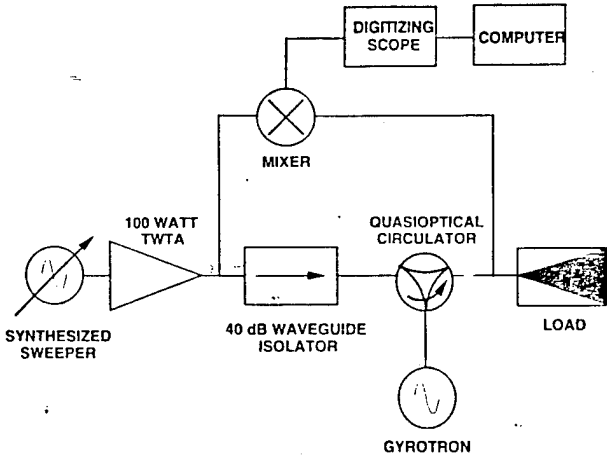


Fig. 4. Block diagram of the experiment.

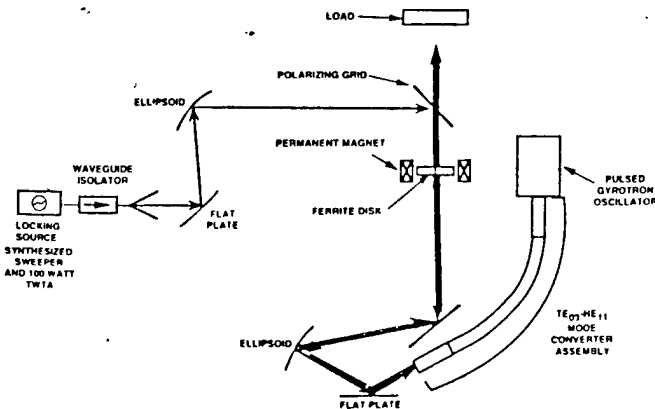


Fig. 5. Quasi-optical circulator configuration.

A small portion of the gyrotron output power was received by a horn antenna located near the free-space load and was sent to the input port of a balanced mixer. There it was combined with a sample of the injection signal from the waveguide coupler located at the TWTA output. The resulting mixer output voltage which was proportional to the instantaneous phase difference between the output and injection signals, was fed into a digitizing oscilloscope. The digitized data were recorded by a computer and stored for later analysis. Crystal detector waveforms and spectrum analyzer displays were also obtained from a branch circuit in the gyrotron output waveguide.

### III. THEORY PREDICTIONS: PHASE-LOCKING EQUATION AND DEMANDS ON GYROTRON POWER SUPPLIES

#### A. Phase-locking Equations

In order to obtain the phase-locking condition in a direct manner, we start from the gyrotron operation equations presented in reference [10]. The reduced gyrotron equations, which describe an annular electron beam interacting with a circular TE<sub>mn</sub> mode near cutoff, have been described in a number of papers [11-15]. Here we simply write down the pertinent results. For operation at the *s*th harmonic, the wave equations are

$$\left(\frac{d}{d\tau} + \frac{1}{2}\right) F = IFg_r(F) + \frac{A}{2} \cos \psi \quad (2a)$$

$$\frac{d\psi}{d\tau} = \beta - Ig_i(F) - \frac{A}{2F} \sin \psi \quad (2b)$$

where  $g = g_r + ig_i$  is the gain functional defined by

$$g(F) = -\frac{1}{F} \int_{-\infty}^{\infty} d\xi f(\xi) \langle p^s e^{i\phi} \rangle.$$

The angle brackets denote an average over initial phase  $\phi$  uniformly distributed between 0 and  $2\pi$ . In these equations,

$$p = \frac{p_{\perp}}{p_{\perp 0}}$$

is the perpendicular momentum normalized to its initial value,

$$\phi = \omega t - s\phi_{gp}$$

is the slowly varying gyrophase ( $\phi_{gp}$  is the actual particle gyrophase),

$$\xi = \frac{2z}{L},$$

is normalized distance where  $L$  is the length of the cavity as determined by the Gaussian axial distribution,

$$f(\xi) = e^{-\xi^2} = e^{-(2z/L)^2},$$

and  $I$  is the normalized current; i.e.,

$$I = \omega T_p \sqrt{\frac{2}{\pi}} \frac{Q I_b}{I_A} \left[ \frac{1}{(s-1)!} \left( \frac{sv_{\perp 0}}{2c} \right)^{s-1} \right]^2 \frac{J_{m\pm s}^2(k_{\perp} r_g)}{J_m^2(\nu_{mn}(\nu_{mn}^2 - m^2))} \quad (3)$$

where  $T_p = L/v_{z0}$  is the transit time,  $v_{z0}$  and  $v_{\perp 0}$  are the axial and perpendicular velocities, respectively,  $c$  is the speed of light,  $\Omega_{e0}$  is the initial relativistic cyclotron frequency,  $I_b$  is the beam current,  $I_A = 4\pi\epsilon_0 m_0 \gamma_0 v_{z0} c^2 / q$  is the Alfvén current in mks units with  $q$  and  $m_0$  the electron charge and rest mass, respectively,  $Q$  is the loaded quality factor of the resonator,  $k_{\perp}$  is the perpendicular wave number ( $k_{\perp} \approx \omega/c$  since we are near cutoff),  $r_g$  is the guiding center radius,  $\nu_{mn}$  is the  $n$ th zero of  $J'_m$ , the derivative of the  $m$ th order Bessel function, and  $m$  is the azimuthal mode number. The normalized field amplitude,  $F e^{-i\psi}$ , is given in terms of the actual field as

$$F e^{-i\psi} = \frac{E_0}{B_0} \frac{\omega T_p}{2v_{\perp 0}/c} \frac{1}{s!} \left( \frac{sv_{\perp 0}}{2c} \right)^{s-1} J_{m\pm s}(k_{\perp} r_g)$$

where the perpendicular component of the electric field,

$$\mathbf{E}_{\perp} \equiv \text{Re} \{ E_0 k_{\perp}^{-1} \hat{z} \times \nabla_{\perp} J_m(k_{\perp} r) \exp[i(m\theta - \omega t)] \},$$

defines  $E_0$ , and  $\psi$  is the slowly varying wave phase with respect to the phase of the injected signal. The normalized frequency mismatch,  $\beta$ , is given by

$$\beta = Q \frac{\omega_r - \omega}{\omega_r} \quad (4)$$

where  $\omega_r$  is the real part of the complex cold cavity resonant frequency. Its imaginary part, which is responsible for losses, is described by the term  $1/2$  in the brackets on the left-hand side of Eq. (2a); note that in Eq. (2),  $\tau$  is the slowly varying time,  $\tau = \omega t / Q$ . Finally,  $A$  is proportional to the field injected into the cavity from an external source.

As discussed in the introduction, this paper is specifically addressed to phase-locking of a harmonic gyrotron with external injection. In this respect, the dependence of the locking bandwidth  $\Delta f_L$  on the input and output power is of practical interest. This quantity can be estimated by setting  $d\psi/d\tau = 0$  in Eq. (2b). Then, we can obtain the following formulae for the maximum and minimum detuning:

$$\beta_{\max} = I g_i + \frac{A}{2F} = Q \frac{\omega_r - \omega_{\min}}{\omega_r} \quad \text{for } \sin \psi = 1 \quad (5)$$

$$\beta_{\min} = I g_i - \frac{A}{2F} = Q \frac{\omega_r - \omega_{\max}}{\omega_r} \quad \text{for } \sin \psi = -1 \quad (6)$$

Now, if we assume that at both  $\beta_{\max}$  and  $\beta_{\min}$  the imaginary part of the gain function,  $g_i$ , and the normalized field amplitudes are the same, then we can obtain the following approximate formulae for the locking bandwidth,

$$\omega_{\max} - \omega_{\min}: \quad \frac{A}{F} \cong Q \frac{\omega_{\max} - \omega_{\min}}{\omega_0} \quad (7)$$

and, for the dependence of phase on the frequency:

$$\psi(\omega) = \arcsin \frac{2(\omega - \omega_0)}{\omega_{\max} - \omega_{\min}} \quad (8)$$

where the 'hot' resonant frequency of the cavity is  $\omega_0$  and  $\omega_0 \approx \omega_r$ .

Equation (8) together with Eqs. (5) and (6) indicates that the phase traverses 180 degrees as the signal frequency swings through the full lock bandwidth. This will be important in demonstrating that phase-locking was accomplished during the experiments by injecting an external signal that is swept in frequency.

The locking bandwidth defined by Eq. (7) coincides with Adler's relation [16]. Let us interpret this relation in terms of the input and output power flows propagating in our system in the same waveguide since these power flows can be measured in the experiment. For this purpose let us recall that, according to reference [17], the flow of the power into the cavity,  $P_{\text{cav}}$ , is related to the flow of the incident wave power,  $P_{\text{in}}$ , as

$$\frac{P_{\text{cav}}}{P_{\text{in}}} = \frac{4Q_e/Q_{\text{ohm}}}{(1 + Q_e/Q_{\text{ohm}})^2 + \Delta^2} \quad (9)$$

and in the stationary regime this power,  $P_{\text{cav}}$ , is equal to the power of ohmic losses in the cavity,

$$P_{\text{cav}} = P_{\text{ohm}} = \frac{\omega}{Q_{\text{ohm}}} A^2 V. \quad (10)$$

In Eqs. (9) and (10),  $Q_e$  and  $Q_{\text{ohm}}$  are, respectively, the external and ohmic quality factors and are related by  $Q_e^{-1} = Q^{-1} - Q_{\text{ohm}}^{-1}$ . In Eq. (9),  $\Delta = 2Q_e(\omega - \omega_0)/\omega_0$  and in Eq. (10)  $V$  is the resonator volume. At the same time, in the presence of the beam when the microwave power extracted from the beam is much larger than  $P_{\text{cav}}$ , the output power flow is equal to

$$P_{\text{out}} = \frac{\omega}{Q_e} F^2 V. \quad (11)$$

In Eqs. (10) and (11) we are not concerned with the normalization constant for  $A$  and  $F$  since they are the same for both, and we are interested only in the ratio of these values. As follows from Eqs. (9)–(11), this ratio is equal to

$$\frac{A}{F} = 2 \sqrt{\frac{P_{\text{in}}/P_{\text{out}}}{(1 + Q_e/Q_{\text{ohm}})^2 + \Delta^2}} \quad (12)$$

In our experiment, the condition  $\Delta^2 \ll 1$  is well satisfied so that Eq. (12) reduces to

$$\frac{A}{F} = \frac{2}{1 + Q_e/Q_{\text{ohm}}} \sqrt{P_{\text{in}}/P_{\text{out}}}. \quad (13)$$

Substituting the field amplitude ratio given by Eq. (13) into Eq. (7) gives the following equation for the phase-locking bandwidth

$$\frac{\omega_{\max} - \omega_{\min}}{\omega_0} \cong \frac{2}{Q(1 + Q_e/Q_{\text{ohm}})} \sqrt{P_{\text{in}}/P_{\text{out}}}. \quad (14)$$

For the case of a critically coupled cavity (i.e.,  $Q_e = Q_{\text{ohm}}$ ) with no power reflection at the cavity entrance, Eq. (14) becomes

$$\frac{\omega_{\max} - \omega_{\min}}{\omega_0} \simeq \frac{1}{Q} \sqrt{P_{\text{in}}/P_{\text{out}}}. \quad (15)$$

Equation (15) is another common form of Adler's equation; however, it is not applicable to the present case since the gyrotron cavity is overcoupled ( $Q_e < Q_{ohm}$ ). Then, one must use the more general form in Eq. (14), which can be rewritten

$$\frac{\omega_{\max} - \omega_{\min}}{\omega_0} \cong \frac{2}{Q_e} \sqrt{P_{in}/P_{out}}. \quad (16)$$

Equation (16) may be regarded as a generalization of Adler's equation which allows for power reflection at the entrance to the cavity.

### B. Expected Pulse Waveforms

In the experiment, the lock range can be determined by sweeping the synthesizer frequency across the normal operating frequency of the gyrotron and viewing the phase difference between the gyrotron output and the injected signal over a single pulse as well as on a pulse-to-pulse basis.

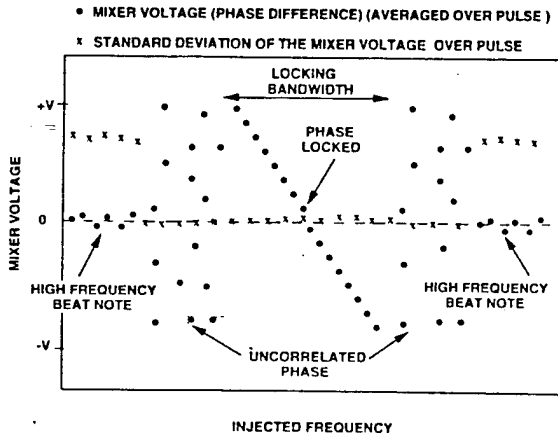


Fig. 6. Expected phase vs. injected frequency over three regions: 1) high frequency beat note, 2) uncorrelated phase difference, 3) phase-locked for the specific case where the  $180^\circ$  range of phase difference is from  $0^\circ$  to  $180^\circ$ .

The average value of the phase difference between the reference and test signals over a given pulse is estimated by computing the average of a set of samples taken from the center portion of the difference pulse. When the difference frequency is large, many cycles appear across the pulse and the average voltage is zero. When the two input frequencies to the mixer are close enough so that no significant portion of a cycle appears across the pulse, a finite average mixer voltage is found for that particular pulse. If the injection signal is so close to the gyrotron frequency that the difference is not resolvable over the pulse length, but the gyrotron is not phase-locked with the injection signal we would expect uncorrelated phase (average pulse voltage) from pulse to pulse. When the gyrotron is injection locked we expect the phase to ramp through a  $180^\circ$  degree range as the locking bandwidth is traversed (see the next section). An example of average voltage results over three regions (high frequency beat note, uncorrelated phase difference, and phase-locked) are shown in Fig. 6. In addition to the

average phase of the pulse, the standard deviation of the mixer voltage (pulse phase) is also included on the plot. This statistic is also an aid in determining the lock range. When many cycles appear across the pulse the standard deviation is high; it is low under locked conditions regardless of the phase of the pulse.

### C. Demands on Gyrotron Beam Voltage

In real systems, there are always voltage fluctuations which change the hot cavity resonant frequency,  $\omega_0$ . For phase-locking to occur, frequency changes caused by the voltage fluctuations, which we denote  $\Delta\omega_v$ , must be smaller than the locking bandwidth,  $\Delta\omega_L$ . Combining this condition with Eq. (16) yields

$$\Delta\omega_v < \frac{2\omega_0}{Q_e} \sqrt{\frac{P_{in}}{P_{out}}}. \quad (17a)$$

Writing  $\Delta\omega_v = \Delta V_b d\omega_0/dV_b$ , where  $\Delta V_b$  is the voltage fluctuation, we have

$$\frac{\Delta V_b}{V_b} < \sqrt{\frac{P_{in}}{P_{out}}} \frac{2\omega_0}{V_b Q_e (d\omega_0/dV_b)}. \quad (17b)$$

In this equation,  $\Delta V_b/V_b$  is to be interpreted as the allowed relative voltage fluctuation in the modulator. Thus, if  $V_b d\omega_0/dV_b$  is too large, it will be impossible to construct a voltage modulator with small enough fluctuations to satisfy Eq. (17). We reproduce here the calculated results which appeared in reference [10] and which are shown in Fig. 7. Allowed maximum values of  $\Delta V_b/V_b$  are plotted versus voltage for various values of the detuning parameter  $\delta$  which is given by

$$\delta = \frac{\omega T_p}{2} \left( 1 - \frac{s\Omega_{c0}}{\omega} \right) \quad (18)$$

where  $\Omega_{c0}$  is the initial relativistic cyclotron frequency.

In these figures, the assumption was made that  $P_{in}/P_{out} = 10^{-3}$  and that  $Q_e = 1000$ . The value of  $Q_e$  and the range of  $V_b$  do not match those in the present experiment, but the trend of the predictions are believed to be relevant. Gyrotron efficiency is also included on the plots. In the region where the efficiency is below approximately 20%, the requirement on the modulator voltage fluctuations are quite stringent: on the order of 0.1%. On the other hand, for gyrotron efficiency  $\gtrsim 30\%$ , the allowed voltage fluctuations are typically on the order of 1%.



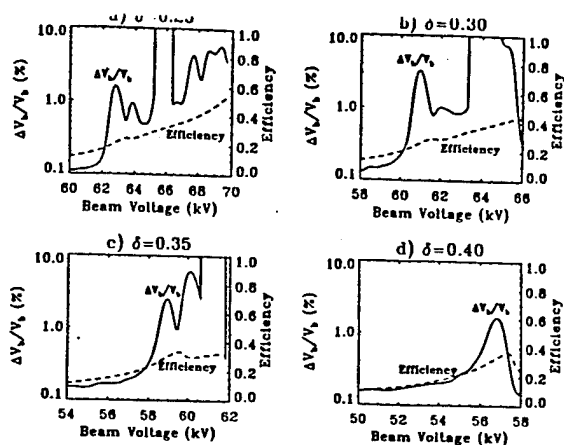


Fig. 7. Allowed voltage fluctuation for phase-locking.

#### IV. EXPERIMENTAL RESULTS

##### A. Measurement of Locking Bandwidth

In all, sixteen separate experiments were performed. Two were control experiments with the injection horn blocked, eight were performed at full injection power (60 Watts), and two were performed at each of three reduced power levels, (30, 15, and 6 Watts). For each experiment 250 pulses were captured near the center of the lock range for later analysis. The synthesizer was swept across a 10 MHz range in 60 seconds, and the pulse repetition frequency was 43 Hz, corresponding to a frequency step of 3.876 kHz per pulse. The pulse waveforms were sampled at a rate of 10 samples per microsecond, and the effective pulse width was 4 microseconds. In some instances the 250 pulses did not straddle the complete locking bandwidth and no useful results were obtained from those experiments.

Figure 8 plots the average mixer voltage (proportional to the sine of the phase), using a solid line to connect each of the 250 points in a control experiment where the injection horn was blocked. As expected, near the beginning and near the end of the data the difference frequency is large enough to produce at least one complete cycle across the pulse and zero average voltage is obtained. Between pulse 50 and 100 the difference frequency is small, and only the random pulse-to-pulse phase jitter of the gyrotron is seen. No pulse-to-pulse correlation is observed and the average voltage fluctuates wildly across the entire allowable mixer range of 0.35 to -0.25 volts. Note the fact that these two voltage extremes are not symmetric, indicating a non-ideal mixer with some finite offset voltage. This plot is exactly what one would expect for the control experiment with no injection power. The standard deviation of the voltage samples on each pulse is plotted as a dashed curve in Fig. 8.

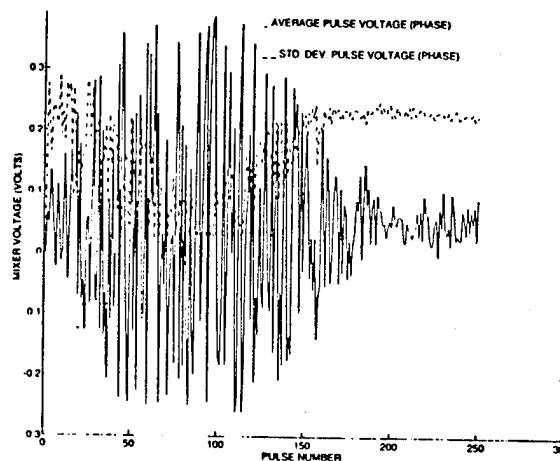


Fig. 8. Mean and standard deviation of samples (no locking).

Figure 9 plots the same information for the case when the termination is removed and 60 Watts are injected into the gyrotron. Now a constant phase progression covering the full mixer range (180 degrees) is seen from pulse number 50 to 164. This 114 pulse interval then represents the locking bandwidth, which in this case corresponds to 440 kHz. It can also be observed that at the high end of the lock range, near pulse number 160, there is a region where intermittent locking occurs. Shot-to-shot modulator pulse height fluctuations cause shifts in the gyrotron output frequency sufficient to randomly unlock the system. This can be attributed to the limited pulse-to-pulse stability as well as the long term drift of the gyrotron frequency. Including the intermittent region, locking occurs over a bandwidth of 510 kHz.

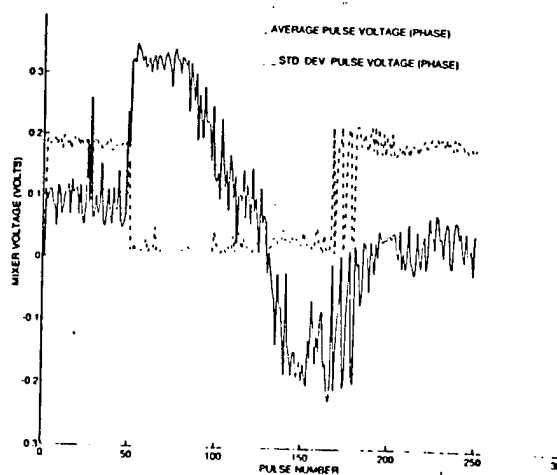


Fig. 9. Mean and standard deviation of samples (locked 114 pulses - 440 kHz).

Examination of the individual pulses in the locking range shows that the behavior predicted in Fig. 6 is observed.

Figure 10 plots the mixer voltage for four representative pulses captured during the experiment discussed above. As can be seen from Fig. 10, pulse number 3 is unlocked and more than a complete cycle of beat note is visible across the pulse. Pulses numbered 75, 120, and 140 represent locked pulses. They are relatively flat, with an average voltage that is proportional to the phase difference between the injection and output signals. This voltage varies from a maximum (pulse 75) through zero (near pulse 120) to a minimum (pulse 140) as the lock range is traversed.

In all, twelve of the experiments produced useful results. These data are tabulated below in Table 3 along with theoretical predictions from Eq. (16) with gyrotron output power  $P_{out} = 100$  kW, and the gyrotron operating frequency  $f_0 = 34.5$  GHz, and taking  $Q_e = 2500$ . There is rough agreement between the experimental values of locking bandwidth and the theoretical predictions. At the highest values of the injection power, the measured bandwidth is somewhat smaller than the theoretical value; this may be due to the ripple in the gyrotron modulator voltage. We also note that as injection power,  $P_i$ , is reduced the locking bandwidth appears to shrink less rapidly than  $\sqrt{P_i}$ ; however, further study is required before a definitive statement can be made.

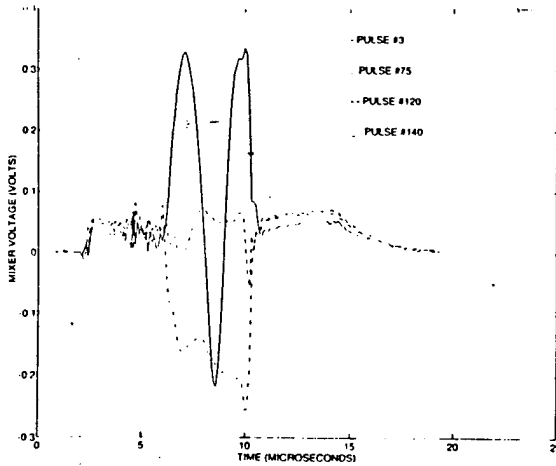


Fig. 10. Mixer voltage for four representative pulses captured during the experiment.

Table 3. Results of phase-locking measurement.

$P_{in}$ (Watts)	Avg. # Pulses Locked	Bandwidth (kHz)	Theoretical Bandwidth (kHz) using Eq. (17)	Gain (dB)
0	0	0	0	0
6	68	230-310	220	42
15	79	310-330	348	38
30	90	340-390	490	35
60	106	440-510	693	32

### B. Effect of Beam Voltage on Gyrotron Operation

The phase-locking experiment was performed with a gyrotron operating efficiency of 30% and with a beam voltage ripple of 0.3%. These conditions are compatible with theoretical estimates for the realization of phase-locking as suggested by Fig. 7. In fact, the pulse width of the beam voltage was 7 microseconds, but the duration of the microwave signal over which phase-locking could be realized was 4 microseconds. This 4 microsecond interval corresponds to the flat portion of the beam voltage where  $\Delta V_b/V_b < 0.3\%$ .

## V. DISCUSSION OF RESULTS

The present experiment demonstrated phase-locking of a second-harmonic, 100 kW, millimeter-wave gyrotron oscillator. Locking bandwidth was measured by means of an instantaneously recording and computer processing system. The results demonstrate for the first time phase-locking of a harmonic gyrotron oscillator ( $s > 1$ ); the phase-locking was accomplished by separating the paths of the injection signal and the output signal in a low loss, high power compatible, quasi-optical circulator. The insights gained during this study may be summarized as follows:

- A second-harmonic gyrotron oscillator incorporating a special complex cavity can operate with sufficient stability and efficiency that it can be phase-locked by injecting an external signal as small as 42 dB below the gyrotron output power.
- A quasi-optical circulator can be of practical value in phase-locking high power millimeter-wave oscillators with signal injection through the output window.
- The requirement for gyrotron power supply stability to achieve phase-locking is quite demanding but can be realized if gyrotron efficiency is high (i.e.,  $\Delta V_b/V_b \lesssim 0.3\%$  is required if efficiency is  $\gtrsim 30\%$ ).
- Measured values of locking bandwidth roughly agree with the predictions of a generalized Adler's equation. The measured values of locking bandwidth for a given value of the ratio,  $P_{in}/P_{out}$ , were much smaller in the present study than in a previous study of a gyrotron operating at the fundamental of the electron cyclotron frequency [5]; the difference is expected, and is attributable to the longer cavity length and correspondingly larger value of  $Q_e$  in the gyrotron of the present study.

## ACKNOWLEDGEMENTS

The authors are indebted to D. Wu, Y. Miao, J. Pyle, and D. Cohen for their technical assistance.

## REFERENCES

- R.K. Parker and R.H. Abrams, "Radio-frequency vacuum electronics: Resurgent technology for tomorrow," SPIE vol. 791, *Millimeter Wave Technology IV and Radio Frequency Power Sources*, pp. 2-12, 1987.

**Design of a High Efficiency, Low Voltage, Axially Modulated, Cusp-Injected,  
Second Harmonic, X-Band Gyrotron Amplifier**

W. Lawson, A. Grigoropolous, A. Liu, G. P. Saraph, J. Rodgers, and W. W. Destler  
Electrical Engineering Department and Institute for Plasma Research  
University of Maryland, College Park, MD 20742

Abstract

We present the theoretical design of a second harmonic small-orbit gyrotron amplifier which utilizes the interaction between a 35 kV, 4 A beam and a  $TE_{011}$  cavity to produce over 70 kW of amplified power at 9.9 GHz in a 1.83 kG magnetic field. One of the novel features of this device is that the electron gun produces an axially-streaming annular beam which is velocity modulated by a short  $TM_{0n0}$  input cavity. Perpendicular energy is imparted to the beam via a non-adiabatic magnetic transition at the end of a 13 cm drift region. An efficiency of 53% is predicted with a large signal gain near 20 dB by a single particle code which takes into account non-ideal effects associated with finite beam thickness and finite magnetic field transition widths. A description of the operating principles and details of the modeling techniques for this device are given before the tube performance is characterized.

## I. INTRODUCTION

In recent years, numerous theoretical and experimental investigations of gyrotrons operating near the fundamental cyclotron frequency have proven them to be reliable, efficient, high power sources of microwave and millimeter wave radiation.<sup>1-4</sup> These studies have been performed over a wide range of parameters and have resulted in a wealth of information about the electron gun requirements and characteristics and about the stability, efficiency, and mode competition properties of microwave circuits for gyrotrons.<sup>5-9</sup> Potential applications of these sources include RF drivers for accelerators, plasma heating in magnetic fusion research, millimeter wave and deep space radar, materials processing, and nonlinear spectroscopy of semiconductors and biological materials.

Unfortunately, conventional gyrotrons operating near the fundamental cyclotron frequency (first harmonic gyrotrons) must be immersed in a magnetic field whose strength is linearly proportional to the output frequency. Thus, they are not viable candidates for some high frequency applications that require compact and lightweight tubes. Two potential ways to decrease the applied magnetic field and the accompanying material bulk and power consumption are (1) to use Doppler upshifting via operation at a high axial wavenumber and (2) to operate at a harmonic of the cyclotron frequency. The cyclotron auto-resonance maser (CARM) is an example of a device that takes the first approach. Many CARMs have been built and tested but none have come close to the efficiencies achieved in first harmonic gyrotrons.<sup>10-12</sup> Mode competition from gyrotron instabilities and sensitivity to velocity spread have typically been the limiting factors. Low harmonic operation (typically the second or third harmonic) has met with some success in the conventional small-orbit gyrotron configuration<sup>13,14</sup> and high-harmonic devices have been fairly successful in the large-orbit configuration.<sup>15-33</sup> Still, the efficiencies of second harmonic devices usually lag behind their first harmonic counterparts by several percent and efficiencies tend to decrease fairly rapidly with increasing harmonic number after that point.

We have recently proposed<sup>34</sup> a method of pre-bunching the electron beam to enhance the efficiency in high harmonic, large-orbit devices which is based on the cusp-injection scheme.<sup>35</sup> Before the annular beam passes through the balanced, non-adiabatic magnetic field reversal, it first encounters a circularly polarized  $TM_{mn0}$  mode input cavity and a subsequent drift region. The resultant ballistic bunching (potentially) sets up a beam that can efficiently interact at the  $m$ th harmonic with a simple right-circular output cavity. For example, the design study in Ref. 34 demonstrated that an efficiency of 40% was achievable in X-Band at the fourth harmonic via an interaction between a 100 kV, 25A electron beam and a  $TE_{411}$  cavity.

While this initial result is quite promising, there are some practical limits to the applicable range of parameters for this device. For example, the beam radius of the large-orbit configuration is equal to the Larmor radius, which is proportional to the perpendicular velocity for a given cyclotron frequency. Thus, the beam radius in low voltage systems decreases fairly substantially with decreasing beam energy. However, the relative radius of the maximum electric field in a cavity increases with increasing harmonic number. In fact, the electric field at radii much less than the maximum field radius varies by a factor that is proportional to the power of the harmonic number. In such systems, the achievement of the necessary field strength for efficient interaction often leads to unrealistic requirements on output cavity quality factors.

There are at least two possible ways to overcome these difficulties and design efficient, low voltage, harmonic devices. One way is to use a vane-resonator to couple various azimuthal modes together. The resultant cavity modes can support the necessary azimuthal field variation with a much lower cutoff frequency. Thus, the wall radius can be reduced considerably as compared to the smooth wall case and the interaction impedance can be significantly increased. There are some potential drawbacks to this approach. For example, the mode composition of the output signal in an axially-coupled vane resonator cavity can be significantly more complicated than for the smooth wall case. Still, this approach has been used with reasonable success in many conventional large-orbit gyrotrons.<sup>19,22,24,33</sup> The design of an axially-bunched, low voltage large-orbit gyrotron with a vane resonator will be the subject of a later study.

The approach we will investigate in this work is to pre-bunch a small-orbit beam. Axial modulation is still a viable concept because a small orbit beam can be generated by a non-adiabatic magnetic transition that does not reverse the direction of the field.<sup>36</sup> The guiding center radius can be adjusted to place the beam at a location where the electric field is relatively strong. This non-zero guiding center radius expands the number of potential modes that the beam can interact with. While this may enable us to select a desirable output mode it also can potentially lead to additional mode competition problems. A properly pre-bunched beam, however, should help to reduce mode competition by preferentially selecting the desired operating mode.

We will illustrate this approach via the presentation of a second harmonic small-orbit system design. In this design, a 35 kV, 4 A beam is pre-bunched by a  $TM_{020}$  cavity and interacts with a  $TE_{011}$  cavity to theoretically produce over 70 kW of power with an efficiency and large-signal gain of approximately 53% and 20 dB, respectively. In Section II, we discuss the basic amplifier configuration and describe the computer codes used in the analysis. In Section III, we detail the results of the design example and present tube stability and large-signal characteristics. We also characterize the sensitivity of the device to parameter variations. The results of this study are summarized in the final section.

## II. THEORETICAL MODEL

A simplified schematic of an axially-modulated, cusp-injected, small-orbit gyrotron amplifier is given in Fig. 1a. A linearly-streaming, thin, mono-energetic, annular beam is immersed in a uniform axial magnetic field and injected into a short buncher cavity. The axial electric field of the input cavity (Fig. 1c) modulates the energy of the electron beam which results in ballistic bunching as the electrons drift through the region immediately following the cavity. When the electrons encounter the non-adiabatic magnetic field transition (shown in Fig. 1b), the radial magnetic field produces a Lorentz force which converts part of each electron's energy into perpendicular motion. Because this conversion occurs in a short distance, the electron bunches that form begin to rotate with the particles. These bunches then interact with the electric field in the output cavity (Fig. 1c) and, if properly formed, can give up most of their energy to the electromagnetic wave.

In order for the bunches to interact effectively with the output cavity fields, the resonant frequencies of the input and output cavities must be nearly integer multiples of the cyclotron frequency (in the output cavity). Furthermore, if  $s_1$  and  $s_2$  are the multiples (harmonics) of the cyclotron frequency in the input and output cavities, respectively, and  $m_1$  and  $m_2$  are the azimuthal mode indices of the same two cavities, respectively, then the following condition must be satisfied:

$$m_1 / s_1 = m_2 / s_2. \quad (1)$$

The designs in this work utilize operating modes with  $m_1 = m_2 = 0$ , so that any combination of  $s_1$  and  $s_2$  are acceptable. We will always focus on the  $s_2 = 2$  case. Most of the analysis will be performed with  $s_1 = 2$  as well, but we will demonstrate towards the end that an  $s_1 = 1$  design is nearly as effective as the earlier design and has several nice features that warrant consideration.

Because the input cavity operates in the  $TM_{0n0}$  mode, it can be excited either by a single aperture on the radial wall fed by a standard waveguide or by a single loop fed by a simple coaxial line. The required drift tube length  $d$  depends on the magnitude of the energy spread ( $\Delta E/E_0$ ) imparted to the beam and has been derived elsewhere for a low voltage system as:<sup>34</sup>

$$d = \beta_o \lambda / (2 \Delta E/E_o) \quad (2)$$

where  $\beta_o$  is the streaming velocity (normalized to the speed of light) and  $\lambda$  is the RF wavelength (of the input cavity signal).

The magnetic transition at the end of the drift region is shortened by a thin iron pole piece. Long solenoids on either side of the pole piece generate approximately constant axial magnetic fields in each region ( $B_c$  on the input side and  $B_o$  on the output side). The required mismatch between the magnetic field strengths depends on the beam radius and the desired velocity ratio ( $\alpha = v_{\perp}/v_z$ ). If the original beam radius is  $r_o$  and the Larmor radius after the magnetic transition is  $r_L$ , then the ratio for an ideal (zero length) transition is:<sup>36</sup>

$$B_c / B_o = 1 - 2 r_L / r_o. \quad (3)$$

The beam's energy spread results in velocity spreads after the magnetic transition which can be approximated by:<sup>34</sup>

$$\begin{aligned} \frac{\Delta v_z}{v_{z_o}} &= \frac{1}{2} \left[ 1 + \alpha^2 + \alpha^2 (\gamma_o^2 - 1) \right] \frac{\Delta E}{E_o} \\ \frac{\Delta v_{\perp}}{v_{\perp_o}} &= -\frac{1}{2} (\gamma_o^2 - 1) \frac{\Delta E}{E_o} \end{aligned} \quad (4)$$

when the effects of the input cavity's magnetic fields are neglected. In Eq. (4),  $\gamma_o$  is the relativistic mass factor. For low voltage beams, the induced perpendicular velocity spread is typically small but the parallel spread can become quite large. Setting an upper limit on this value often dictates the drift tube length in small-orbit designs via Eq. (2).

There are two other contributions to the net velocity spreads. The first is from the electron gun optics and hence is design specific, can typically be kept fairly small, and won't be discussed further. The other contribution comes from the canonical angular momentum of finite thickness beams. This spread can be reduced in small-orbit systems by compressing the beam width.<sup>36</sup>

The output cavity for the pre-bunched small orbit gyrotron is a simple axially-coupled right-circular waveguide that is designed to operate at the proper frequency in the  $TE_{011}$  mode. The



cavity has a long main section and a shorter output lip that has a radius smaller than that required for the operating mode to propagate. The resonant frequency and quality factor ( $Q$ ) are calculated with a scattering-matrix code.<sup>37,38</sup> In general, the required cavity  $Q$  is far below the resistive  $Q$  of a copper cavity but sufficiently large so that the interaction between the beam and the microwaves occurs predominantly in the main section of the cavity. For this reason, the sinusoidal axial field dependence of a closed cavity is often a good approximation for the open-ended cavity.

Four main computer codes are utilized in the design process. The scattering matrix code is used to design the output cavity and a start-oscillation code<sup>39</sup> is used to check the stability of the output cavity to spurious modes in the absence of beam pre-bunching by the input cavity. This code assumes that the magnetic field is constant in the output cavity.

The other two codes are single particle codes that numerically integrate the particle motion in the device. The first single particle code simulates the beam's motion through the input cavity, the drift region, and the non-adiabatic magnetic transition. Given the beam parameters, electrons are initially "launched" over a range of axial positions, times, and angles that represent the entirety of phase space (after taking into account any symmetries in the system). The initial velocities of the particles are assumed to be purely axial, but electrons can be started from several radial locations to emulate finite thickness beams. The EM fields are assumed to be confined to the input cavity (leakage fields are neglected). The only field in the drift region is the axial magnetic field, which is assumed to remain constant. The magnetic transition region is simulated with a piece-wise linear axial field profile. The Runge-Kutta method is used to start the process and a predictor-corrector scheme is used for the bulk of the numerical integration. Numerical convergence is checked by varying integration step size and the number of particles. Conservation of energy and canonical angular momentum are also checked in regions where there is only a static magnetic field. This code produces the phase space distributions of the electrons at the end of the transition region and calculates various quantities that give the average beam statistics and indicate the effectiveness of the bunching process. The resistive  $Q$  of a copper input cavity

and the required drive power are also reported. This code is typically iterated, while adjusting the drift region length and the strength of the input field, until satisfactory bunching performance is achieved.

The second code takes the results from the first single particle code and uses the same numerical techniques to calculate the extraction efficiency of the EM wave in the output cavity under steady-state conditions. The code can model either a closed circular cavity or it can accept the output from the scattering matrix code to model open resonator configurations. The magnetic field in the output cavity can be tapered linearly to optimize the interaction. This code is typically iterated, while varying the cavity and magnetic field parameters, until an optimal design is achieved. During each efficiency run, the amplitude and phase of the EM wave are adjusted until maximum efficiency is calculated. In addition to the efficiency, the code reports the required diffractive  $Q$  and the resistive  $Q$  for a closed, right-circular copper cavity. By decreasing the field amplitude in the output cavity toward zero, this code can also be used to calculate the start currents for the various modes in tapered magnetic fields, whether the beam is pre-bunched or unbunched.

We have also run a separate large signal code to independently verify the efficiency calculations in the output cavity. This code, originally designed for relativistic gyrokystrons<sup>39</sup>, is modified to take into account the pre-bunched beam at the entrance of the output cavity from the first single particle code. The code also assumes the cold cavity field profiles and  $Q$  value from the scattering matrix code which includes linear mode conversion at the radial steps in the output cavity. In order to optimize the device efficiency, a two-dimensional search, in terms of overall mode amplitude and phase, is carried out. To ensure self-consistency in the calculations the quality factor required to maintain the steady-state field amplitude is matched with the  $Q$  value from the scattering matrix code.

Details of the results from these simulation codes for the specific designs are given in the following section.

### III. DESIGN SIMULATION

The parameters for the second harmonic design are given in Table 1.1. The system is designed to produce microwaves at 9.9 GHz via the interaction between a 35 kV, 4 A beam and the microwave circuit. The initial beam radius of 1.5 cm is selected to optimize the interaction with the EM wave in the output cavity while avoiding any beam interception. This beam can be generated with a standard electrode configuration.<sup>34</sup> If a magnetic compression of four were to be utilized, for example, the cathode thickness would be 2 mm, the average emitter radius would be 3 cm, and the required current density would be quite modest at a little over  $1 \text{ A/cm}^2$ . The table indicates the pre- and post-compression beam dimensions. The DC space charge depression in the output cavity is less than 3 % and is considerably smaller before the magnetic transition. The radial thickness corresponds to an ideal post-cusp velocity spread of  $\Delta v_{\perp} = 1.9 \%$  (if beam width compression is not utilized to reduce this number). The average velocity ratio is somewhat larger than a typical small-orbit system but is below what is often quoted for cusp-injected large-orbit systems.

The drive cavity is a simple right-circular  $\text{TM}_{020}$  cavity with the dimensions indicated in the table. The cavity width is selected to give a beam coupling factor<sup>40</sup> of about 0.93. The cavity radius is adjusted to achieve the desired operating frequency. Note that the quality factor quoted includes only the losses in the copper. The actual quality factor, after taking into account the input power coupling, should be about one-half of this value. All drive powers quoted in this paper assume a net input  $Q$  of 1400. Any beam loading is neglected. The beam is located between the first null and the second peak of the axial electric field. The required input power could be decreased and the resultant gain increased if the beam could be re-positioned on the maximum. The easiest way to accomplish this would undoubtedly be to use a coaxial input cavity. Other possibilities include the introduction of dielectrics into the input cavity or moving the input cavity into the magnetic compression region where the beam radius is larger.

The peak axial magnetic field in the output cavity is determined from the optimization procedure and is such that twice the cyclotron frequency is about 3% lower than the drive frequency.

The magnetic field in the input region is about 60 Gauss less than predicted by Eq. (3) due to the finite cusp width. The distance between the input cavity and cusp transition is optimized with the numerical codes, but the initial length is chosen from Eqs. (2) and (4) so that maximal bunching could be achieved with an energy spread and an induced axial velocity spread approximately under 3% and 10%, respectively. The transition width should readily be achievable with the aid of one or more iron pole pieces. The optimal magnetic field profile is shown in Fig. 1b.

The length of the output cavity is varied to maximize efficiency while keeping the required  $Q$  less than 5-7% of the resistive  $Q$  of a copper cavity. This restriction means that over 93% of the microwave power can be extracted. The cavity radius and lip dimensions are adjusted to produce the required resonant frequency and  $Q$  while avoiding beam interception (by the particles that are accelerated during the interaction). The main cavity length is such that particles undergo approximately eleven revolutions inside this region. The azimuthal electric field at the beam radius in the output cavity is shown in Fig. 1c. The exponential decay in the drift region and the leakage field through the coupling aperture can be seen in the figure.

A second constraint on the output cavity is that it be stable to spurious oscillations. The beam current required to achieve self-oscillation in the output cavity is shown in Fig. 2 as a function of (uniform) magnetic field. It is assumed that no drive power is applied to the input cavity. Curves are plotted for the  $TE_{011}$  mode and the  $TE_{111}$  mode. The resonant frequency of the fundamental  $TE_{111}$  mode is near the cyclotron frequency at 4.87 GHz. The quality factor of the  $TE_{111}$  mode is 72. All other modes evaluated are completely stable to currents below 10 A in the magnetic field range indicated. The cavity is expected to be unstable to the operating mode but stable to the fundamental mode at the design field of 1.83 kG. However, the optimal taper yields a field at the exit of the output cavity of 1.775 kG. At this field magnitude the fundamental mode is unstable and the operating mode is stable. By using the efficiency code, it can be shown that with the tapered field profile the desired mode is again unstable and the  $TE_{111}$  mode is stable.

The evolution of electron bunching in the device is illustrated in Fig. 3, where the distribution of representative particles relative to the phase of the output cavity's electric field is plotted

at various axial locations. Figure 3a represents the distribution just prior to the output cavity when no drive power is applied and illustrates the initially uniform distribution of particles in phase space. The three distinct bands of particles represent the effect of finite beam thickness and the velocity spread that results from canonical angular momentum. Figure 3b shows the distribution at the output cavity entrance when a signal of 800 W is injected into the input cavity. The increase in perpendicular velocity spread can be seen clearly and is comparable (but less than) the canonical angular momentum spread. The phase distribution at the exit of the output cavity which corresponds to the 800 W input case is shown in Fig 3c. The phase coherence of the beam is essentially destroyed and a large number of particles have given up over 80% of their perpendicular energy. A much smaller number of particles have remained at about the same energy level or had their energy increase slightly. The beam evolution throughout the cavity is indicated in Fig. 1a where the r-z projection of representative particles are plotted. The figure reveals that while some particles gain energy and increase their Larmor radii, the majority of the particles lose a significant amount of energy.

The simulated results for the parameters in Table I near the optimal drive power are summarized in Table II. The nominal electric field at the beam is about 8 kV/cm in the input cavity and about 5 times that in the output cavity. The peak electric field at the wall is 17 kV/cm in the input cavity and zero in the output cavity. The total axial velocity spread includes a contribution of about 8.5% from energy spread, which is reasonably close to the estimate given in Eq. (4). The contribution to the perpendicular velocity spread from the energy spread is about 0.8%. The nominal saturated gain is about 20 dB. The peak efficiency of 53% greatly exceeds the performance of any second harmonic small-orbit amplifier to date.

The dependence of efficiency on output cavity Q is revealed in Fig. 4 for a thin beam and a drive power of 800 W. The output efficiency rises dramatically from ~5% to ~48% as the quality factor is increased from 300 to 1300. After that point, the efficiency only increases slowly with Q until it reaches its maximum value of 54.4 % when  $Q=2550$ . The nominal Q of 1825 was se-

lected rather than the optimal value because its improved stability and wall loss properties come at only a small sacrifice in efficiency.

Two drive curves for parameters near the optimal configuration (and a zero thickness beam) are shown in Fig. 5. The solid line shows the peak power at the optimal electric field strength. This represents the maximum possible performance but also requires that the quality factor be varied at each point. The zero drive efficiency is over 22% and requires an output quality factor of 3180. The second curve gives the output power for the original output cavity with a Q of 1825. Performance is poor at low drive powers, where the zero input efficiency is less than 2%. However, the two curves are quite similar near the maximum output power, which occurs for the latter curve at an input power of 1.4 kW. The corresponding power and efficiency are 78 kW and 55.7% efficiency, respectively.

The dependence of output efficiency on the thin beam's average velocity ratio is given in Fig. 6. This ratio is modified solely by varying the magnetic field in the drift region. The phase and amplitude output cavity's electric field are optimized at each point. This again implies that the quality factor is adjusted to maximize output power. All other parameters, however, are held at their nominal values. The efficiency drops off fairly rapidly with decreasing velocity ratio, going to a level of about 23% at a velocity ratio near one. This result requires a quality factor of 8570. Efficiency only slowly increases in the opposite direction, approaching a level of 57% with a velocity ratio of three and a quality factor of 1635. This result would undoubtedly degrade with the introduction of finite beam thickness. On the other hand, performance could possibly be improved further if additional optimizations (e.g. cavity length adjustment) were performed.

The effect of beam thickness on efficiency at the nominal operating point has been examined in Fig. 7. The efficiency is fairly insensitive to beam thickness and the resulting velocity spread. For example, efficiency barely dips below 50% at a beam thickness of 0.26 cm and an axial velocity spread near 25%. Particles begin to hit the output cavity wall when the thickness exceeds 0.28 cm.

The results from the single particle code are confirmed using the gyrokystron code. In these simulations, the pre-bunched beam shown in Fig. 3(b) and field profiles from the scattering matrix code are used as the input. The effect of magnetic field taper is presented in Fig. 8a. The field amplitude and phase are adjusted at each value of magnetic taper to optimize the efficiency. The beam current is adjusted such that the required quality factor from the large signal code matches with the  $Q$  value from the scattering matrix code. It is important to note that the product of the beam current and  $Q$  is proportional to the square of field amplitude and inversely proportional to the efficiency. If the beam current is not within the acceptable range then the amplitude and phase should be readjusted or the cavity should be redesigned with a different value of  $Q$ . The efficiency values plotted in Fig. 8a, shown by the circles, correspond to 10 % rms-spread in the axial velocity. The corresponding values of optimum beam current are shown by the triangles. It can be seen that the efficiency is maximum for the magnetic taper value of -5 G/cm which is equivalent to a -3 % taper. The beam current of 3.8 A matches well with design current of 4.0 A based on the single particle code. The magnetic taper improves the efficiency from 44.4 % at zero taper to 51.4 %. Higher magnetic tapers correspond to lower values of field amplitudes required to achieve maximum efficiency and hence lower values of optimum beam current. The optimum beam current (for a fixed value of  $Q=1825$ ) varies from 2.3 Amp to 6.1 Amp for the magnetic taper of -8 G/cm to 0 G/cm. The corresponding output power level varies from 40 kW to 95 kW.

The effect of axial velocity spread on the design point is plotted in Fig. 8b. This assumes that the beam is monoenergetic at the entrance of the output cavity. It can be seen from the figure that the output efficiency is above 50 % for axial velocity rms-spreads up to 15 %. The decrease in efficiency with the velocity spread is very slow for this device as compared to second harmonic gyrotrons or other devices. It is important to note that the velocity spread in the gyrokystron code is "placed" on the nominal beam distribution and thus is quite different from the spread computed by the two single particle codes. Nonetheless, the agreement between the two types of simulations is excellent.

The final simulation that we present utilizes an input cavity that is resonant in the  $TM_{010}$  mode at half the output frequency. This trivially satisfies the requirement in Eq. (1). The drift region length is doubled to conform to Eq. (2). The drive power is adjusted to introduce a similar energy spread into the beam. Most of the other parameters remain the same. All of the values that are adjusted are summarized in Table III; those not adjusted remain as in Table I. For a quality factor of about 2540, an electronic efficiency of 50.9 % is achieved. This represents only a slight decrease ( $\sim 2\%$ ) over the second harmonic drive case. Furthermore, the reduced input power requirement, coupled with the higher quality factor and the lower stored energy boosts the large-signal gain to over 28 dB.



#### IV. DISCUSSION

The novel concept of an axially pre-bunched, low-voltage, second-harmonic, small-orbit gyrotron presented here promises reasonable gains and unprecedented efficiencies in a compact design. Because the beam is linearly streaming throughout most of the tube, this device is easily more stable than a comparable gyrokystron. The ability to use overmoded output cavities should enable these tubes to achieve higher powers than comparable klystrons.

The specific designs investigated here utilized a 35 kV, 4 A beam to produce over 70 kW of power at 9.9 GHz via an axially coupled  $TE_{011}$  output cavity. Simulations were carried out with a single particle code which was modified to accept realistic cold-cavity field profiles from a scattering matrix code. The two-cavity gains with second ( $TM_{020}$ ) and first harmonic ( $TM_{010}$ ) input cavities were 20 dB and 28 dB, respectively. The simulated efficiency for the X-Band input cavity system of 53% included non-ideal effects due to finite beam thickness and cusp-width. The efficiency of the first harmonic input system was only about two percent lower and required an output cavity Q about 39 % higher than the previous design. The addition of one or more second-harmonic buncher cavities should allow for shorter drift regions, higher gain, and possibly higher efficiency. It should also minimize the performance discrepancies between the two input schemes.

One of the key differences between the axial bunching schemes for large- and small-orbit devices is the axial velocity spread resulting from the energy modulation. While the approximate expression for velocity spread (Eq. (4)) is the same for both cases, the effect of the input cavity's magnetic field appears to reduce the axial spread in large-orbit systems<sup>34</sup> but does little for the spread in small orbit systems. This difference stems in part from the effect of each electron's radial displacement on the post cusp velocity ratio. Fortunately, this spread can often be minimized by choosing a drift length that is proportional to the axial periodicity of the beam's radial perturbation. It is also possible that the beam focusing of the electron gun could be designed to reduce the velocity spread. Additional work must be done on this concept to determine its viability.

Another concept which requires further investigation is the operation of pre-bunched small-orbit devices above the second harmonic. Third harmonic operation was briefly simulated during this investigation with a (third-harmonic)  $TM_{020}$  input cavity and a  $TE_{021}$  output cavity, but no systematic study was undertaken. By varying the guiding center radius, we were able to fairly quickly find operating points with efficiencies exceeding 40%, however the required output cavity quality factors were comparable to the resistive Qs of copper cavities. It is possible that operation was hindered by the induced axial velocity spread, because harmonic operation is increasingly more sensitive to such spread. However, it is also possible that further optimization would have resulted in high efficiency at a realistic operating point, particularly since the magnetic field resonance is quite narrow at low voltage. In systems that can tolerate higher beam voltages, the correspondingly broader magnetic field resonances should facilitate high harmonic operation.

Because of the high quality factors of both cavities in this design, the instantaneous bandwidth of this device should be relatively small. However, we propose that this concept can readily be extended to a broad-band version. Because the beam is bunched with a  $TM_{0n}$  mode, the input cavity and drift tube region can be replaced by a helix (or some other slow wave) structure. By the same token, the output cavity can be replaced by a smooth-walled, traveling wave section. This device should realize bandwidths comparable to traveling wave tubes (TWTs), achieve higher powers and efficiencies than conventional TWTs,<sup>41</sup> and be more stable than gyro-TWTs.<sup>42</sup> The two regions will be naturally isolated from each other by the center plug of the iron pole piece (that is used to generate the non-adiabatic transition). Isolation should be further enhanced because the field patterns in each region are quite distinct.

In the future, we will attempt to investigate the theoretical questions left unanswered in the preceding few paragraphs. We also expect to work on an experimental investigation of this concept. We are in the process of building an experimental test bed which is energized by a 50 kV, 20 A, 5  $\mu$ s pulse-line modulator. We have the capability to produce magnetic fields of about 2

kG over the required distance and are currently designing an electron gun compatible with the beam parameters of this design.

This work was supported by the Tri-Services Program for Vacuum Electronics.

Table I. Second Harmonic Amplifier System Parameters

Beam Parameters		
Voltage (kV)	35	
Current (A)	4	
	(before cusp)	(after cusp)
Average radius (cm)	1.50	1.18
Beam thickness (mm)	1.00	7.33
Velocity ratio ( $v_{\perp}/v_z$ )	0.00	2.28
Input Cavity		
Drive frequency (GHz)	9.9	
Operating mode	TM <sub>020</sub>	
Resistive Quality factor (Q)	2800	
Radius (cm)	2.66	
Length (cm)	0.20	
Magnetic Field Parameters		
Buncher magnetic field (kG)	0.985	
Output magnetic field (kG)	1.83	
Cyclotron frequency (GHz)	4.794	
Cusp width (cm)	0.50	
Cavity - cusp spacing (cm)	13	
Output field taper	-3%	
Output cavity		
Output frequency (GHz)	9.9	
Operating mode	TE <sub>011</sub>	
Diffraction Q	1825	
Resistive Q	28,580	
	(main section)	(cavity lip)
Radius (cm)	1.864	1.70
Length (cm)	10.000	1.09

Table II. Second Harmonic Amplifier Performance

Input cavity results	
Input drive power (W)	800
$E_z$ at beam (kV/cm)	7.99
Drift region results	
Total $\Delta v_z$ (%)	12.2
Total $\Delta v_{\perp}$ (%)	1.8
Energy spread (%)	3.2
Output cavity results	
Power (kW)	74.2
Efficiency (%)	53.0
Gain (dB)	19.7
$E_{\phi}$ at beam (kV/cm)	39

Table III. First Harmonic Drive System Parameters

Input Cavity	
Drive frequency (GHz)	4.95
Operating mode	TM <sub>010</sub>
Resistive Quality factor (Q)	3630
Radius (cm)	2.318
Length (cm)	0.40
Input drive power (W)	110
E <sub>z</sub> at beam (kV/cm)	4.1
Drift region	
Cavity - cusp spacing (cm)	26
Total $\Delta v_z$ (%)	11.8
Total $\Delta v_{\perp}$ (%)	1.7
Energy spread (%)	3.3
Output cavity	
Diffraction Q	2540
Power (kW)	71.3
Efficiency (%)	50.9
Gain (dB)	28.1
E <sub><math>\phi</math></sub> at beam (kV/cm)	44

## REFERENCES

1. R. S. Symons and H. R. Jory, *Advances in Electronics and Electron Physics*, C. Marton, ed. (New York: Academic Press, 1981), Vol. 55, Ch. 1, p. 1.
2. V. L. Granatstein, M. E. Read, and L. R. Barnett, *Infrared and Millimeter Waves*, K. Button, ed. (New York: Academic Press, 1981), Vol. 5, Ch. 5, p. 267.
3. K. E. Kreischer, T. L. Grimm, W. C. Guss, A. W. Mobins, and R. J. Temkin, "Experimental study of a high-frequency megawatt gyrotron oscillator," *Phys. Fluids B* **2**, pp. 640-646, 1990.
4. K. Felch, C. Hess, H. Huey, E. Jongewaard, H. Jory, J. Neilson, R. Pendleton, and M. Tsirulnikov, "Recent long-pulse and high average power tests on a 140 GHz gyrotron," *Proc. SPIE* **1514**, pp. 315-317 (1990).
5. B. Levush and T. M. Antonsen, "Mode Competition and Control in High-Power Gyrotron Oscillators," *IEEE Trans. Plasma Sci.* **18**, pp. 260-272, 1990.
6. O. Dumbrajs and G. S. Nusinovich, "Cold-Cavity and Self-Consistent Approaches in the Theory of Mode Competition in Gyrotrons," *IEEE Trans. Plasma Sci.* **20**, pp. 133-138, 1992.
7. G. P. Saraph, T. M. Antonsen, B. Levush, and G. I. Lin, "Regions of Stability of High-Power Gyrotron Oscillators," *IEEE Trans. Plasma Sci.* **20**, pp. 115-125, 1992.
8. W. C. Guss, M. A. Basten, K. E. Kreischer, and R. J. Temkin, "Velocity spread measurements on a magnetron injection gun beam," *J. Appl. Phys.* **76**, pp. 3237-3243, 1994.
9. W. C. Guss, M. A. Basten, K. E. Kreischer, R. J. Temkin, T. M. Antonsen, S. Y. Cai, G. Saraph, and B. Levush, "Influence of Sideband Oscillations on Gyrotron Efficiency," *IEEE Trans. Plasma Sci.* **22**, pp. 871-877, 1994.
10. V. L. Bratman, N. S. Ginzburg, G. S. Nusinovich, M. I. Petelin, and P. S. Strelkov, "Relativistic gyrotrons and cyclotron autoresonance masers," *Int. J. Electron.*, **51**, pp. 541-567, 1981.
11. K. D. Pendergast, B. G. Danly, R. J. Temkin, and J. S. Wurtele, "Self-Consistent Simulation of Cyclotron Autoresonance Maser Amplifiers," *IEEE Trans. Plasma Sci.* **16**, pp. 122-128, 1988.
12. V. L. Bratman and G. G. Denisov, "Cyclotron autoresonance masers - recent experiments and prospects," *Int. J. Electron.*, **72**, pp. 969-981, 1992.

13. G. F. Brand, Y. Idehara, T. Tatsukawa, and I. Ogawa, "Mode competition in a high harmonic gyrotron," *Int. J. Electron.*, **72**, pp. 745-758, 1992.
14. W. Lawson, H. W. Matthews, M. K. E. Lee, J. P. Calame, J. Cheng, B. Hogan, P. E. Latham, V. L. Granatstein, and M. Reiser, "High Power Operation of a K-Band Second Harmonic Gyroklystron," *Phys. Rev. Lett.* **71**, pp. 456-459, 1993.
15. P. Sprangle, "Excitation of electromagnetic waves from a rotating annular relativistic  $e$ -beam," *J. Appl. Phys.* **47**, pp. 2935-2940, 1976.
16. W. W. Destler, D. W. Hudgings, M. J. Rhee, S. Kawasaki, and V. L. Granatstein, "Experimental study of microwave generation and suppression in a non-neutral  $e$ -layer," *J. Appl. Phys.* **48**, pp. 3291-3296, 1977.
17. H. S. Uhm and R. C. Davidson, "Intense microwave generation by the negative-mass instability," *J. Appl. Phys.* **49**, pp. 593-598, 1978.
18. W. W. Destler, H. Romero, C. D. Striffler, R. L. Weiler, and W. Namkung, "Intense microwave generation from a non-neutral rotating  $E$  layer," *J. Appl. Phys.* **52**, pp. 2740-2749, 1981.
19. W. W. Destler, R. L. Weiler, and C. D. Striffler, "High-Power microwave generation from a rotating  $E$  layer in a magnetron-type waveguide," *Appl. Phys. Lett.* **38**, pp. 570-572, 1981.
20. Y. Y. Lau and L. R. Barnett, "Theory of a low magnetic field gyrotron (gyromagnetron)," *Int. J. Infrared Millimeter Waves* **3**, pp. 619-643 (1982).
21. W. W. Destler, R. Kulkarni, C. D. Striffler, and R. L. Weiler, "Microwave generation from rotating electron beams in magnetron-type waveguides," *J. Appl. Phys.* **54**, pp. 4152-4162, 1983.
22. W. Namkung, "Observation of microwave generation from a cusptron device," *Phys. Fluids* **27**, pp. 329-330, 1984.
23. K. R. Chu and D. Dialetis, "Theory of harmonic gyrotron oscillator with slotted resonant structure," *Int. J. Infrared Millimeter Waves* **5**, pp. 37-56 (1984).
24. W. Lawson, W. W. Destler, and C. D. Striffler, "High-Power Microwave Generation from a Large-Orbit Gyrotron in Vane and Hole-and-Slot Conducting Wall Geometries," *IEEE Trans. Plasma Sci.* **PS-13**, pp. 444-453, 1985.
25. W. Lawson and C. D. Striffler, "A general linear growth rate formula for large orbit, annular electron beams," *Phys. Fluids* **28**, pp. 2868-2877, 1985.

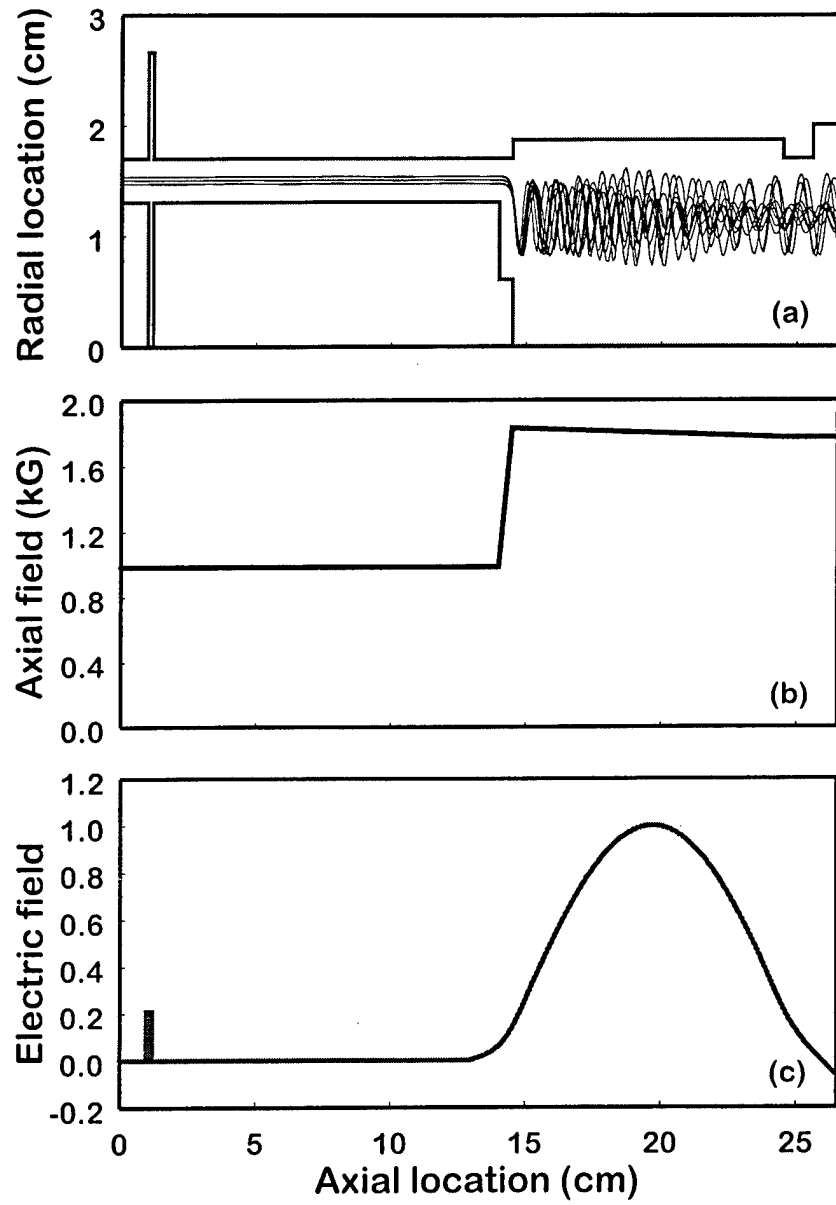


26. W. Lawson and C. D. Striffler, "A linear growth rate fluid formulation for large orbit, annular electron layers with finite thickness," *Phys. Fluids* 29, pp. 1682-1694, 1986.
27. E. Chojnacki, W. W. Destler, W. Lawson, and W. Namkung, "Studies of Microwave Radiation from a Non-Relativistic Rotating Electron Beam in a Multiresonator Magnetron Cavity," *J. Appl. Phys.* 61, pp. 1268-1275, 1987.
28. H. P. Bluem, P. E. Latham, W. Lawson, and C. D. Striffler, "Single-Particle Motion in a Large-Orbit Gyrotron," *IEEE Trans. Microwave Theory Tech.* MTT-35, pp. 946-955, 1987.
29. W. W. Destler, E. Chojnacki, R. F. Heoberling, W. Lawson, A. Singh, and C. D. Striffler, "High-Power Microwave Generation from Large-Orbit Devices," *IEEE Trans. Plasma Sci.* 16, pp. 71-89, 1988.
30. W. W. Destler, K. Irwin, W. Lawson, J. Rodgers, Z. Segalov, E. P. Scannell, and S. T. Spang, "Intense-Beam Fundamental Mode Large-Orbit Gyrotron Studies," *J. Appl. Phys.* 66, pp. 4089-4094, 1989.
31. C. S. Kou, D. B. McDermott, N. C. Luhmann, Jr., and K. R. Chu, "Prebunched High-Harmonic Gyrotron," *IEEE Trans. Plasma Sci.* 18, pp. 343-349, 1990.
32. K. Irwin, W. W. Destler, W. Lawson, J. Rodgers, E. P. Scannel, and S. T. Spang, "Second Generation, High Power, Fundamental Mode Large-Orbit Gyrotron Experiments," *J. Appl. Phys.* 69, pp. 627-631, 1991.
33. K. K. Tiong and S. P. Kuo, "Operation of a high harmonic cusptron oscillator," *Int. J. Electronics* 70, pp. 815-821, 1991.
34. W. Lawson and W. W. Destler, "The Axially Modulated, Cusp-Injected, Large-Orbit Gyrotron Amplifier," *IEEE Trans. Plasma Sci.* 22, pp. 895-901, 1994.
35. M. J. Rhee and W. W. Destler, "Relativistic electron dynamics in a cusped magnetic field," *Phys. Fluids* 17, pp. 1574-1581, 1974.
36. W. Lawson and P. E. Latham, "The Design of a Small-Orbit/Large-Orbit Gyroklystron Experiment," *J. Appl. Phys.* 61, pp. 519-528, 1987.
37. J. Neilson, P. E. Latham, M. Caplan, and W. Lawson, "Determination of the Resonant Frequencies in a Complex Cavity Using the Scattering Matrix Formulation," *IEEE Trans. Microwave Theory Tech.* 37, pp. 1165-1170, 1989.
38. W. Lawson and P. E. Latham, "The Scattering Matrix Formulation for Overmoded Coaxial Cavities," *IEEE Trans. Microwave Theory Tech.* 40, pp. 1973-1976, 1992.

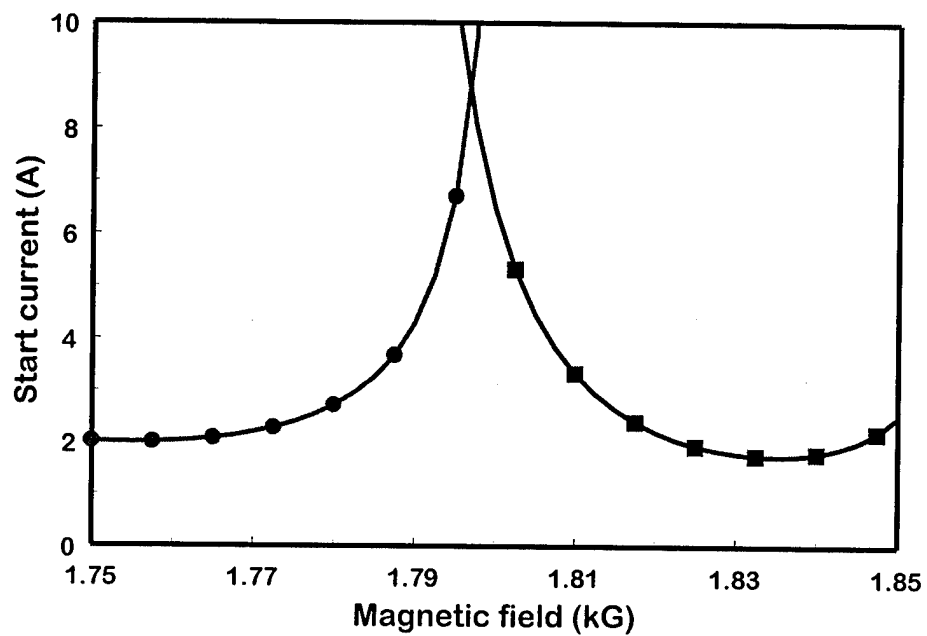
39. K. R. Chu, V. L. Granatstein, P. E. Latham, W. Lawson, and C. D. Striffler, "A 30-MW Gyrokystron-Amplifier Design for High-Energy Linear Accelerators," IEEE Trans. Plasma Sci. PS-13, pp. 424-434, 1985.
40. R. E. Collin, Foundations for Microwave Engineering, (New York: McGraw-Hill, 1966), p. 468.
41. D. Shiffler, J. A. Nation, and G. S. Kerslick, "A High-Power, Travelling Wave Tube Amplifier," IEEE Trans. Plasma Sci. 18, pp. 546-552, 1990.
42. K. R. Chu, L. R. Barnett, W. K. Lau, L. H. Chang, and H. T. Chen, "A Wide-Band Millimeter-Wave Gyrotron Travelling-Wave Amplifier Experiment," IEEE Trans. Electron Dev., 37, pp. 1557-1560, 1990.

### Figure Captions

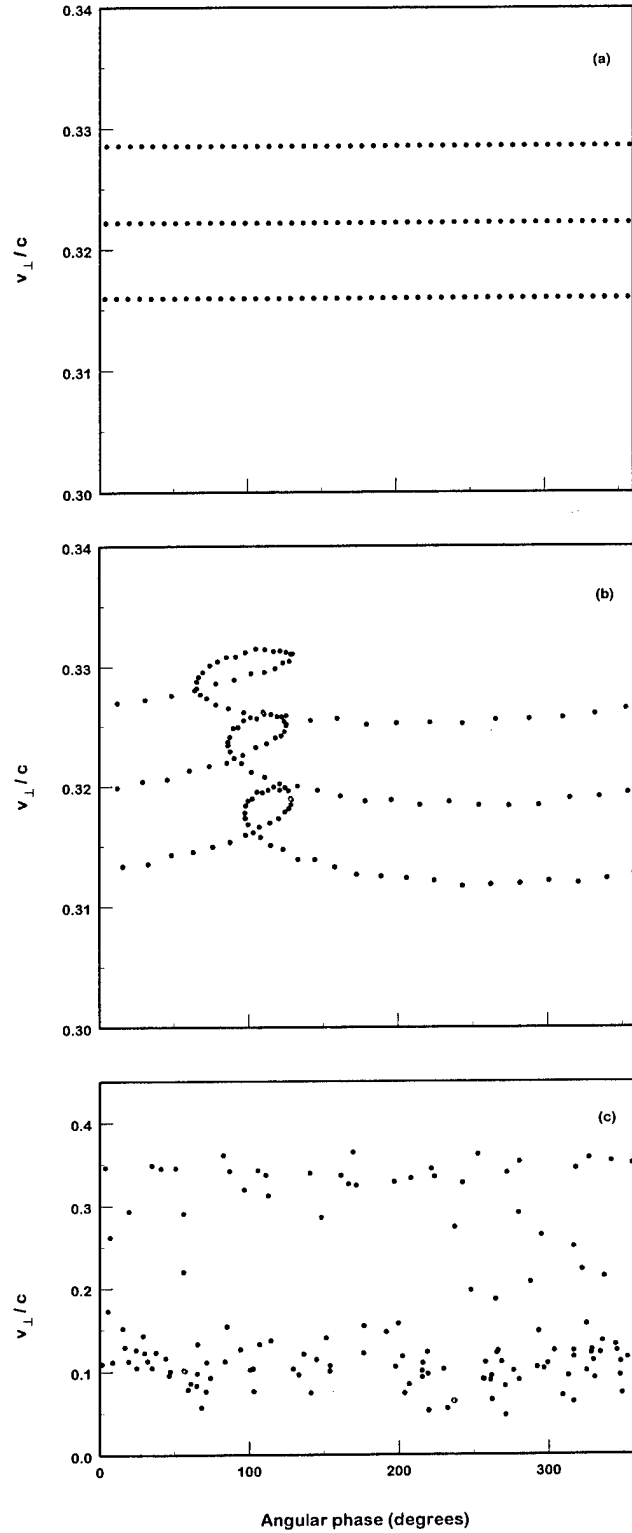
1. The axially-modulated, cusp-injected, small-orbit gyrotron: (a) system schematic, (b) axial magnetic field profile, and (c) normalized electric field profile at the beam radius ( $E_z$  in the input cavity and  $E_\phi$  in the output cavity).
2. The output cavity start-oscillation curves. The squares indicate the  $TE_{011}$  mode and the circles represent the  $TE_{111}$  mode.
3. Representative phase distribution of electrons: (a) output cavity entrance ( $P_{in}=0$  W), (b) output cavity entrance ( $P_{in}=800$  W), and (c) output cavity exit ( $P_{in}=800$  W).
4. The dependence of output efficiency on the output cavity quality factor ( $P_{in}=800$  W).
5. System drive curves. The solid line shows the output efficiency at the optimal electric field strength. The dashed line gives the output efficiency for a constant quality factor ( $Q=1825$ ).
6. The dependence of output efficiency on average velocity ratio.
7. The dependence of output efficiency on beam thickness.
8. Gyroklystron code results: (a) output efficiency (solid line) and optimal current (dashed line) as a function of magnetic field taper and (b) output efficiency as a function of velocity spread.



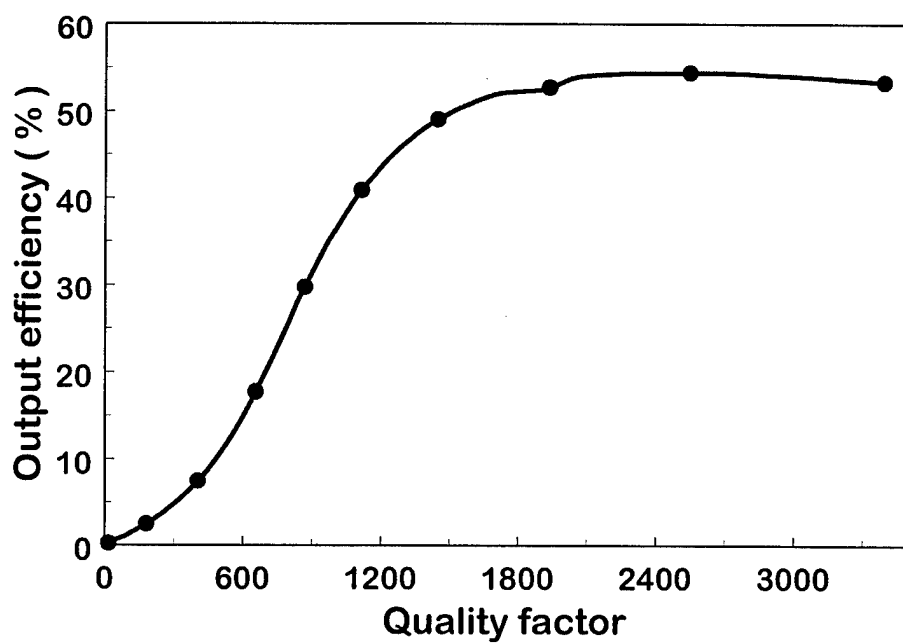
1. The axially-modulated, cusp-injected, small-orbit gyrotron: (a) system schematic, (b) axial magnetic field profile, and (c) normalized electric field profile at the beam radius ( $E_z$  in the input cavity and  $E_\phi$  in the output cavity).



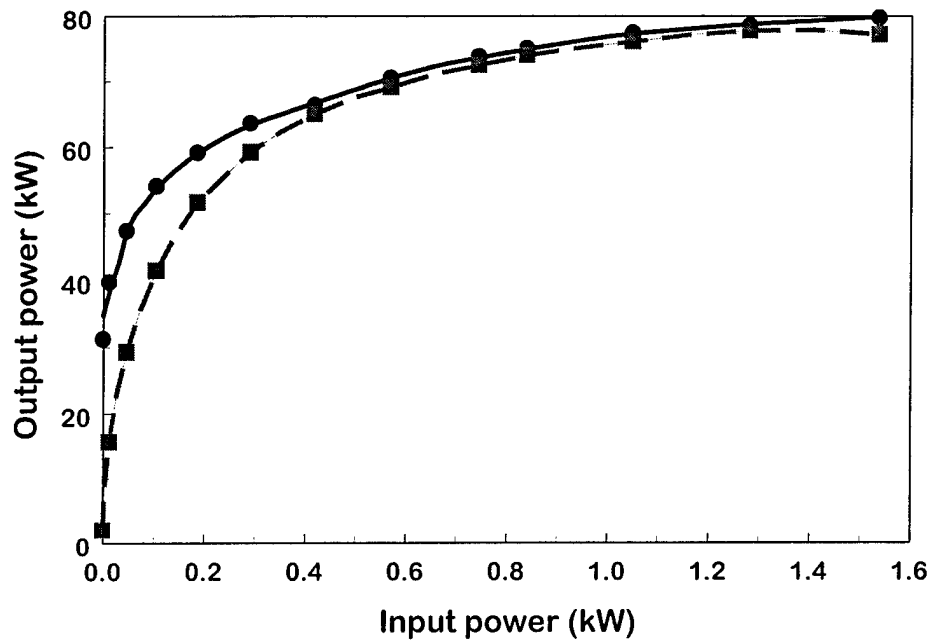
2. The output cavity start-oscillation curves. The squares indicate the TE<sub>011</sub> mode and the circles represent the TE<sub>111</sub> mode.



3. Representative phase distribution of electrons: (a) output cavity entrance ( $P_{in}=0$  W), (b) output cavity entrance ( $P_{in}=800$  W), and (c) output cavity exit ( $P_{in}=800$  W).

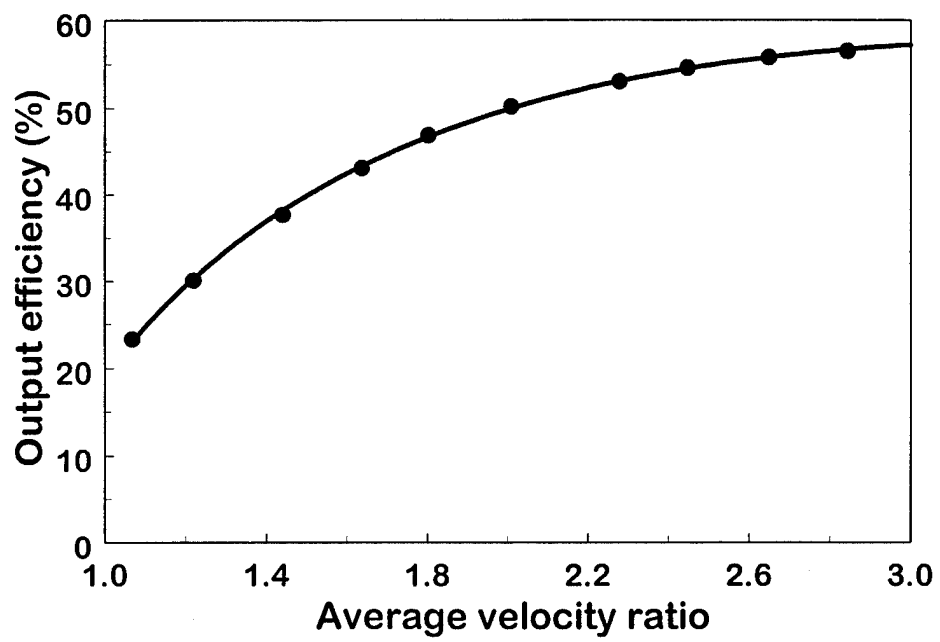


4. The dependence of output efficiency on the output cavity quality factor ( $P_{in}=800$  W).

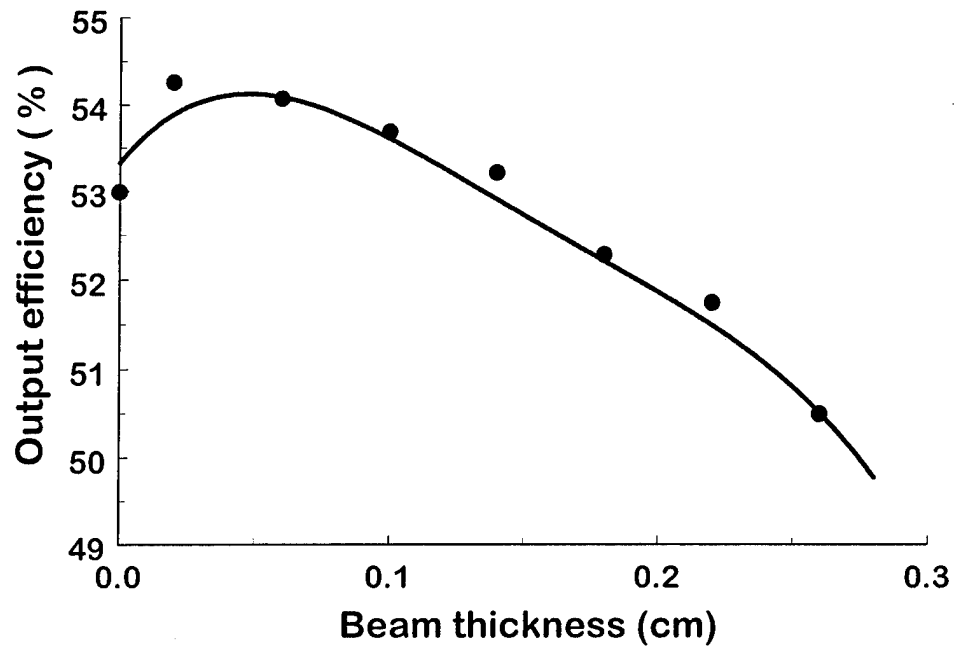


5. System drive curves. The solid line shows the output efficiency at the optimal electric field strength. The dashed line gives the output efficiency for a constant quality factor ( $Q=1825$ ).

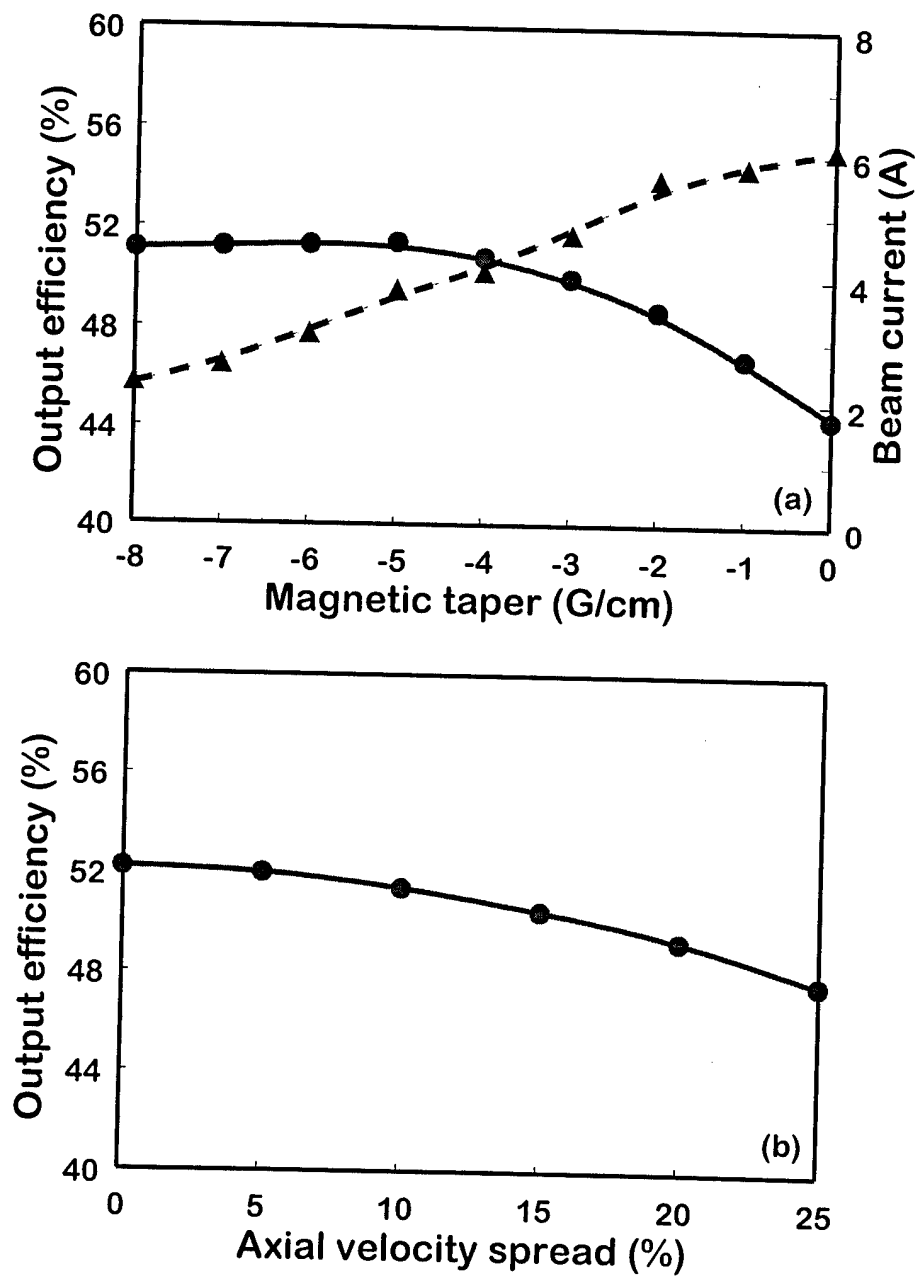




6. The dependence of output efficiency on average velocity ratio.



7. The dependence of output efficiency on beam thickness.



8. Gyrokystron code results: (a) output efficiency (solid line) and optimal current (dashed line) as a function of magnetic field taper and (b) output efficiency as a function of velocity spread.

# **Design of an Efficient, Low Voltage, Third Harmonic, Large-Orbit Gyrotron Amplifier with a Vane-Resonator Output Cavity**

W. Lawson, W. W. Destler, A. Fernandez, A. Liu, J. Rodgers, and J. Weinstein  
Electrical Engineering Department and Institute for Plasma Research  
University of Maryland, College Park, MD 20742

## Abstract

We present the design of a 100 kW, J-band, third harmonic large-orbit gyrotron amplifier which utilizes the interaction between a 45 kV, 4 A beam and a vane resonator output cavity operating in the " $\pi$ "-mode. An efficiency of 55% is predicted with a large signal gain near 20 dB by a single particle code which takes into account non-ideal effects associated with finite beam thickness and finite magnetic field transition widths. High efficiency is achieved by velocity modulation of an axially-streaming annular beam via a short  $TM_{310}$  drive cavity. Ballistically created axial bunches are converted into azimuthal bunches when the beam encounters a non-adiabatic, balanced magnetic field reversal at the end of a 30 cm drift region. The design of this tube is presented and its performance is completely characterized before the prospects for the operation of this low voltage configuration at other harmonics are explored.

## I. INTRODUCTION

Microwave generation at high harmonics of the cyclotron frequency from large-orbit gyrotrons has undergone considerable theoretical and experimental scrutiny in the past two decades at a number of institutions [1-16]. Because of the reduced magnetic field requirements, these devices potentially have a considerable advantage over conventional first harmonic gyrotrons [17-19] in a number of applications that require compact, lightweight tubes. The chief disadvantage of high harmonic operation is the reduction in efficiency that usually accompanies any increase in harmonic number. One possible way to compensate for this weakness is to use energy recovery techniques to restore the net efficiency to a level comparable to the first harmonic devices [13,20,21]. Unfortunately, this approach adds to the complexity of the power supply and microwave output system. Also, there is typically a large capital cost associated with the collector hardware (insulators, electrodes, magnets, etc.). Furthermore, this approach does nothing to reduce cathode loading requirements or space-charge effects in the gun and beam transport system.

An alternate approach to enhanced efficiency involves pre-bunching the beam to achieve a non-uniform phase-space distribution prior to the entrance of the output cavity. Several such efficiency enhancement techniques have been attempted in linear devices [22-24], and all of them may be applicable to those large-orbit devices which introduce perpendicular energy into the beam via a non-adiabatic, magnetic field reversal. One of these techniques utilizes a modified version of the klystron's ballistic bunching process to generate the required velocity distribution. A device based on this technique, which we call the axially-modulated, cusp-injected, large-orbit gyrotron, has been explored in an earlier paper for a system with a 100 kV, 25 A beam [25].

A schematic of this device is shown in Fig. 1. The axial bunches are created ballistically after the beam passes through an input cavity which is driven with a  $TM_{m10}$  circularly-polarized mode. The axial bunches are converted into azimuthal bunches when the beam encounters the non-adiabatic magnetic transition (cusp). If the drive frequency is at the  $m^{\text{th}}$  harmonic of the cyclotron frequency, the net effect is that the beam will form  $m$  spokes that will rotate at the cyclotron frequency. If an output cavity that operates in a  $TE_{mnp}$  mode is placed immediately after the cusp, efficient energy extraction can occur. For example, the previous design study demonstrated

that an efficiency of 40% was achievable in X-Band at the fourth harmonic via an interaction with a right-circular  $TE_{411}$  cavity.

While the result quoted in the previous paragraph appears promising, there are some practical limits to the applicable range of parameters for this device. Of particular concern is the quality factor required to produce the optimal field strength in a low voltage, low current device operating at a high harmonic number. For example, the radius of the maximum electric field in a cavity, relative to the wall radius, increases with increasing harmonic number. Thus, the higher the harmonic number the further out the beam should be. However, the beam radius of the large-orbit configuration is equal to the Larmor radius, which, for a particular cyclotron frequency, is proportional to the perpendicular velocity. Thus, the beam radius in low voltage systems decreases fairly rapidly with decreasing beam energy. These two seemingly incompatible requirements often combine to yield an unrealistic requirement on the output cavity quality factor.

There are at least two ways to overcome this difficulty and design efficient, low voltage, harmonic devices. One way is to use a pre-bunched, small-orbit beam. Axial modulation is a viable technique for this approach because a non-reversal, non-adiabatic magnetic transition can be used to generate the small orbit beam. The guiding center radius can be adjusted to place the beam at a location where the electric field is relatively strong. This approach has been investigated previously via the design of a second harmonic small-orbit system [26]. In this design, a 35 kV, 4 A beam was pre-bunched by a short  $TM_{020}$  cavity and interacted with a 10 cm long  $TE_{011}$  output cavity to theoretically produce over 70 kW of power in X-Band. The simulated efficiency and large-signal gain were approximately 53% and 20 dB, respectively, when the beam thickness and finite magnetic transition width were taken into consideration. At approximately 1800, the required output cavity quality factor was well below the resistive  $Q$  of 28,600 and the cavity was stable to all spurious modes. However, the simulations indicated that the quality factor of a comparable third harmonic system would be too large.

The second approach is to use a vane-resonator to couple various azimuthal modes together. The resultant cavity modes can support the necessary azimuthal field variation with a much lower cutoff frequency. Thus, the wall radius can be reduced considerably as compared to the smooth wall case and the interaction impedance can be significantly increased. This is the approach that we will investigate in this paper. In the next section we will discuss the basic ampli-

fier configuration and describe the computer codes used in the analysis. In Section III, we will present the results of a third harmonic example which utilizes a 45 kV, 4 A beam to efficiently generate 100 kW of power at 5.5 GHz. These parameters were selected to facilitate a future proof-of-principle experiment in our laboratory. In addition to characterizing tube stability and large-signal characteristics, we will also discuss the sensitivity of the device to parameter variations. The results of this study and prospects for high harmonic operation are summarized in the final section.

## II. DEVICE OPERATION AND MODELING

A detailed description of the operation of this device was given in [25]. In this section we briefly note the key aspects of the design and simulation processes and detail only the novel aspects of this work, which involve the use of a vane resonator (VR) output cavity.

In order to maximize the circuit gain, the beam must be placed near the maximum of the axial electric field in the input cavity, which is increasingly close to the wall radius with increasing harmonic number. The wall radius in a  $TM_{m10}$  cavity is proportional to the drive signal's wavelength while the beam radius is tied to the magnetic field and the beam energy. This problem is easier to remedy than the analogous one with the output cavity: either the input cavity can be moved into the magnetic field's adiabatic compression region where the beam radius is larger (if one exists) or dielectrics can be inserted into the input cavity to decrease the wall radius. We have selected the latter approach for this design. Because the cavity is short and the beam is thin and streaming linearly in that region, there should be no problem with charge build-up. We model the cavity with a code that assumes three dielectric regions radially and calculates the quality factor assuming a good conducting (copper) wall and an ideal dielectric.

The required drift tube length  $d$  depends on the magnitude of the energy spread ( $\Delta E/E_o$ ) imparted to the beam:

$$d = \beta_o \lambda / (2 \Delta E/E_o) \quad (1)$$

where  $\beta_o$  is the streaming velocity (normalized to the speed of light) and  $\lambda$  is the EM wavelength (of the input cavity signal). The magnetic transition at the end of the drift region is shortened by a thin iron pole piece. Long solenoids on either side of the pole piece generate approximately constant axial magnetic fields in each region ( $B_c$  on the input side and  $B_o$  on the output side). The axial magnetic field is modeled by a piece-wise linear function and the radial field is given by Maxwell's equations. The spread in beam energy translates into additional velocity spread after the magnetic transition. When the effects of the input cavity's magnetic fields are neglected, the induced spread can be approximated by [25]:



$$\begin{aligned}\frac{\Delta v_z}{v_{z_o}} &= \frac{1}{2} \left[ 1 + \alpha^2 + \alpha^2 (\gamma_o^2 - 1) \right] \frac{\Delta E}{E_o} \\ \frac{\Delta v_{\perp}}{v_{\perp_o}} &= -\frac{1}{2} (\gamma_o^2 - 1) \frac{\Delta E}{E_o}\end{aligned}\quad (2)$$

In (2),  $\gamma_o$  is the relativistic mass factor.

A single particle code is used to simulate the beam's motion through the input cavity, the drift region, and the non-adiabatic magnetic transition. Given the beam parameters, electrons are initially "launched" over a range of axial positions, times, and angles that represent the entirety of phase space (after taking into account any symmetries in the system). The initial velocities of the particles are assumed to be purely axial. A minimum of 100 particles are used to model the beam when zero radial beam thickness is assumed and more than 300 particles are used to model finite thickness beams. After a Runge-Kutta start-up, a predictor-corrector integration scheme is used to solve the equations of motion. Convergence is checked by varying the time step and the number of particles and by verifying conservation of energy and canonical angular momentum for each particle. This "buncher" code produces the phase space distributions of the electrons at the end of the transition region, calculates the key beam statistics (*e.g.* the average velocity ratio and guiding center radius and the spreads in  $v_{\perp}$ ,  $v_z$ , and energy), and indicates the effectiveness of the bunching process.

A cross-section of the output cavity is displayed in Fig. 2. The wall radius is denoted  $r_w$  and the slot depth is  $d_s$  so that the slot radius is  $r_s = r_w + d_s$ . We assume that there are  $n_s$  slots, so that the angular span of one period is  $\theta_r = 2\pi / n_s$ . The angular opening of each slot is  $\Delta\theta$ . To solve for the dispersion relation and subsequently the cutoff wavenumbers for the VR structure, we make the usual approximation of a constant electric field across the slot opening and match the magnetic field there only on average [13]. If we let the phase advance between adjacent slots be:

$$\varphi_a = 2\pi l_o / n_s \quad (3)$$

where  $l_o$  is an integer in the range  $0 \leq l_o \leq n_s$ , then the dispersion relation is given by:

$$\frac{J_o(x_w)Y'_o(x_s) - Y_o(x_w)J'_o(x_s)}{J'_o(x_w)Y_o(x_s) - Y'_o(x_w)J_o(x_s)} = \left( \frac{\Delta\theta}{\theta_r} \right) \sum_{q=-\infty}^{+\infty} \frac{J_{l_o+qn}(x_w)}{J'_{l_o+qn}(x_w)} \left\{ \frac{\sin[(l_o + qn)\Delta\theta / 2]}{(l_o + qn)\Delta\theta / 2} \right\}^2. \quad (4)$$

Here  $x_w = r_w \xi$  and  $x_s = r_s \xi$ , for  $\xi = \sqrt{(\omega / c)^2 - k_z^2}$ , and where  $\omega$  is the angular frequency,  $c$  is the speed of light, and  $k_z$  is the axial wavenumber.  $J_n(x)$  and  $Y_n(x)$  are Bessel functions of the first and second kind, respectively.

A simple code is used to find the cutoff frequency of a VR structure from (4), given the dimensions listed above and a particular value of  $l_o$ . The usual two operating modes are the “ $\pi$ ”-mode ( $l_o = n_s / 2$ ) and the “ $2\pi$ ”-mode ( $l_o = 0$ ). We will only consider the “ $\pi$ ”-mode in this paper because it has in general a lower start-oscillation threshold than the other mode. The EM fields are generated by specifying an axial length for the cavity and assuming that the axial variation is sinusoidal (the closed cavity approximation). The resistive quality factor is calculated by assuming a good conductor (copper) wall, evaluating the magnetic field at all surfaces, and integrating the wall losses either analytically or numerically. The actual resistive  $Q$  will presumably be somewhat larger, since the endwalls will be partially removed.

A second single particle code takes the results from the “buncher” code and uses the same numerical techniques to calculate the extraction efficiency of the EM wave in the output cavity under steady-state conditions. The “efficiency” code also takes the results from the output cavity code to generate the electromagnetic fields. The applied dc magnetic field in the output cavity is assumed to vary linearly. This “efficiency” code is iterated, while varying the cavity and magnetic field parameters, until an optimal design is achieved. During each run, the amplitude and phase of the wave are adjusted until maximum efficiency is obtained. In addition to the efficiency, the code reports the required diffractive  $Q$ . By decreasing the field amplitude in the output cavity towards zero, this code is used to calculate the start currents for the various modes in tapered magnetic fields. The code has been benchmarked successfully against the start-oscillation results in [8] by using an unbunched beam.

### III. SIMULATION RESULTS FOR A THIRD HARMONIC DESIGN

The parameters for a third harmonic large-orbit design are given in Table I. The system is designed to produce microwaves at 5.5 GHz via the interaction between a 45 kV, 4 A beam and the microwave circuit. Given the beam energy and the expected magnetic field level, the beam radius of 1.125 cm is required to provide a velocity ratio near 2.2. This beam can be generated with a thin annular cathode and a modest magnetic compression. For example, a compression of about seven would result in a cathode loading of slightly above  $1 \text{ A/cm}^2$ , an average emitter radius of 3 cm, and a cathode thickness of 2 mm. The radial thickness indicated corresponds to an ideal post-cusp velocity spread from canonical angular momentum considerations of about  $\Delta v_{\perp} = 1.9\%$ . The dc space charge depression in the entire circuit is negligible.

The drive cavity is a dielectric-loaded, right-circular  $\text{TM}_{310}$  cavity with the dimensions indicated in Table I. The cavity width is selected to give a beam coupling factor [27] of about 0.98. A dielectric with a relative permittivity of about 13 is assumed to be placed above and below the beam location, leaving a clearance of at least 1 mm. The cavity radius is adjusted to achieve the desired operating frequency. With these parameters, the axial electric field shown in Fig. 3 is realized. Thus, the beam is located in a region where the electric field is nearly constant and optimal. The azimuthal magnetic field is also indicated in the figure. This field is quite small near the beam radius and has little effect on particle motion. The radial magnetic field is similar in profile to the electric field and is not shown. There are a number of good dielectrics with relative permittivities near 10 and we expect that a real device would use one of these and would also possibly place the cavity near the end of the magnetic compression region to maximize the gain.

The dc magnetic field profile throughout the circuit is determined during the efficiency optimization procedure. The axial magnetic field at the entrance to the output cavity is such that three times the cyclotron frequency is about 14% lower than the drive frequency. The 13% up-taper leaves the drive frequency nearly equal to thrice the cyclotron frequency at the output cavity end. The magnetic transition is not perfectly balanced; the field strength in the drift region is about 8% lower than the initial field after the transition. The distance between the input cavity and cusp transition is optimized with the numerical codes, but the initial length is chosen from

(1) so that maximal bunching could be achieved with an energy spread under 4%. The transition width should readily be achievable with the aid of one or more iron pole pieces.

The length of the output cavity is varied to maximize efficiency while keeping the required  $Q$  less than 10% of the resistive  $Q$  of a copper cavity. This restriction allows for extraction of about 90% of the microwave power. The chosen length is such that unperturbed particles undergo approximately  $4\frac{1}{2}$  revolutions inside the cavity. The cavity radius is selected to minimize beam interception and the slot depth is adjusted to produce the required resonant frequency. Six vanes are required for “ $\pi$ ”-mode operation. The slot opening is fixed at 50% of the angular period. The azimuthal electric field and axial magnetic field radial profiles are plotted in Fig. 4 at a fixed azimuthal location which corresponds to the center of a vane. They are, of course, out of time phase by  $90^\circ$ . The discontinuity in the curves at  $r_w$  results from the truncation of the infinite series in (4). The azimuthal electric field at the initial average beam radius is nearly half of the peak field.

The beam current required to achieve self-oscillation in the “ $\pi$ ”-mode of the output cavity is shown in Fig. 5 as a function of (uniform) magnetic field. It is assumed that no drive power is applied to the input cavity. The resonant frequencies of the various azimuthal modes are given in Table II. The “ $\pi$ ”-mode is the only unstable mode in the magnetic field range from 600 to 700 G. However, even the “ $\pi$ ”-mode is stable for the optimal tapered magnetic field profile at the design current of 4 A. The optimal zero-drive efficiency is found to be 27% at a starting magnetic field of 662 G and a weak uptaper..

The simulated results for the parameters in Table I near the optimal drive power are summarized in Table III. The nominal electric field at the average beam location is about 11 kV/cm in the input cavity and almost double that in the output cavity. The total axial velocity spread includes a contribution of about 1.9% from energy spread, which is substantially below the estimate given in (2) because of ac magnetic field effects. The contribution to the perpendicular velocity spread from the energy spread is about 1.7%. The bunching effectiveness is quantified by computing the RMS angular distribution of particles at the entrance to the output cavity, relative to the phase of the EM wave. This value is scaled and subtracted from 100% to yield a value of 0% for a uniform beam and a value of 100% for a perfectly bunched beam. The nominal saturated gain is just above 19 dB. The simulated efficiency of 55% is more than twice the maximum

unbunched efficiency and is comparable to or better than the optimal theoretical efficiencies of most first harmonic gyrotrons. With a 180 kW beam, about 100 kW of microwave power should be produced.

The axial evolution of electron bunching in the device at the optimal point is illustrated in Fig. 6, where the  $r$ - $z$  projection of the trajectories of representative particles are plotted. The input cavity entrance is at  $z=0$ . The scalloping of the beam in the drift region is due to the Lorentz force brought about by the radial magnetic field in the input cavity. Since the guiding center radius of the beam is nearly zero, a particle's radial location is a good indication of its energy. The interaction between the wave and the beam is quite strong, with many particles gaining energy in the first half of the cavity only to lose it in the second half. Clearly the cavity radius is just large enough to avoid beam scrape-off. A larger radius could be used, but the required quality factor would increase.

Figure 7a shows the distribution of representative particles in the transverse plane (for the same optimal parameters of Fig. 6) at the entrance to the output cavity. Though it is difficult to quantify the angular density distribution, three distinct particle bunches are clearly visible. The resultant phase distribution at the exit of the output cavity is shown in Fig 7b. The phase coherence of the beam is essentially destroyed and a large number of particles have given up the majority of their perpendicular energy. A much smaller number of particles have remained at about the same energy level or had their energy increase slightly.

The efficiency is plotted in Fig. 8 as a function of beam thickness. Also indicated in the figure is the axial velocity spread computed by the "buncher" code. The maximum efficiency of over 67% is obtained with a zero thickness beam. The efficiency drops steadily to about 55% at the nominal design thickness and begins to fall off more rapidly after that point. The bunching effectiveness (not plotted) is essentially independent of beam thickness. The required quality factor varies slowly from 1070 at zero thickness to 1240 at the 0.75 mm point and then jumps to 1520 at the final point. The increase in velocity spread (from canonical angular momentum conservation) is believed to be the main cause for the decrease in efficiency. Beam scrape-off is probably also a contributing factor to the efficiency degradation, particularly at the final thickness point. If a shielded electron source, such as the Advanced Center-Post gun [28], were used instead of an immersed emitter, efficiencies for a finite thickness beam could approach 67%. In

the remainder of this section we present mainly the characteristics of the zero-thickness (or shielded) beam; the characteristics of the 0.75 mm beam are found to be similar, with a reduction in efficiency of about 10% near the optimal power points.

The drive curve near the optimal system parameters (but with a zero thickness beam) is shown in Fig. 9. The relative bunching effectiveness is given in the figure by the dashed line. The curve is generated assuming a constant quality factor in the output cavity of about 1100. The device is zero-drive stable and enjoys a fairly broad saturation region. The induced energy spread in the beam is about 6.2% at the maximum drive power of 3 kW.

The dependence of efficiency on output cavity  $Q$  is displayed in Fig. 10. All other parameters are held fixed at the optimal system configuration values. The output efficiency rises steadily from zero to about 45% as the quality factor is increased to 875. After that point, the efficiency increases more rapidly with  $Q$  until it reaches its maximum value of  $\sim 1100$ . Electric fields that are indicative of quality factors above 1150 result in beam scrape-off and consequently are not plotted. Undoubtedly, scrape-off could be avoided and comparable efficiencies achieved if we were to adjust some of the other parameters (e.g. magnetic field taper).

The dependence of output efficiency on the thin beam's average velocity ratio is given in Fig. 11. This ratio is modified solely by varying the magnetic field in the drift region; the required field at each point is indicated in the figure by the dashed line. The phase and amplitude of the output cavity's electric field are optimized at each point. This implies that the quality factor is adjusted to maximize output power. All other parameters, however, are held at their nominal values. The first maximum in efficiency is 67%, occurs near the nominal velocity ratio of 2.2, and drops off fairly rapidly with decreasing velocity ratio, going to a level of about 13% at a velocity ratio near one. The maximum quality factor of 1850 is required at the minimum efficiency point. There is a dip in the efficiency near a velocity ratio 2.35 before it returns to the 67% level at a velocity ratio of 2.5. A buncher field of 610 Gauss yields a velocity ratio above 2.8 and results in particle reflections in the output cavity's tapered magnetic field.

## IV. DISCUSSION

In this paper we have demonstrated, via a concrete design, the feasibility of the low voltage, high efficiency, pre-bunched, gyrotron concept at the third harmonic. The principle extension of this work beyond our previous study [25] involves the introduction of a vane-resonator output cavity. This configuration allows a reduction in the transverse dimensions of the cavity for a given frequency and azimuthal mode number and results in vastly improved beam coupling to low energy, axis-encircling beams. With this approach, we are able to produce simulated efficiencies of 67% with a shielded beam and 55% with an immersed beam (which had an axial velocity spread of about 9%). With a beam voltage of 45 kV and a current of 4 A, the resultant power is 100 kW. The design is most sensitive to the required output cavity quality factor, which at the optimal point is acceptable at less than 10% of the output cavity's resistive  $Q$ .

We have also taken a preliminary look at efficiency enhancement in higher harmonic systems with comparable beam voltages. In Fig. 12a, we plot the simulated efficiency of the large-orbit device as a function of harmonic number. The solid line indicates the simulated efficiency achievable for a zero-thickness beam and the dashed line gives the 0.75 mm beam result. The third harmonic point corresponds to the system described in the previous section. For the other harmonic results, the magnetic field and beam parameters are fixed at the values given in Table I. However, the cavity-cusp spacing, and the cavities' harmonic number, radial dimensions, and number of (output) vanes are adjusted to the appropriate values. Furthermore, the output cavity quality factor is adjusted to optimize efficiency. With the exception of the second harmonic result, the finite beam thickness results in an efficiency decrease of about 10 - 12%.

In Fig. 12b we plot the required output quality factors for the thin (solid line) and thick (dashed line) beams. Operation above the fourth harmonic is not practical because the required  $Q$  is comparable to or exceeds the resistive  $Q$  of a copper cavity (given by the dot-dashed line in the figure). These results for the higher harmonics can undoubtedly be improved upon by a more complete optimization (e.g. adjustment of the output cavity length), but the basic trend would still persist. Thus, operation at harmonics significantly above the fourth will require an increase in beam voltage and / or power.

In the near future, we will attempt a proof-of-principle experiment based on this concept. We are in the process of building a test bed which is energized by a 50 kV, 20 A, 5  $\mu$ s pulse-line

modulator. The frequency in this study is selected to be compatible with sources and magnetic field coils which are readily available to us. We are currently designing an electron gun that is compatible with the beam parameters of this design.

This work was supported by the Department of Defense Tri-Services Program for Vacuum Electronics.



Table I. Third Harmonic Amplifier System Parameters.

Beam Parameters	
Voltage (kV)	45
Current (A)	4
Average radius (cm)	1.125
Beam thickness (mm)	0.75
Streaming velocity $\beta_0$	0.394
Velocity ratio ( $v_\perp/v_z$ )	2.200
Input Cavity	
Drive frequency (GHz)	5.5
Operating mode	TM <sub>310</sub>
Resistive Quality factor (Q)	2170
Radius (cm)	1.701
Length (cm)	0.225
Magnetic Field Parameters	
Buncher magnetic field (G)	-567
Output magnetic field (G)	613
Cyclotron frequency (GHz)	1.577
Cusp width (cm)	0.375
Cavity - cusp spacing (cm)	30
Output field taper	13%
Output cavity	
Output frequency (GHz)	5.5
Operating mode	$\pi$ -mode
Diffraction Q	1240
Resistive Q	13,430
Length (cm)	15.000
Radius (cm)	1.763
Slot depth (cm)	0.747
Slot width (%)	50
Number of vanes	6

Table II. Resonant frequencies of the VR structure.

$l_o$	Resonant frequency (GHz)
0	7.231
1	3.686
2	5.055
3	5.500

Table III. Third Harmonic Amplifier Performance

Input cavity results	
Input drive power (kW)	1.16
$E_z$ at beam (kV/cm)	11.3
Drift region results	
Total $\Delta v_z$ (%)	9.07
Total $\Delta v_{\perp}$ (%)	2.50
Bunching effectiveness (%)	37.79
Energy spread $\Delta E$ (%)	3.88
Output cavity results	
Power (kW)	99.7
Efficiency (%)	55.4
Gain (dB)	19.3
$E_{\phi}$ at beam (kV/cm)	21.3

## REFERENCES

1. P. Sprangle, "Excitation of electromagnetic waves from a rotating annular relativistic  $e$ -beam," *J. Appl. Phys.* vol. 47, pp. 2935-2940, 1976.
2. W. W. Destler, D. W. Hudgings, M. J. Rhee, S. Kawasaki, and V. L. Granatstein, "Experimental study of microwave generation and suppression in a non-neutral  $e$ -layer," *J. Appl. Phys.* vol. 48, pp. 3291-3296, 1977.
3. H. S. Uhm and R. C. Davidson, "Intense microwave generation by the negative-mass instability," *J. Appl. Phys.* vol. 49, pp. 593-598, 1978.
4. W. W. Destler, R. L. Weiler, and C. D. Striffler, "High-Power microwave generation from a rotating  $E$  layer in a magnetron-type waveguide," *Appl. Phys. Lett.* vol. 38, pp. 570-572, 1981.
5. Y. Y. Lau and L. R. Barnett, "Theory of a low magnetic field gyrotron (gyromagnetron)," *Int. J. Infrared Millimeter Waves*, vol. 3, pp. 619-643, 1982.
6. W. W. Destler, R. Kulkarni, C. D. Striffler, and R. L. Weiler, "Microwave generation from rotating electron beams in magnetron-type waveguides," *J. Appl. Phys.* vol. 54, pp. 4152-4162, 1983.
7. W. Namkung, "Observation of microwave generation from a cusptron device," *Phys. Fluids*, vol. 27, pp. 329-330, 1984.
8. K. R. Chu and D. Dialetis, "Theory of harmonic gyrotron oscillator with slotted resonant structure," *Int. J. Infrared Millimeter Waves*, vol. 5, pp. 37-56, 1984.
9. W. Lawson, W. W. Destler, and C. D. Striffler, "High-power microwave generation from a large-orbit gyrotron in vane and hole-and-slot conducting wall geometries," *IEEE Trans. Plasma Sci.* vol. PS-13, pp. 444-453, 1985.
10. W. Lawson and C. D. Striffler, "A general linear growth rate formula for large orbit, annular electron beams," *Phys. Fluids*, vol. 28, pp. 2868-2877, 1985.
11. W. Lawson and C. D. Striffler, "A linear growth rate fluid formulation for large orbit, annular electron layers with finite thickness," *Phys. Fluids*, vol. 29, pp. 1682-1694, 1986.
12. E. Chojnacki, W. W. Destler, W. Lawson, and W. Namkung, "Studies of microwave radiation from a non-relativistic rotating electron beam in a multiresonator magnetron cavity," *J. Appl. Phys.* vol. 61, pp. 1268-1275, 1987.
13. W. W. Destler, E. Chojnacki, R. F. Heoberling, W. Lawson, A. Singh, and C. D. Striffler, "High-power microwave generation from large-orbit devices," *IEEE Trans. Plasma Sci.* vol. 16, pp. 71-89, 1988.

14. W. W. Destler, K. Irwin, W. Lawson, J. Rodgers, Z. Segalov, E. P. Scannell, and S. T. Spang, "Intense-beam fundamental mode large-orbit gyrotron studies," *J. Appl. Phys.* vol. 66, pp. 4089-4094, 1989.
15. C. S. Kou, D. B. McDermott, N. C. Luhmann, Jr., and K. R. Chu, "Prebunched high-harmonic gyrotron," *IEEE Trans. Plasma Sci.* vol. 18, pp. 343-349, 1990.
16. K. K. Tiong and S. P. Kuo, "Operation of a high harmonic cusptron oscillator," *Int. J. Electronics*, vol. 70, pp. 815-821, 1991.
17. R. S. Symons and H. R. Jory, *Advances in Electronics and Electron Physics*, C. Marton, ed. (New York: Academic Press, 1981), Vol. 55, Ch. 1, p. 1.
18. V. L. Granatstein, M. E. Read, and L. R. Barnett, *Infrared and Millimeter Waves*, K. Button, ed. (New York: Academic Press, 1981), Vol. 5, Ch. 5, p. 267.
19. K. E. Kreischer, T. L. Grimm, W. C. Guss, A. W. Mobins, and R. J. Temkin, "Experimental study of a high-frequency megawatt gyrotron oscillator," *Phys. Fluids B*, vol. 2, pp. 640-646, 1990.
20. A. Singh, W. Lawson, D. Goutos, W. R. Hix, C. D. Striffler, V. L. Granatstein, and W. W. Destler, "Beam conditioning for electron energy recovery systems in devices employing axis-encircling beams," *Int. J. Electronics*, vol. 65, pp. 351-368, 1988.
21. M. E. Read, W. Lawson, A. J. Dudas, and A. Singh, "Depressed collectors for high power gyrotrons," *IEEE Trans. Electron Dev. Part 2*, vol. 37, pp. 1579-1589, 1990.
22. H. M. Bizek, P. M. McIntyre, D. Raparia, and C. A. Swenson, "Gigatron," *IEEE Trans. Plasma Sci.* vol. 16, pp. 258-263, 1988.
23. M. Yoshioka, "Lasertron: A Pulsed rf source using a laser-triggered photocathode," *Jap. J. Appl. Phys.*, vol. 28, pp. 1079-1093, 1989.
24. D. H. Preist and M. B. Shrader, "The Klystrode - An unusual transmitting tube with potentials for UHF-TV," *Proceedings of the IEEE*, vol. 70, pp. 1318-1325, 1982.
25. W. Lawson and W. W. Destler, "The axially modulated, cusp-injected, large-orbit gyrotron amplifier," *IEEE Trans. Plasma Sci.* vol. 22, pp. 895-901, 1994.
26. W. Lawson, A. Grigoropolous, A. Liu, G. P. Saraph, J. Rodgers, and W. W. Destler, "Design of a high efficiency, low voltage, axially modulated, cusp-injected, second harmonic, X-band gyrotron amplifier," submitted to *IEEE Trans. Plasma Sci.*, August 1995.
27. R. E. Collin, *Foundations for Microwave Engineering*, (New York: McGraw-Hill, 1966), p. 468.
28. G. P. Scheitrum, T. Bemis, T. A. Hargreaves, and L. Higgins, "95 GHz harmonic gyrokystron," *Proc. SPIE*, vol. 2104, pp. 523-524, 1993.

### Figure Captions

- Figure 1. A schematic of the axially-modulated, cusp-injected, large-orbit gyrotron.
- Figure 2. Cross-sectional view of the vane resonator structure.
- Figure 3. Input cavity field radial profiles: axial electric field (solid line) and azimuthal magnetic field (dashed line).
- Figure 4. Output cavity field radial profiles: azimuthal electric field (solid line) and axial magnetic field (dashed line). The azimuthal angle is fixed at the center of a vane opening.
- Figure 5. The dependence of the start-oscillation current on magnetic field for the " $\pi$ "-mode.
- Figure 6. Axial evolution of the radial location of representative particles for the optimal efficiency parameters.
- Figure 7. The cross-sectional distribution of representative particles for the optimal efficiency parameters at (a) the entrance of the output cavity and (b) the exit of the output cavity.
- Figure 8. The dependence of output efficiency (solid line) and total axial velocity spread (dashed line) on beam thickness.
- Figure 9. The drive curve (solid line) for the zero-thickness beam when the output cavity  $Q$  is  $\sim 1100$ . The dashed line indicates the bunching efficiency.
- Figure 10. The dependence of output efficiency on output cavity  $Q$  for the zero-thickness beam.
- Figure 11. The dependence of output efficiency on average velocity ratio (solid line). The required drift tube magnetic field is indicated by the dashed line.
- Figure 12. (a) The efficiency as a function of harmonic number for a zero-thickness beam (solid line) and a 0.75 mm thick beam (dashed line). The output cavity length is fixed at 15 cm and the magnetic field taper is fixed at 13%, but the drive frequency is proportional to the harmonic number. The remaining design parameters are adjusted to be compatible with the drive frequency. (b) The required quality factor for the zero-thickness beam (solid line) and the finite thickness beam (dashed line).

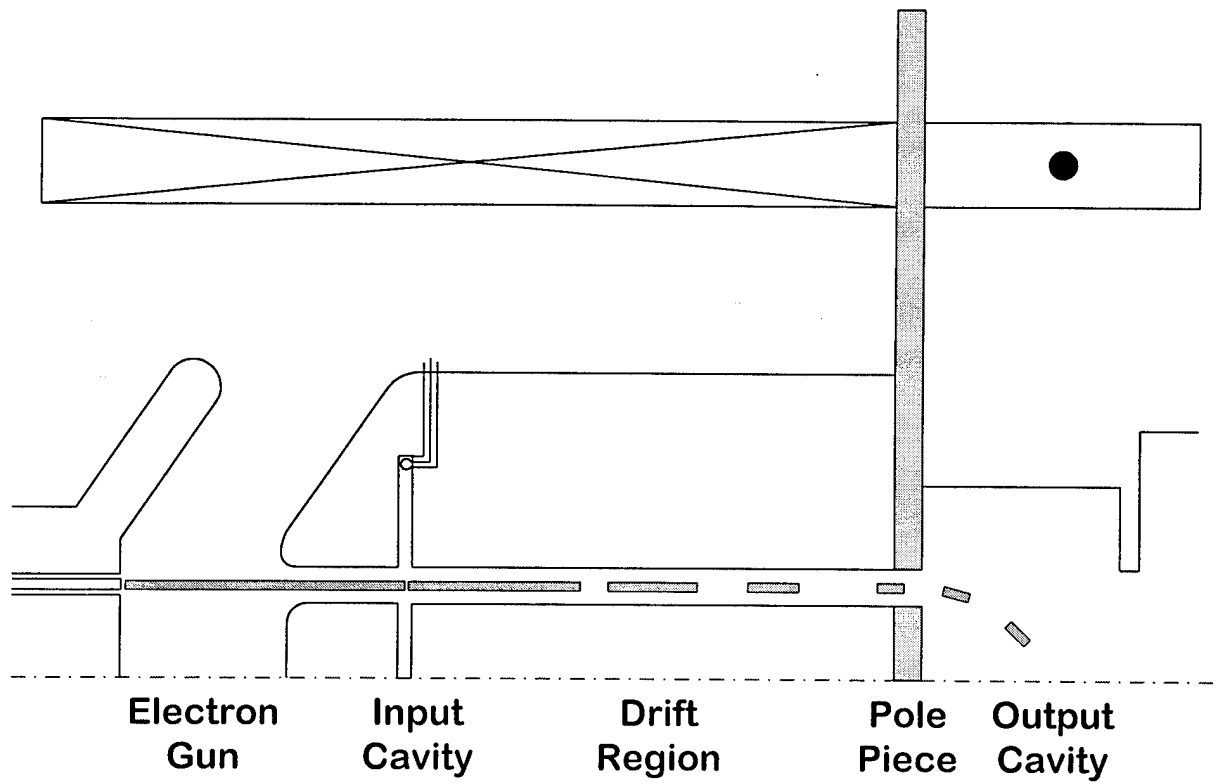


Figure 1. A schematic of the axially-modulated, cusp-injected, large-orbit gyrotron.

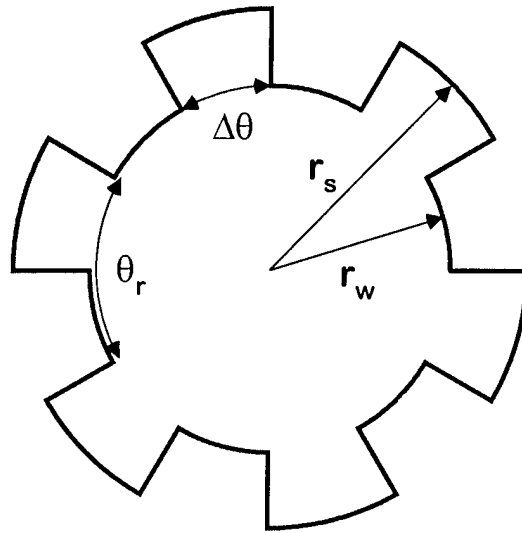


Figure 2. Cross-sectional view of the vane resonator structure.

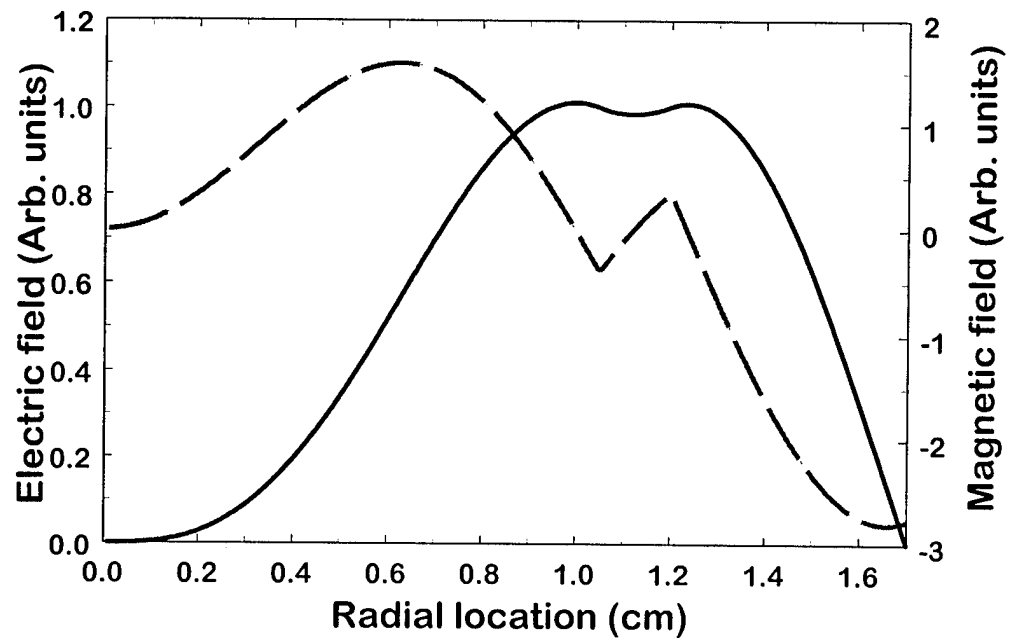


Figure 3. Input cavity field radial profiles: axial electric field (solid line) and azimuthal magnetic field (dashed line).



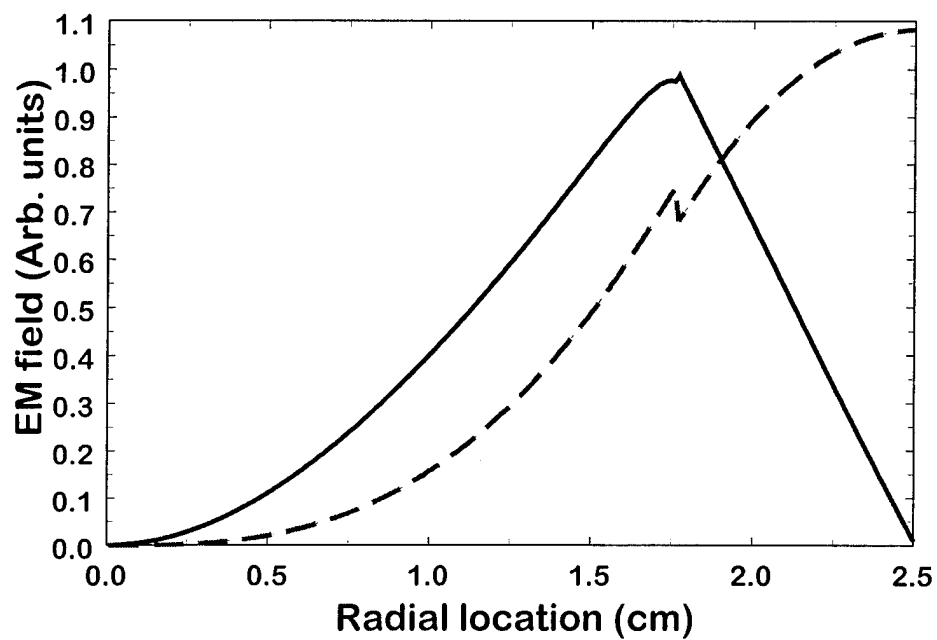


Figure 4. Output cavity field radial profiles: azimuthal electric field (solid line) and axial magnetic field (dashed line). The azimuthal angle is fixed at the center of a vane opening.

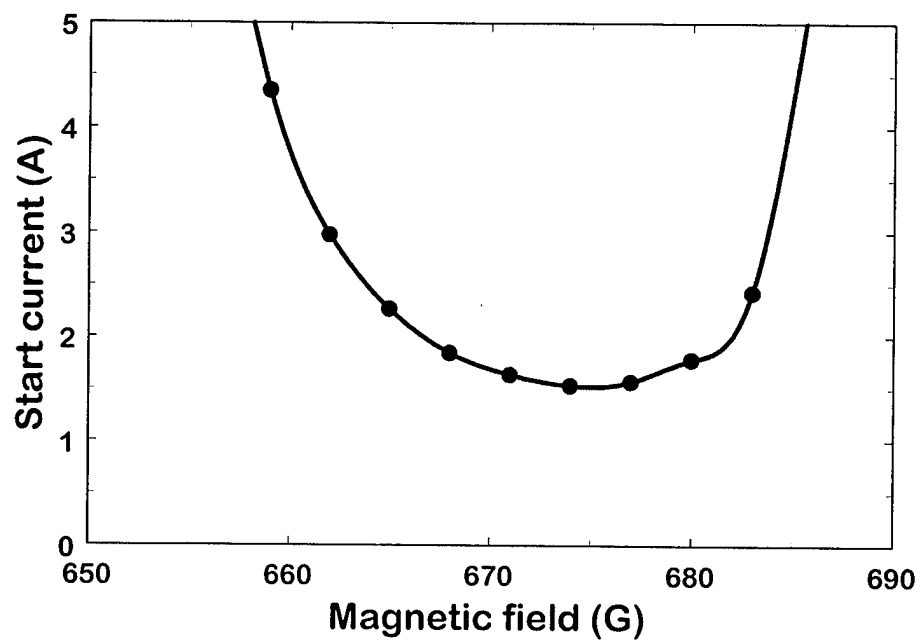


Figure 5. The dependence of the start-oscillation current on magnetic field for the “ $\pi$ ”-mode.

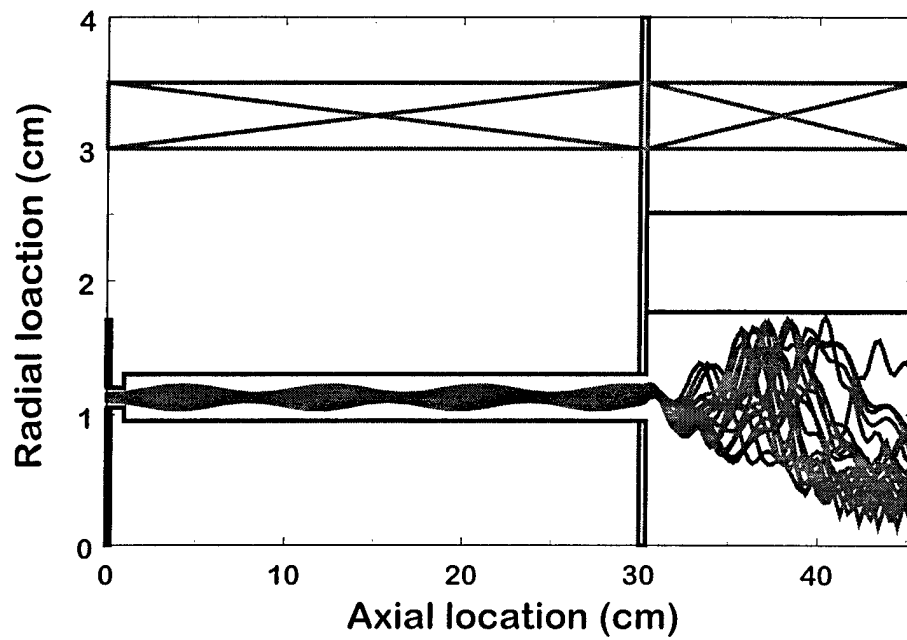


Figure 6. Axial evolution of the radial location of representative particles for the optimal efficiency parameters.

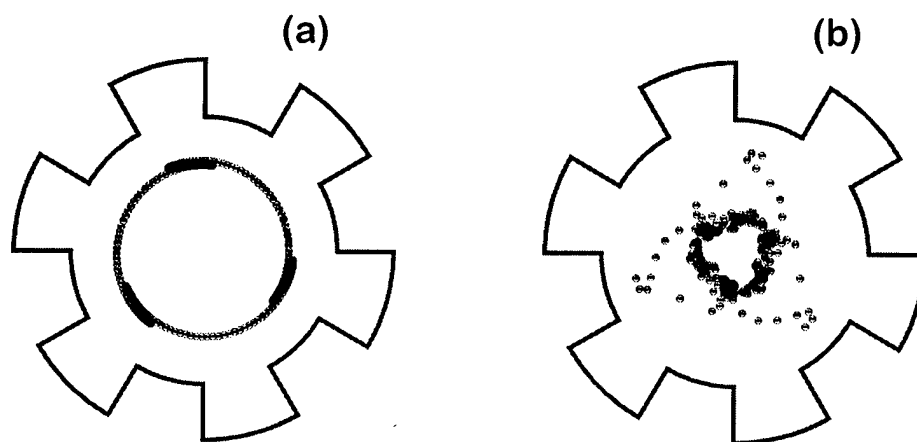


Figure 7. The cross-sectional distribution of representative particles for the optimal efficiency parameters at (a) the entrance of the output cavity and (b) the exit of the output cavity.

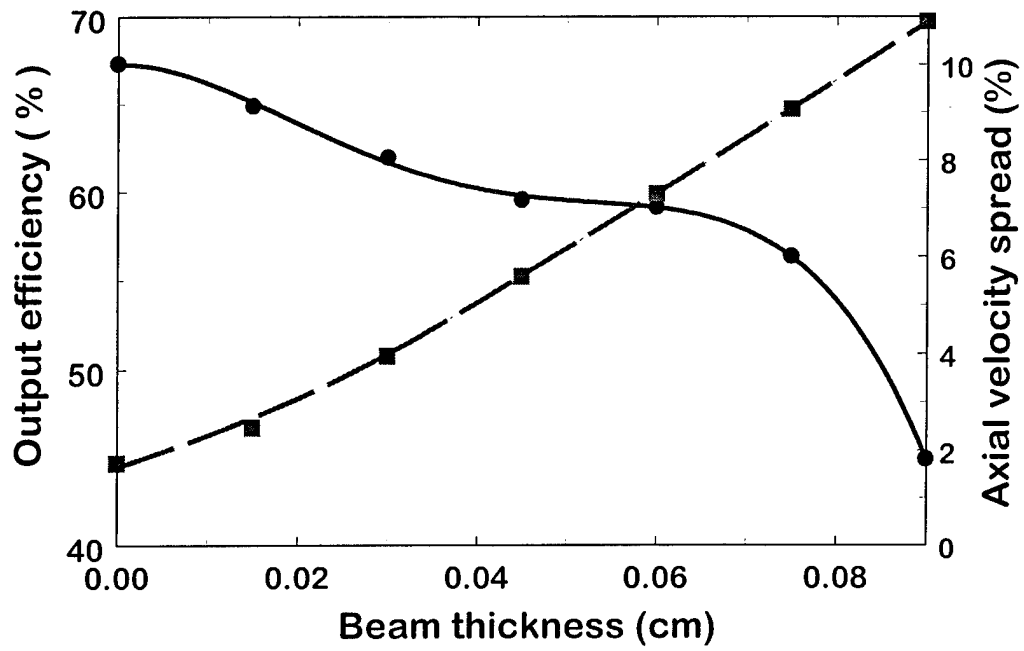


Figure 8. The dependence of output efficiency (solid line) and total axial velocity spread (dashed line) on beam thickness.

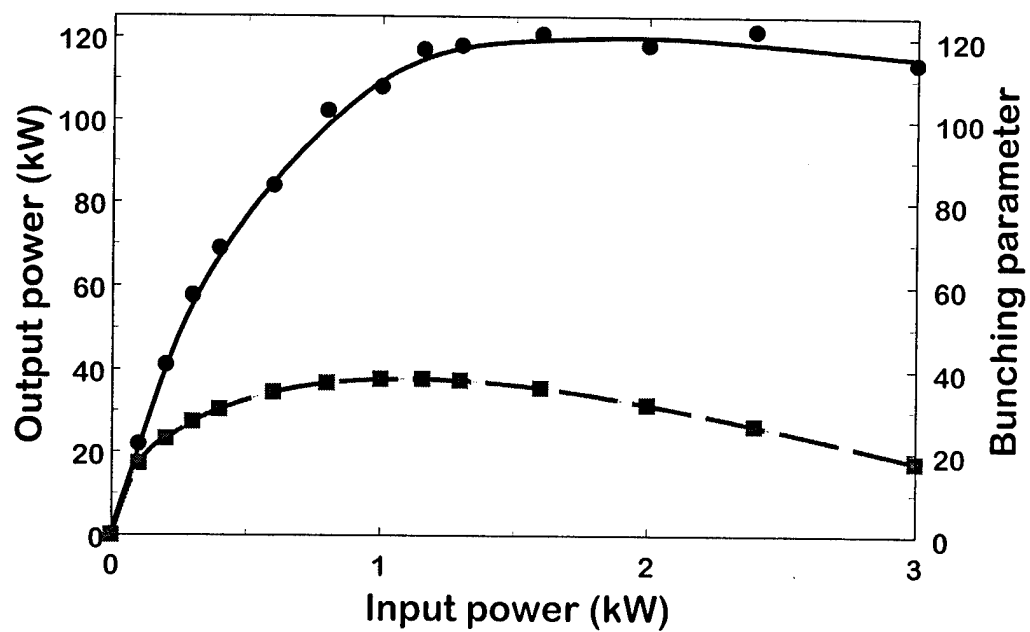


Figure 9. The drive curve (solid line) for the zero-thickness beam when the output cavity  $Q$  is  $\sim 1100$ . The dashed line indicates the bunching efficiency.

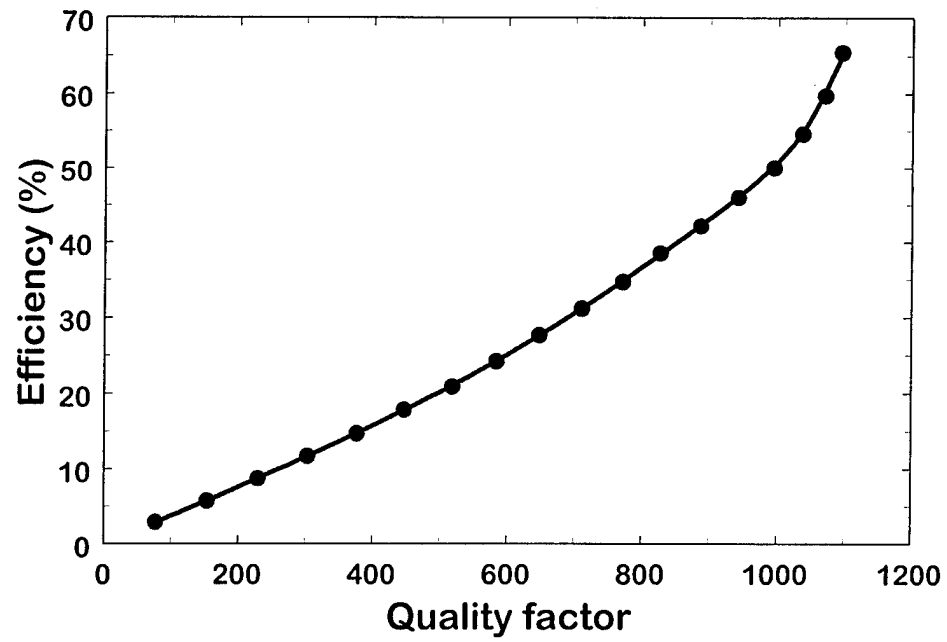


Figure 10. The dependence of output efficiency on output cavity  $Q$  for the zero-thickness beam.

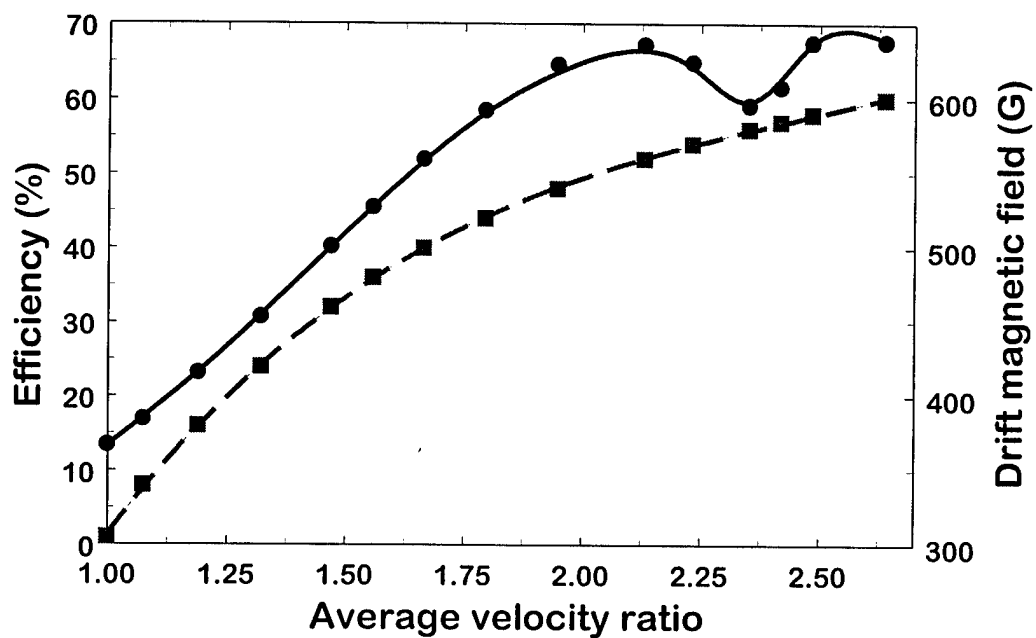


Figure 11. The dependence of output efficiency on average velocity ratio (solid line). The required drift tube magnetic field is indicated by the dashed line.



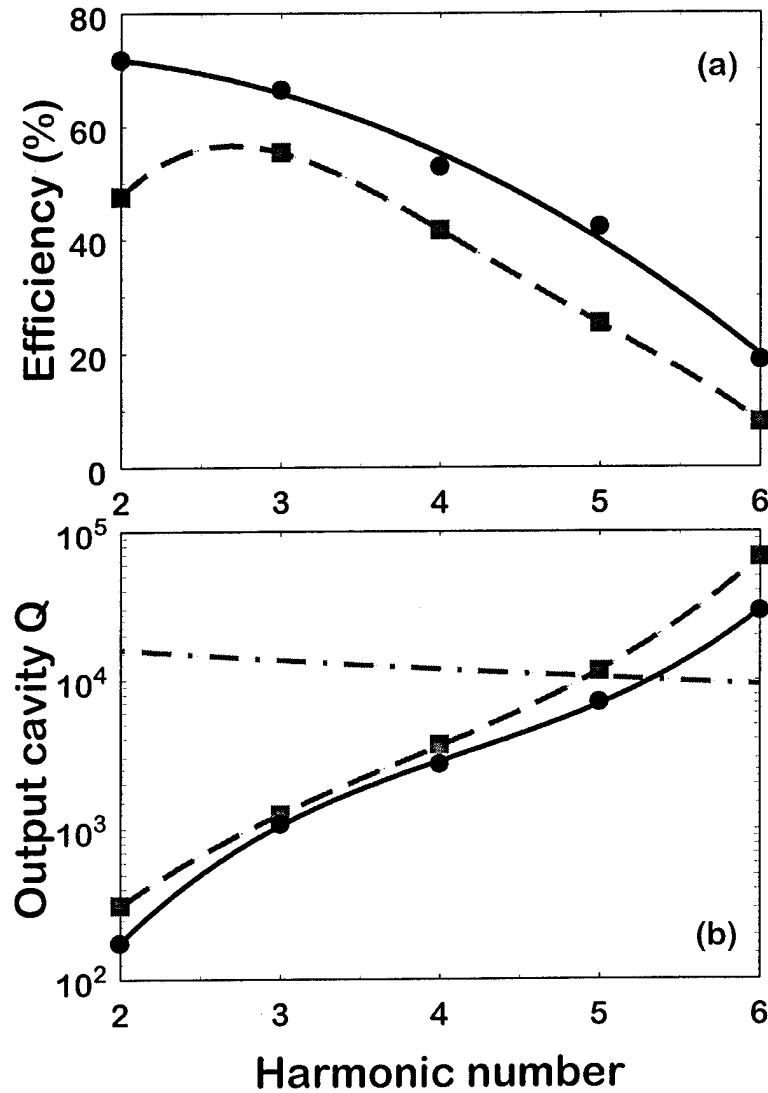


Figure 12. (a) The efficiency as a function of harmonic number for a zero-thickness beam (solid line) and a 0.75 mm thick beam (dashed line). The output cavity length is fixed at 15 cm and the magnetic field taper is fixed at 13%, but the drive frequency is proportional to the harmonic number. The remaining design parameters are adjusted to be compatible with the drive frequency. (b) The required quality factor for the zero-thickness beam (solid line) and the finite thickness beam (dashed line).

**On the design of electron guns for cyclotron resonance masers  
utilizing trochoidal electron beams (trochotrons)**

W. Lawson,<sup>†</sup> M. Garven,<sup>‡</sup> and G. S. Nusinovich  
Institute for Plasma Research  
University of Maryland  
College Park, MD 20742

**Abstract**

The properties of crossed-field electron guns which are capable of providing the required trochoidal beams for efficient cyclotron resonance interaction in the trochotron configuration are analyzed. A discussion of the beam parameters that are used to characterize the device performance is included in a general description of the operation of these guns. Two concrete designs are presented and are used to demonstrate the performance capabilities of these devices with respect to the beam self-fields, the externally applied electric and magnetic fields, and the electrode geometry. It is shown that these devices, which typically generate beams with large ratios of perpendicular to parallel (drift) velocity, are capable of producing extremely small drift velocity spreads over a wide range of parameters.

<sup>†</sup>Also with the Electrical Engineering Department, University of Maryland at College Park.

<sup>‡</sup>Also with the Naval Research Laboratory, Vacuum Electronics Branch, Washington, DC 20375.

## I. Introduction

It is well known that a non-relativistic charged particle, in the presence of uniform, perpendicular, static, external electric and magnetic fields, will execute a trochoidal trajectory which can be described as the superposition of a cyclotron orbit and a linear drift. This drift is perpendicular to both applied fields and has a speed equal to the ratio of the electric field magnitude to the magnetic field magnitude. Cyclotron resonance masers (CRMs), based on the interaction of fast electromagnetic waves with these trochoidal beams (trochotrons) were investigated in the early days of CRM development [1,2] and have recently been revisited [3]. The original trochotrons demonstrated reasonably good efficiencies in traveling-wave amplifier configurations, but were later abandoned in favor of CRM devices which interacted with helical beams (gyrotrons [4-8]). This abandonment occurred because the initial thrust of CRM development was for millimeter wave operation and the trochotron has an inherent frequency limitation that the gyrotron does not. Because the operating frequency in a CRM device is tied to an harmonic of the cyclotron frequency, the applied magnetic field must increase linearly with increasing frequency. And since, for a given axial drift velocity, the electric field strength in a trochotron is tied to the magnetic field, the frequency can be increased only until the breakdown limit is reached in the device. In gyrotrons, there is no applied dc electric field in the interaction region and correspondingly no such limitation.

Still, there are at least three good reasons to revisit trochotron operation. First, there are applications in radar, accelerators, and material processing that require centimeter-type wavelengths. Second, the early trochotron experiments were designed to be resonant at the first harmonic of the cyclotron frequency. Operation of CRM devices at higher harmonics is now

better understood, is fairly commonly used [9-11], and has the potential to increase the achievable operating frequency of trochotrons significantly. Finally, trochotrons can potentially be more effective in devices that operate fairly far from the cutoff frequency (e.g. wide-band amplifiers), because the trochoidal beam has considerably less axial velocity spread than the helical beam. So, for a given axial wavenumber, the inhomogeneous Doppler broadening of the cyclotron resonance, which spoils the interaction efficiency, can be much smaller in trochotrons than in gyrotrons. This is true because the axial drift velocity is tied to the external fields and the spread arises only from the relative space-charge potential depression and the inhomogeneities in the external fields. In helical beams, however, the axial velocity is unconstrained and is determined by the details of the electron gun optics and the space charge effects. Typical Magnetron Injection Guns (MIGs), which generate beams for the majority of gyrotrons, theoretically have perpendicular velocity spreads of a few percent. [12-15] In addition, experiments with high current, high compression MIGs have indicated that actual perpendicular spreads may be significantly higher. [16,17] Furthermore, axial velocity spreads in helical systems are typically larger than the corresponding perpendicular spreads by the square of the average perpendicular-to-parallel velocity ratio. In trochoidal beams, there is no such coupling between the spreads and extremely large ratios of perpendicular-to-parallel velocities (or more accurately rotating-to-drift velocities) can be achieved.

At the University of Maryland, we have begun to re-investigate the trochotron configuration. In an earlier paper [3], one of the authors analyzed the basic geometry, developed some scaling laws, and identified some important restrictions for this device. It was pointed out that the suc-

cess of these devices is contingent on the ability to produce a high quality electron beam with the required parameters. That issue is addressed in this paper.

In the next section we present the basic configuration of a planar electron gun that can be used to generate the trochoidal beam. The operation of the device is described and the method of determining the beam parameters is explained. EGUN [18] simulations of a simple planar gun geometry are performed in the third section to demonstrate the basic properties of the device. A more sophisticated device that uses an injection scheme which is similar to an earlier Russian design [1] is described in the fourth section. Both designs are geared to produce the necessary beam parameters for a moderate power, pulsed, 35 GHz, second harmonic trochotron. In the final section of this paper we summarize the results of this study.

## II . The basic planar electron gun geometry

The geometry of a simple planar trochotron electron gun is shown schematically in Figure 1. The device is assumed to be infinite in the direction perpendicular to the figure surface so that edge effects are neglected. The cathode is centered at the origin and the distance from the cathode center to the end of the gun is  $l_g$ . The emitter length is  $l_c$  and the cathode loading is assumed to be uniform with a density of  $J_c$ . Thus, the total beam current per unit length is  $I_0 = J_c l_c$ . The gap between the anode and cathode at the emitter strip is  $d_c$  and the gap between the plates at the beam exit is  $d_o$ . The magnetic field is  $B_c$  at the emitter strip and  $B_o$  at the end of the gun. The magnetic compression is the ratio of the two values:

$$f_m = B_o / B_c. \quad (1)$$

The anode - cathode potential difference is  $V_o$ . Far from the transition region, the external electric field between the plates is uniform, normal to the electrode surfaces, and equal to the

potential difference divided by the gap distance. Thus,  $E_o = V_o / d_o$  in the circuit region and  $E_c = V_o / d_c$  at the emitter strip. These results assume, of course, that the electron beam's self-fields can be neglected. The electric compression is defined by the ratio:

$$f_e = E_o / E_c = d_c / d_o. \quad (2)$$

We assume that electrons are emitted from the cathode with virtually no kinetic energy (e.g. thermionic emission). Since the net velocity of each electron is the sum of its drift velocity,  $v_d$ , and its cyclotron velocity,  $v_c$ , the two components must have equal magnitudes but opposite directions. Thus, the velocity ratio near the emitting surface is:

$$v_c(0) / v_d(0) = 1, \quad (3)$$

independent of the gun geometry. The velocity ratio at the end of the gun can be determined analytically with the single additional assumption that the magnetic field variation is adiabatic. If we define  $\alpha$  to be this ratio, then

$$\alpha = v_c(l_g) / v_d(l_g) = [v_c(0) / v_d(0)] \times [v_c(l_g) / v_c(0)] / [v_d(l_g) / v_d(0)]. \quad (4)$$

The first term in (4) is just equal to one from (3) and the third term is just

$$v_d(l_g) / v_d(0) = (E_o / B_o) / (E_c / B_o) = f_e / f_m \quad (5)$$

from (1) and (2). Under adiabatic conditions, the second term in (4) for a weakly relativistic electron beam is just equal to the square root of the magnetic compression, [14] so

$$\alpha = f_m^{3/2} / f_e. \quad (6)$$

Another parameter of primary importance is the average energy of the electrons ( $eV_b$ ) in the gun relative to the applied voltage  $V_o$ . A non-relativistic approximation of this value can be quickly determined as follows. Neglecting self-fields, the non-relativistic particle in the homoge-

neous field region attains its average energy when the two velocity components are perpendicular to each other:

$$eV_b = \frac{m}{2}(v_c^2 + v_d^2) = (1 + \alpha^2) \frac{m}{2} \left( \frac{E_o}{B_o} \right)^2. \quad (7)$$

From (7), the relative potential can be readily found:

$$\frac{V_b}{V_o} = (1 + \alpha^2) \frac{mV_o}{2e d_o^2 B_o^2}. \quad (8)$$

The remaining design values and equations come from the consideration of the microwave interaction and the technical limits on breakdown.  $B_o$  is determined by the resonance condition and  $V_o$  and  $I_o$  are derived from power requirements. The spacing  $d_o$  is set by the microwave mode, given the realistic constraints on  $E_o$ . There are at least two reasons to consider a lower value of electric field in the cathode region in spite of the fact that it increases the required magnetic compression for a given velocity ratio. The first is that the restriction on the maximum allowable electric field is typically more stringent near the emitter. The second advantage is that the relative width of the beam compared to the distance it travels perpendicular to the emitter is smaller, minimizing the effects of non-adiabatic changes in the electric and magnetic field. This in turn helps to minimize the spread in the average beam energy. A potential disadvantage of the lower field is the associated decrease in the space-charge limited current density,  $J_{sc}$ , which is given for the infinite planar case by [19]:

$$J_{sc} \approx 2.34 \times 10^{-6} V_o^{3/2} / d_c^2 \quad (9)$$

where the units for  $J_{sc}$ ,  $V_o$ , and  $d_c$  are A/cm<sup>2</sup>, V, and cm, respectively.

In the following two sections, we will use these equations to design and analyze two electron gun configurations which are suitable for a 35 GHz tube. The two-dimensional code EGUN is used to simulate the electron guns, so edge effects are neglected. Convergence is checked by varying the mesh size and the number of rays. Magnetic field tapering is modeled along the axis either by the smooth function:

$$B_t = \frac{(B_o + B_c)}{2} + \frac{(B_o - B_c)}{2} \tanh[(z - z_m) / \xi] \quad (10)$$

or by the piecewise linear function:

$$B_t = \begin{cases} B_c & z < z_m - \xi \\ \frac{(B_o + B_c)}{2} + \frac{(B_o - B_c)}{2} \left[ \frac{z - z_m}{\xi} \right] & z_m - \xi < z < z_m + \xi \\ B_o & z > z_m + \xi \end{cases} \quad (11)$$

where  $z_m$  is the midpoint of the field transition and  $\xi$  is a measure of the transition width. These models are adequate because of the relative insensitivity of the beam parameters to the field profile. To model inhomogeneities in the applied magnetic field of a real magnetic coil system, we use (10) and stop the simulations before  $B_t$  attains its maximum value.

Characterization of the average velocity ratio (and other beam parameters) is complicated by space charge, inhomogeneities in the applied fields, and the fact that the relativistic correction to the electron motion in a reference frame moving at the drift velocity  $v_d$  results in non-circular motion. The values quoted in this paper are found by averaging the simulated quantities at various locations in the final orbit of each electron. Uncertainties in these quantities are always checked and are typically quite small.



### III. An in-line gun design

The electron guns characterized in this paper are designed to meet the needs of a second harmonic trochotron amplifier with the parameters given in Table I. The specified magnetic field represents a 12.6% detuning from the resonant field required for 35 GHz operation at the second harmonic. We assume a thermionic emitter and restrict the cathode loading accordingly; the impact of using a field-emitter array (FEA) cathode will be discussed briefly in the final section. The beam power density is selected to demonstrate useful power levels with a fairly narrow system. The peak electric field indicated is for the circuit region and is below what has been achieved in short pulse (microsecond) systems. We restrict the peak field in the anode-cathode region to half of this value.

The optimized electrode field configuration and the magnetic field profile for the in-line gun design are shown in Fig. 2. The simulated beam trajectory is also indicated for the nominal parameters given in Table II. The anode cathode gap is reduced from 0.84 cm in the emitter region to 0.42 cm over a distance of 1.9 cm. The emitter length is 0.4 cm and the surface is curved to minimize the spread in the beam energy. The left-most point on the emitter surface is parallel to the anode and the surface changes by  $10^\circ$  with a 2.29 cm radius of curvature. The current density is selected to achieve the design beam power density if the beam is centered between the two plates. The cathode is shown as two separate conductors. This is done so that the right electrode could in principle be (slightly) reversed biased to minimize the production of secondary electrons. The two electrodes were kept at the same potential in all of the simulations that we performed.

As evident in Fig. 2, the beam is well-formed and maintains a high degree of phase coherence throughout the gun region. The simulated gun parameters at the nominal design point are given in the middle column of Table III. The average velocity ratio of 5.0 is obtained with a drift velocity spread of less than 0.1%. The combination of these two values is unheard of in MIG designs and is a direct consequence of the drift velocity mechanism. The spread in pitch angle, though over an order of magnitude higher, is still considerably smaller than what is readily attainable in MIGs. The cathode - average beam position spacing is about 56% of the cathode - anode spacing, so that the targeted beam power is modestly exceeded. The beam voltage spread arises in part from self-fields, but mostly from the 2.3% spread in the electron guiding center radii. The simulated space-charge limiting (SCL) current density is about  $52 \text{ A/cm}^2$  and is higher than the theoretical value of  $37 \text{ A/cm}^2$  obtained from (9) due to the finite emitter width. Clearly the nominal loading of  $10 \text{ A/cm}^2$  is well into the temperature-limited regime. The peak electric field of 129 kV/cm occurs on the anode at the end of the gun. The electric field at the corresponding point on the cathode is about 18 kV/cm lower because of self-field effects.

The dependence of average velocity ratio on the applied cathode magnetic field (and hence on the magnetic compression) is indicated in Fig. 3a by the solid line. The theoretical curve given by (6) is indicated in the figure by the dash-dotted line. Since the cathode is curved, the average cathode - anode distance is used in the equation. Agreement between simulation and theory is seen to be excellent over the entire range of fields. Cathode magnetic fields of 1.15 kG and below result in partial beam interception on the anode. Fields above 1.65 kG result in partial beam interception on the cathode. Still, the velocity ratio can be adjusted from about 3.5 to 5.5 in

the accessible range of fields. The resultant drift velocity spread is indicated in the figure by the dashed curve. The spread remains well below 1% until the field exceeds 1.5 kG.

From (8), it is evident that the average beam energy is also quite dependent on the cathode magnetic field (via the dependence of  $\alpha$  on  $f_m$ ). The simulated and analytic dependencies of beam voltage on cathode magnetic field are indicated in Fig. 3b by the solid and dash-dotted lines, respectively. The two curves indicate a similar drop-off in voltage with decreased magnetic compression, but the theoretical curve is consistently about 2 - 3 kV higher. At least half of this discrepancy can be accounted for by the potential depression of the beam. The spread in beam voltage is shown in Fig. 3b by the dashed line. As with the spread in  $\alpha$ , there is a marked increase after the field exceeds 1.5 kG. Comparing the results in the figure, it is clear that the pre-eminent effect of cathode magnetic field variations is on the beam voltage average and spread.

The dependence of average velocity ratio on the voltage applied across the two electrodes is indicated by the solid line in Fig. 4. Even though there is an increase in the electric field everywhere in the circuit, the electric compression remains unchanged and (6) predicts no variation in  $\alpha$ . The slight increase in  $\alpha$  with increasing voltage is mainly due to the relative decrease in the potential depression. Partial beam interception on the anode occurs with an applied voltage of 60 kV. It is interesting to note that the ratio of average beam voltage to applied voltage increases from 37% at 40 kV to 68% at 60 kV. The drift velocity spread is given in the figure by the dashed line. The spread is well below 0.5% for all beam voltages above 45 kV. The decrease in beam quality below that point is due in large part to the drop off in beam voltage and the resultant increase in relative space-charge forces.

Figure 5 demonstrates the dependence of average velocity ratio (solid line) and drift velocity spread (dashed line) on cathode loading. Again, the simple theory predicts no variation in velocity ratio and the weak dependence exhibited in the simulations can be directly attributed to space-charge depression. This small change in  $\alpha$  could readily be compensated for by a small change in the cathode magnetic field, if desired. A high quality beam is achieved from current densities of 2 A/cm ( $J_c = 5 \text{ A/cm}^2$ ) up to 5 A/cm ( $J_c = 12.5 \text{ A/cm}^2$ ). The increase in velocity spread with increasing current is due, of course, to space-charge effects. The smaller increase in spread that occurs as the current density goes to zero results from the inhomogeneities in the magnetic field and the large spread in guiding center transverse locations. This spread can be reduced by optimizing the electrode surfaces at lower current densities, but that effort would result in increased spread at the operating current density.

#### IV. An injection gun design

An injection gun design, based on the circuit parameters in Table I but utilizing a geometry similar to the earlier Russian design in [1], is shown in Fig. 6. Such a configuration can be used to isolate the microwave path from the beam source in an amplifier configuration. In addition to the electrode configuration, the magnetic field profile and the simulated ray trajectories are also indicated in the figure. The piecewise linear magnetic field profile in (11) is used for this design because of the fairly large transverse range of the beam. The shape of the electrodes in the emitter region is nearly identical to that of the in-line gun. In fact, the electrode parameters are identical to those listed in Table II. Exactly the same emitter shape and nominal cathode loading are used. The anode has the same  $14^\circ$  slope as the in-line design, beginning at the same relative axial position. However, the taper ends after about 5 mm in order to begin the transition to the upper

plate. To promote an adiabatic transition, the radius of the curvature of the lower plate in the transition region is selected to be about 10 times larger than the final Larmor radius. The circuit magnetic field ( $B_0$ ) is identical in the two cases, but the complex injection geometry requires a cathode field of  $B_c=1.355$  kG to achieve the desired velocity ratio of 5.0. The transition width is  $\xi=1.9$  cm and the transition center is  $z_m=2.4$  cm.

The simulated results for the configuration are given in the final column of Table III. In spite of the more complex geometry, the spread in the drift velocity is only about 0.1% and is still well over an order of magnitude smaller than the best values found in MIGs. The average beam power is only slightly lower in the injection design because of a small difference in the average guiding center location. However, the guiding center spread is smaller for this case, and this results in improved values of beam voltage and velocity ratio spread. Comparing the beam trajectories shown in Figs. 2 and 5, it is apparent that the injection gun beam is considerably more mixed than the in-line beam. The mixing begins in the injection region but doesn't appear to have any adverse effects on the beam quality. The peak electric field occurs on the lower electrode at about 3.5 cm (in the middle of the small radiused transition). The peak field on the anode is 135 kV/cm and occurs on the radiused end. The latter value may be adequate and the higher value could be reduced in an actual design simply by increasing the transition radius.

## V. Discussion

This study has demonstrated the feasibility of electron guns for trochotrons in a parameter regime of interest for current applications. The beam voltage, peak electric field, and cathode loading are all consistent with what is readily achievable in modern tubes. Ratios of transverse velocity to drift velocity of 5 (or higher) are easily obtainable with drift velocity spreads well

below 1%. Electron beams with such low drift velocity spreads are definitely suitable for resonant operation far from cutoff. So, the main issue in the development of wideband traveling-wave trochotrons could be providing proper coupling between the electrons and a wave propagating with a large group velocity (rather than the deleterious effect of inhomogeneous Doppler broadening inherent in gyro-TWTs).

The simple analytic model of the gun's beam dynamics results in good estimates of the system parameters as long as the electric and magnetic fields are varied adiabatically and the relative space-charge effects are sufficiently small. Beam quality is seen to remain high over a wide range of parameters. Frequently, the parameter most sensitive to system variations is the relative location of the beam between the plates and the resulting average beam energy.

Though not presented here, we have also investigated the performance of trochotron guns with narrower emitters and higher current densities. Such emitters are consistent with the FEA cathodes that are under development at many locations. [20-22] These systems typically require no curvature and give higher beam quality over a greater range in current densities.

## **VI. Acknowledgment**

The work was supported by the Department of Defense Tri-Services program.

Table I. The microwave circuit requirements.

Parameter	Value
Output frequency (GHz)	35
Applied voltage $V_o$ (kV)	50
Beam power density (kW/cm)	100
Circuit magnetic field $B_o$ (kG)	6.0
Maximum electric field (kV/cm)	150
Nominal cathode loading ( $A/cm^2$ )	10

Table II. The in-line gun parameters.

Parameter	Value
Circuit plate gap $d_o$ (cm)	0.42
Cathode-anode plate gap $d_c$ (cm)	0.84
Nominal Current density $I_o$ (A/cm)	4.0
Cathode magnetic field $B_c$ (kG)	1.26
Field transition location $z_m$ (cm)	1.45
Field transition length $\xi$ (cm)	0.6
Cathode curvature (degrees)	10
Anode taper angle (degrees)	14

Table III. The simulated properties of the two gun designs.

Parameter	In-Line	Injection
Average velocity ratio $\alpha$	5.00	5.00
Velocity ratio spread (%)	1.70	0.74
Normalized average drift velocity	0.0607	0.0605
Drift velocity spread (%)	0.06	0.11
Average beam power (kW/cm)	106.4	104.7
Beam voltage spread (%)	3.55	1.50
SCL current density (A/cm <sup>2</sup> )	52	52
Peak electric field (kV/cm)	129	153



### Figure Captions

- Figure 1. Layout of a simple trochoidal gun configuration.
- Figure 2. Schematic of the in-line gun electrode configuration. The simulated ray trajectories at the nominal parameters of Table II are shown in the figure along with the magnetic field profile.
- Figure 3. (a) The dependence of simulated average velocity ratio (solid line) and drift velocity spread (dashed line) on cathode magnetic field. The theoretical curve for the average velocity ratio based on (6) is indicated by the dash-dotted line. (b) The dependence of simulated average beam voltage (solid line) and voltage spread (dashed line) on cathode magnetic field. The theoretical curve for the average voltage based on (8) is indicated by the dash-dotted line.
- Figure 4. The dependence of simulated average velocity ratio (solid line) and drift velocity spread (dashed line) on applied voltage.
- Figure 5. The simulated average velocity ratio (solid line) and drift velocity spread (dashed line) as a function of beam current density.
- Figure 6. Schematic of the injection gun electrode configuration. The simulated ray trajectories at the nominal parameters are shown in the figure along with the magnetic field profile.

## References

- [1] I. I. Antakov, A. V. Gaponov, O. V. Malygin, and V. A. Flyagin, "Application of induced cyclotron radiation of electrons for the generation and amplification of high-powered electromagnetic waves," *Radio Eng. and Electron. Phys.*, vol. 11, pp. 1995-1997, 1966.
- [2] A. V. Gaponov, M. I. Petelin, and V. K. Yulpatov, "The induced radiation of excited classical oscillators and its use in high-frequency electronics," *Radiophysics and Quantum Electronics*, vol. 10, pp. 794-813, 1967.
- [3] G. S. Nusinovich, "The linear theory of cyclotron resonance masers with trochoidal beams," *Physics of Plasmas*, vol. 2, pp. 3531-3538, 1995.
- [4] V. A. Flyagin, A. V. Gaponov, M. I. Petelin, and V. K. Yulpatov, "The gyrotron," *IEEE Trans. Microwave Theory Tech.*, vol. 25, pp. 514-521, 1977.
- [5] R. S. Symons and H. R. Jory, *Advances in Electronics and Electron Physics*, C. Marton, ed. (New York: Academic Press, 1981), vol. 55, Ch. 1, pp. 1-75.
- [6] V. L. Granatstein, M. E. Read, and L. R. Barnett, *Infrared and Millimeter Waves*, K. Button, ed. (New York: Academic Press, 1981), vol. 5, Ch. 5, pp. 267-304.
- [7] K. E. Kreischer, T. L. Grimm, W. C. Guss, A. W. Mobius, and R. J. Temkin, "Experimental study of a high-frequency megawatt gyrotron oscillator," *Phys. Fluids*, vol. B 2, pp. 640-646, 1990.
- [8] B. Levush and T. M. Antonsen, "Mode competition and control in high-power gyrotron oscillators," *IEEE Trans. Plasma Sci.*, vol. 18, pp. 260-272, 1990.
- [9] H. W. Matthews, W. Lawson, J. P. Calame, M. K. E. Flaherty, B. Hogan, J. Cheng, and P. E. Latham, "Experimental studies of stability and amplification in a two-cavity second harmonic gyrokylystron," *IEEE Trans. Plasma Sci.*, vol. 22, pp. 825-833, 1994.
- [10] G. F. Brand, Y. Idehara, T. Tatsukawa, and I. Ogawa, "Mode competition in a high harmonic gyrotron," *Int. J. Electron.*, vol. 72, pp. 745-758, 1992.
- [11] V. G. Pavel'ev, Sh. E. Tsimring, and V. E. Zapevalov, "Coupled cavities with mode conversion in gyrotrons," *Int. J. Electronics*, vol. 63, pp. 379-391, 1987.
- [12] M. Caplan and C. Thorington, "Improved computer modeling of magnetron injection guns for gyrotrons," *Int. J. Electron.*, vol. 51, pp. 415-426, 1981.
- [13] J. L. Seftor, A. T. Drobot, and K. R. Chu, "An investigation of a MIG suitable for use in cyclotron resonance masers," *IEEE Trans. Electron. Dev.*, vol. 26, pp. 1609-161, 1979.
- [14] W. Lawson, J. Calame, V. L. Granatstein, J. Neilson, G. S. Park, and C. D. Striffler, "The design of a high peak power relativistic magnetron injection gun," *Int. J. Electronics*, vol. 61, pp. 969-984, 1986.
- [15] W. Lawson and V. Specht, "Design comparison of single-anode and double-anode 300 MW magnetron injection guns," *IEEE Trans. Electron Dev.* vol. 40, pp. 1322-1993.

- [16] E. G. Avdoshin and A. L. Gol'denberg, "Experimental investigation of adiabatic electron guns of cyclotron resonance masers," *Radiophysics and Quantum Electronics*, vol. 16, pp. 1241-1246, 1973.
- [17] W. C. Guss, M. A. Basten, K. E. Kreischer, and R. J. Temkin, "Velocity spread measurements on a magnetron injection gun beam," *J. Appl. Phys.*, vol. 76, pp. 3237-3243, 1994.
- [18] W. B. Herrmannsfeldt, "Electron trajectory program," SLAC, Stanford, CA, Rep. 226, Nov. 1979.
- [19] J. D. Lawson, *The Physics of Charged-particle Beams* (Clarendon Press, Oxford, 1977), p. 126.
- [20] M. Garven, A. D. R. Phelps and S. N. Spark, "Field emission array experiments relevant to cold cathode gyrotrons," *Vacuum*, vol. 45, pp. 513-517, 1994.
- [21] I. Brodie and C.A. Spindt, "Vacuum microelectronics," *Advances in Electronics and Electron Physics*, C. Marton, ed. (New York: Academic Press, 1992), vol. 83, pp. 1-108.
- [22] M. A. Kodis, K. L. Jensen, E. G. Zaidman, B. Goplen, and D. N. Smithe, "Operation and optimization of gated field emitter arrays in inductive output amplifiers," submitted to *IEEE Trans. Plasma Sci.* (this issue).

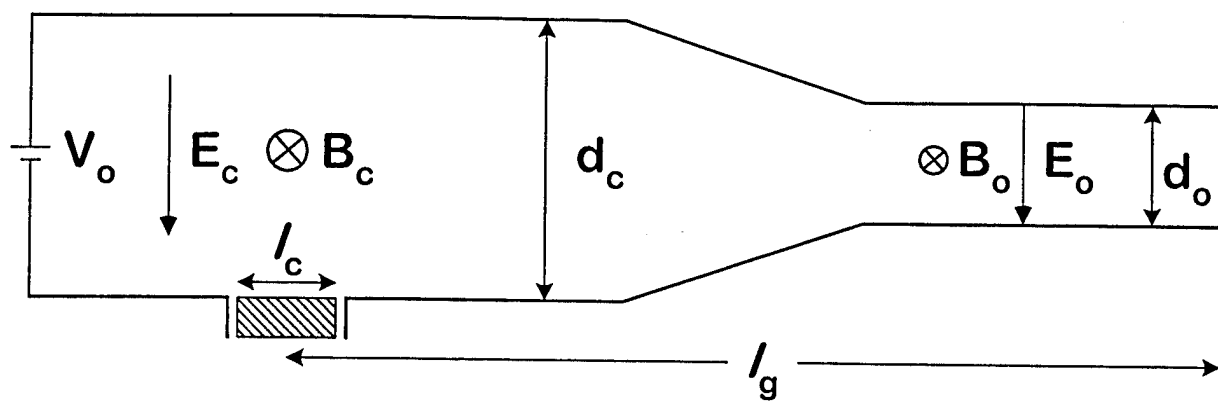


Figure 1. Layout of a simple trochoidal gun configuration.

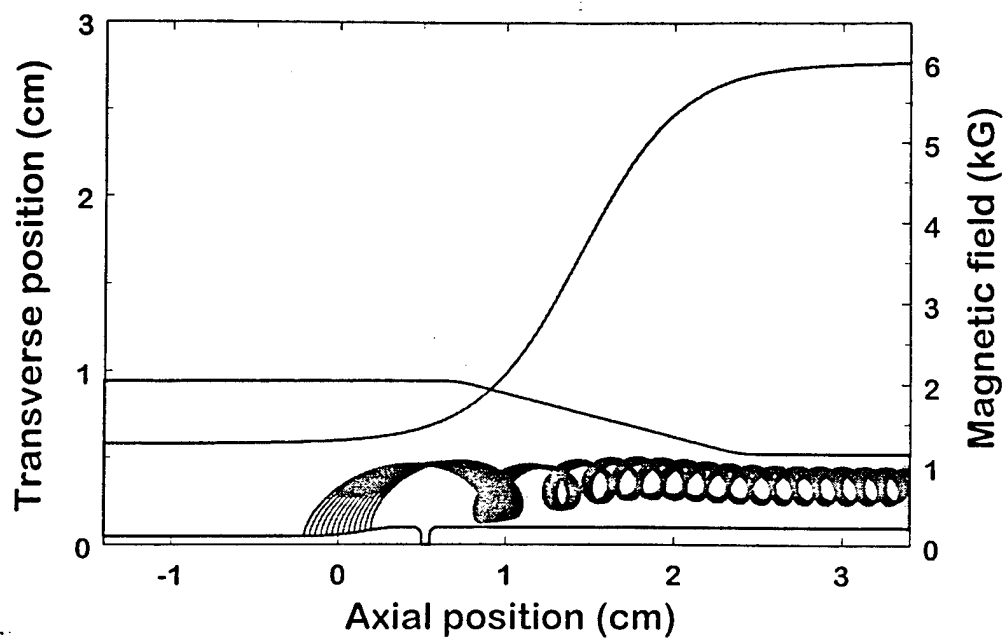


Figure 2. Schematic of the in-line gun electrode configuration. The simulated ray trajectories at the nominal parameters of Table II are shown in the figure along with the magnetic field profile.

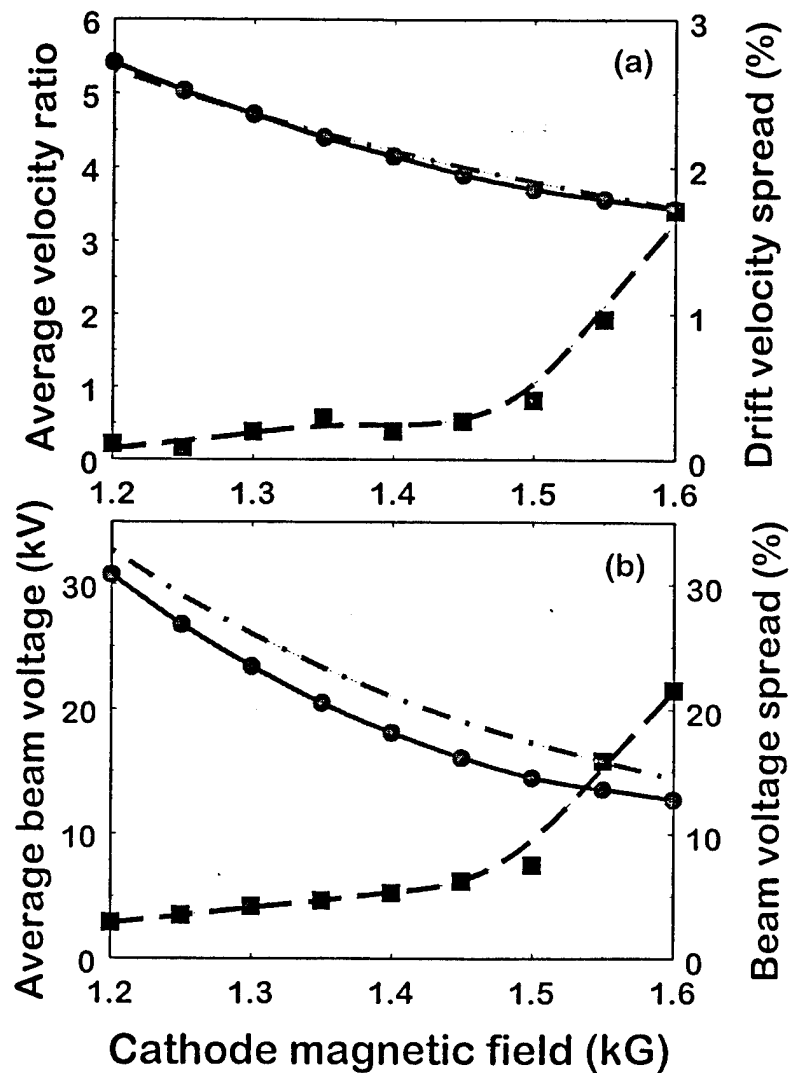


Figure 3. (a) The dependence of simulated average velocity ratio (solid line) and drift velocity spread (dashed line) on cathode magnetic field. The theoretical curve for the average velocity ratio based on (6) is indicated by the dash-dotted line. (b) The dependence of simulated average beam voltage (solid line) and voltage spread (dashed line) on cathode magnetic field. The theoretical curve for the average voltage based on (8) is indicated by the dash-dotted line.

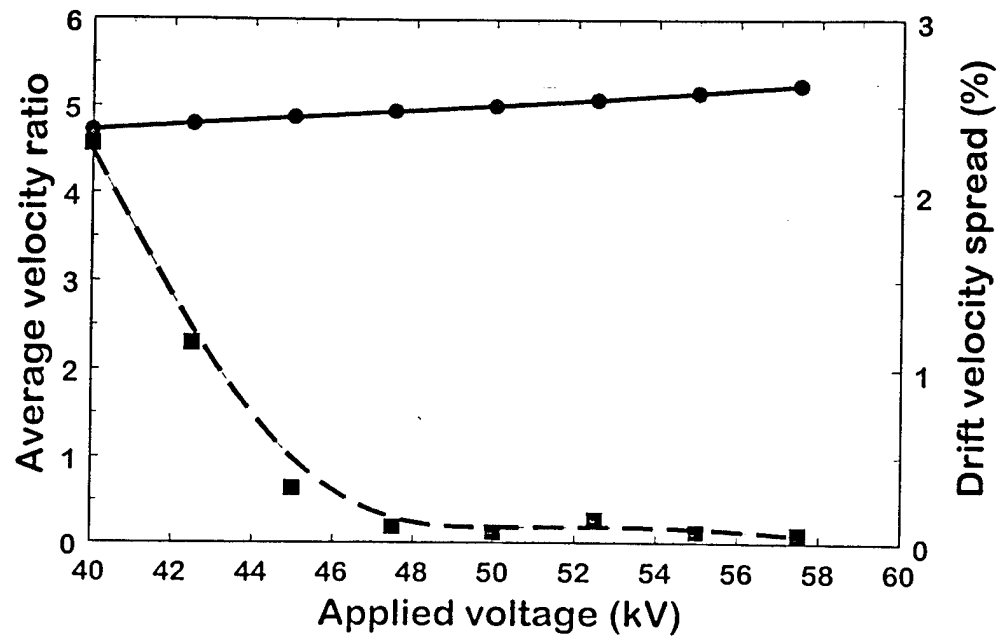


Figure 4. The dependence of simulated average velocity ratio (solid line) and drift velocity spread (dashed line) on applied voltage.

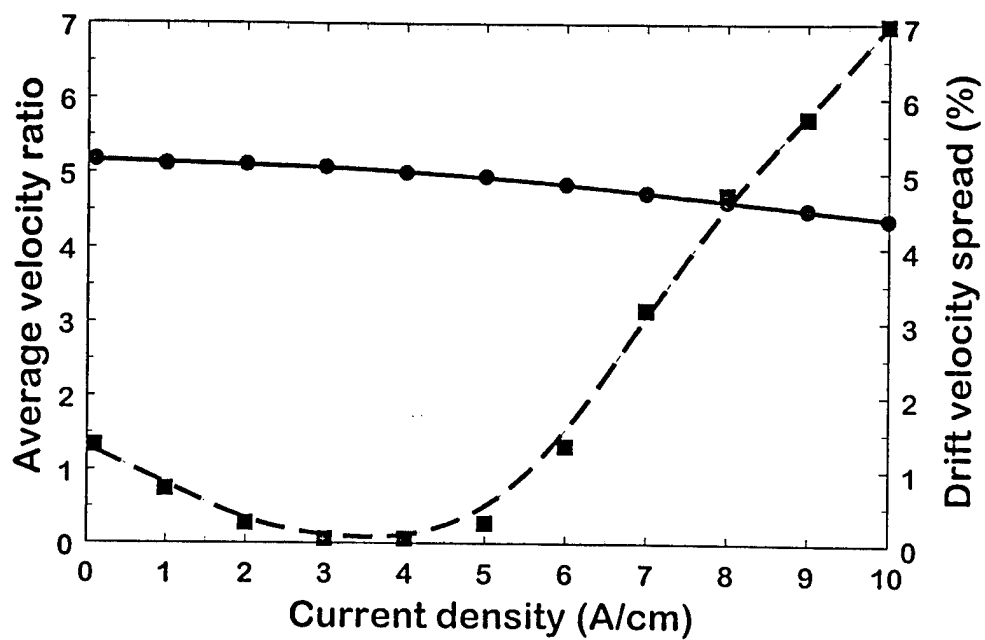


Figure 5. The simulated average velocity ratio (solid line) and drift velocity spread (dashed line) as a function of beam current density.



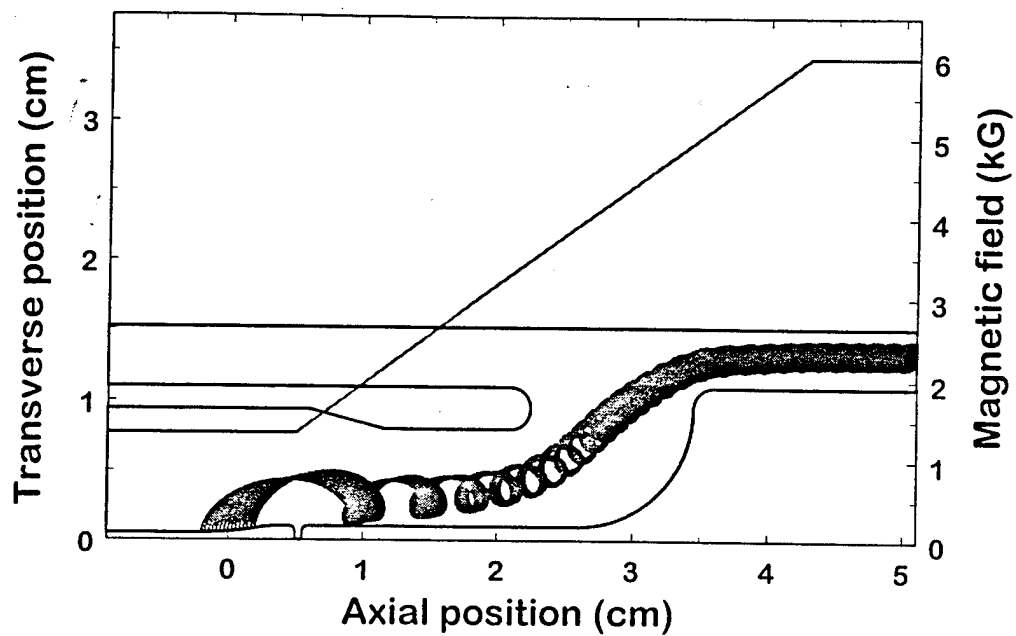


Figure 6. Schematic of the injection gun electrode configuration. The simulated ray trajectories at the nominal parameters are shown in the figure along with the magnetic field profile.